1-1-2017

Strain Rate Dependence And Impact Behavior Of Abs (acrylonitrile-Butadiene-Styrene) Amorphous Thermoplastic

Mehmet Akif Dundar
Wayne State University,

STRAIN RATE DEPENDENCE AND IMPACT BEHAVIOR OF ABS (ACRYLONITRILE-BUTADIENE-STYRENE) AMORPHOUS THERMOPLASTIC

by

MEHMET AKIF DUNDAR

DISSERTATION

Submitted to the Graduate School

of Wayne State University,

Detroit, Michigan

in partial fulfillment of the requirements

for the degree of

DOCTOR OF PHILOSOPHY

2017

MAJOR: MECHANICAL ENGINEERING

Approved By:

_____

Advisor Date

_____

_____

_____

DEDICATION

To my mother, my brothers and my sister

ACKNOWLEDGEMENTS

First and foremost, I would like to express my deep gratitude to my advisor Prof. Emmanuel Ayorinde for his precious guidance and support throughout this study. He provided me pretty good working environment, all necessary materials and equipment's without any hesitation to conduct my experiments and implement their numerical simulations. It has been a great privilege for me studying under his guidance.

Secondly, I would like to convey my gratefulness to my committee members Prof. Golam Newaz and Prof. Xin Wu for allowing me to study and conduct some of my experiments in their laboratories. Additionally, I am very thankful to them for their guidance and being my committee members.

Thirdly, I would like to express my thankfulness to Prof. H.C.Wu for his support and serving as my committee member. Fourthly, I would like to thank the Turkish Ministry of Education for its financial support throughout my PhD study.

Finally, I would like state that I am extremely grateful to Dr. Paul Begeman and my colleague Tal Saif for their guidance and support during high speed tension tests.

TABLE OF CONTENTS

LIST OF TABLES

LIST OF FIGURES

CHAPTER 1 INTRODUCTION

1.1 Introduction

Amorphous thermoplastics have been receiving a great deal of attention to be utilized as a structural component in a wide range of engineering applications, such as marine craft, protective headgear, automotive trim components and medical devices because they possess many distinguished material properties including high stiffness, high toughness, good impact resistance, high compressive strength and low density. Amorphous thermoplastics are formed by chain macromolecules that are chaotically arranged in their structures as shown in Fig 1.1. The material properties of amorphous thermoplastics including elasticity, strength and toughness are significantly influenced by van der Waals intermolecular forces that are caused by an intermolecular interaction of chains to one another [1]. The randomly arranged chain macromolecules result a highly complex mechanical response for amorphous thermoplastics when subjected to loads. During deformation, the chain macromolecules change their positions to one another with a relative motion leads to the material behavior of amorphous thermoplastics strain rate dependent [2-13]. In other words, the strain rate response of amorphous thermoplastics is directly associated with the deformation mechanism of chain macromolecules with respect to an applied deformation rate; therefore, obtaining the strain rate dependent material behavior of amorphous thermoplastics is crucial to understand how chain macromolecules deform under various strain rates and to calculate their mechanical response under dynamic loading conditions such as impact[14-18]. In addition, amorphous thermoplastics can undergo extremely large plastic strains under load as a result of the relative motion of chains to one another. The capability of sustaining extremely large plastic deformations makes amorphous thermoplastics very appealing for such unique engineering applications where a good impact performance is the primary concern

[19-21]. Despite the fact that the strain rate dependent material behavior of amorphous thermoplastics under low strain rates is well comprehensible, understanding their behaviors under high strain rates is still a great topic [2]. Because they develop an intrinsic failure mechanism subjected to high strain deformations and there are many opening questions why they exhibit that mechanism[22-24].

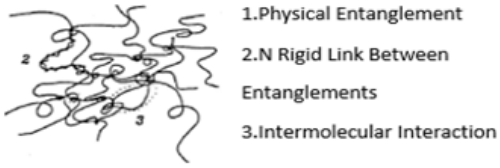

Fig 1.1. Molecular Structure of Amorphous Thermoplastics [25]

The typical stress-strain feature of amorphous thermoplastics under tension can be divided into five distinct stages such as linear elastic, nonuniform plastic deformation or strain softening, cold drawing, strain hardening and failure, respectively [8].

In the linear elastic region, the deformation is completely recovable due to the reversible rotations of chain macromolecules to one another. In the nonuniform plastic deformation stage, a very drastic reduction in stress with an increasing strain begins to form at a point that is known as post yield or the onset of necking point in amorphous thermoplastics[26]. In the post yield point, chain macromolecules start to change their initial positions irreversibly implying that the material response is no longer homegenous [2]. After the yield point, the yield stress perpetually goes down until a point where the both the stress and the necking start to become stable. The material behavior of amorphous thermoplastics in the region of their tensile stress-strain curves located between those two points is named the strain softening or intrinsic yield drop[27]. In the strain softening region, the formation of localized material changes takes place. Following the strain softening, the chains intend to be straight and reach their maximum strecthing level that results a strain hardening feature in amorphous thermoplastics and then the failure occurs eventually.

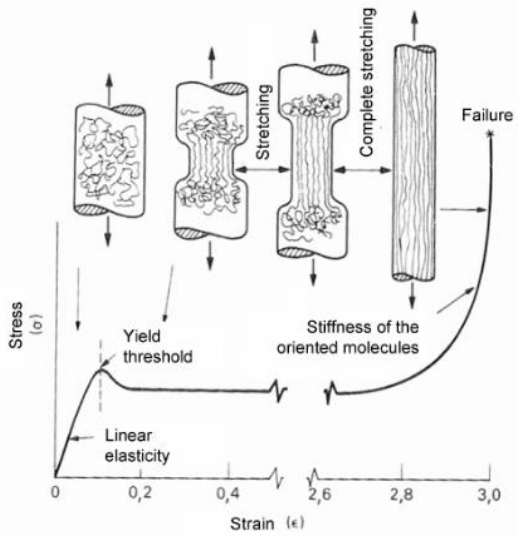

Fig 1.2. Typical Stress-Strain Curve of Amorphous Thermoplastics

The mechanical behaviors of amorphous thermoplastics under compression significantly vary in their stress states under tension indicating that their yield stress is pressure dependent[28-36]. In general, compressive strength of amorphous thermoplastics is about15% higher than their tensile strength [8]. The pressure effect on yield stress needs to be taken into account for engineering applications where an amorphous thermoplastic material is subjected to such a loading condition like impact that simultaneously dictates various stress states including tension, compression and shear [37]. Eventhough a great deal of study has been devoted to characterize the different behavior of amorphous thermoplastics under tension and compression, further investigation has been highly desirable [38-40].

Although there have been many constituve models proposed to accurately predict the complex strain rate and pressure dependent material behavior of amorphous thermoplastics, it has not been accomplished yet[26, 41]. Therefore, there are at least three different mechanical tests such as uniaxial tension, uniaxial compression and shear that should be carried out on amorphous thermoplastics at various strain rates to fully charactarize their material behavior, and their numerical analysis needs to be performed based on data obtained from those mechanical tests.

In this study, the strain rate dependent material behavior of ABS amorphous thermoplastic over a wide range of strain rates from very low to moderate obtained from three distinct mechanical tests such as uniaxial tension, uniaxial compression and shear has been clearly documented.Moreover, the flexural material behavior of ABS was characterized through the conducted 3-point bending tests under various deformation rates ranging from low to moderate. Additionally, the impact performance of ABS under different impact energies was identified. After impact tests, two highly effective non-destructive evaluation tools, including the ultrasonic C-Scan and laser scanning microscopy were utilized to detect damage areas inside the ABS specimens and imperfections on the front and back surfaces of ABS,respectively. While the detected damage areas were displayed as a two dimensional graphical representation,the inspected surfaces were illustrated as both two dimenional and three dimensional graphical representation.

For the finite element modeling of uniaxial tension,uniaxial compression,3-point bending and impact tests carried out on ABS, we addressed one semi-empirical material model (SAMP-1) in Ls-Dyna that is quite capable of capturing actual material behavior of polymer based materials like ABS.In numerical predictions, this material model uses true plastic stress-true plastic strain curves as a tabulated data that needs to be obtained from at least three fundemantal mechanical tests including uniaxial tension, uniaxial compression and shear over a wide range deformation rates. Thus, the numerical implementations were performed by the use of experimentally measured true stress-true strain curves as an input in SAMP-1 material model.Hence, the numerical results were compared favoribly to the experimental results.

Acrylonitrile Butadiene Styrene (ABS):

ABS (Acrylonitrile-Butadiene-Styrene) is a very significant and widely used amorphous thermoplastic on which, on account of its importance in industry, multiplied billions of dollars are

spent yearly in USA alone, not to talk of the rest of the world. It is primarily utilized across industry and in domestic situations to abate damaging effects of impacts. This fact makes it a candidate for serious and thorough research. Additional applications of ABS include use in civil infrastructure, scientific piping systems, sports items, musical instruments, automotive trims for air, sea and land vehicles, medical gadgets, headgear that protect the skull, luggage applications, toys, consumer goods, etc.

ABS was produced from the combination of three monomers acrylonitrile,butadiene and styrene as an alternative material to styrene-butadiene-rubber (SBR) during the second world war[42].The first commercially available ABS materials started in utilizing as a structural component in automotive industry in an effort to develop the best properties of ABS from the polymerization of those three monomers in 1950s[43] as illustrated in Fig 1.3.

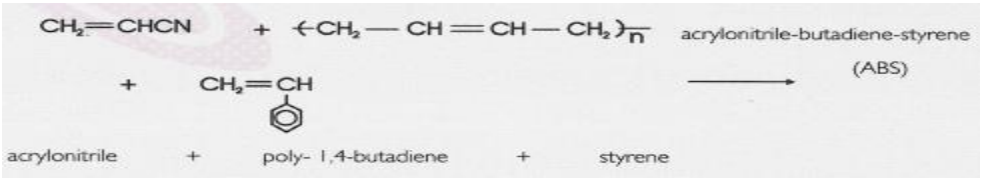

Fig 1.3. Chemical Structure of ABS

The material quality of ABS is directly controlled by these monomers and their propotions when compared to one another. Each monomer has a different contribution to the material behavior of ABS as indicated in Fig 1.4. For instance, the function of acrylonitrile is to provide chemical and thermal resistance; rigidity and ease of processability are given by styrene and ABS gains its impact strength and toughness from butadiene.

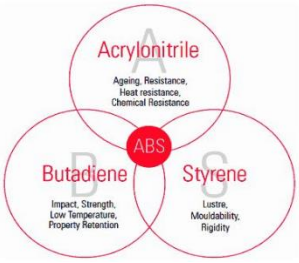

Fig 1.4. Contribution of monomers to the material properties of ABS

ABS grabs much attention in regards to its excellent impact resistance in comparision to other amorphous thermoplastics. Rubber particles that are randomly dispersed in the structure of ABS significantly improve its toughness and delay craze initiation leading to a large plastic deformation that the ABS can sustain[42, 44-47]. This makes the ABS very appealing for unique engineering applications where good impact resistance is highly demanded.

Particularly, the use of lightweight and good impact resistance plastic materials as a replacment of metals for both internal and external structural components in automotive industry has been of high interest for reducing weight and increasing the fuel efficincy; therefore, many metallic parts of cars have been replaced with various plastic materials that differently contribute the mechanical quality related to weight reduction, strength and resistance. The external and internal structural parts of cars made of plastics are shown in Fig 1.5.

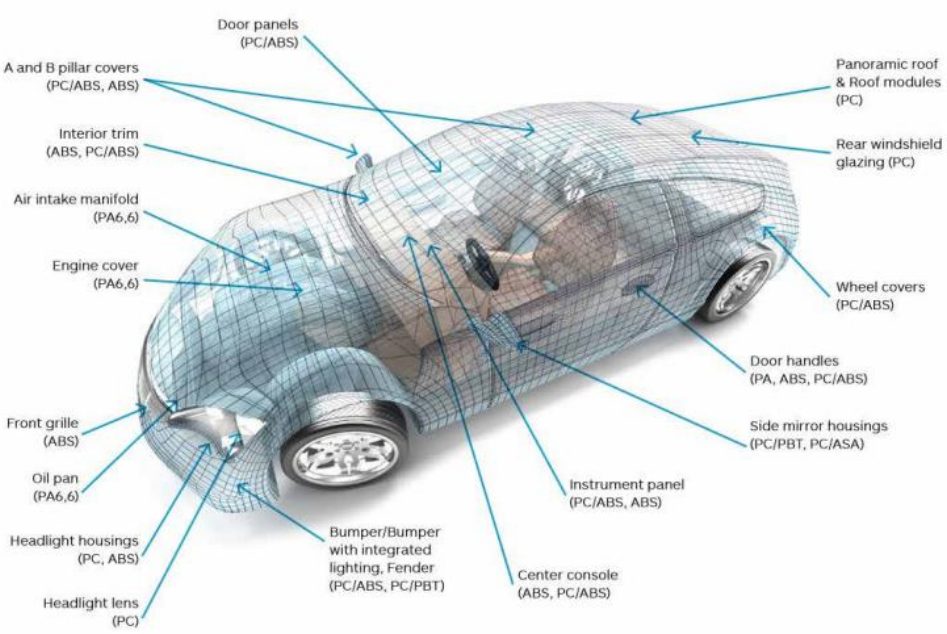

Fig 1.5. The plastic parts used in automotive industry[48]

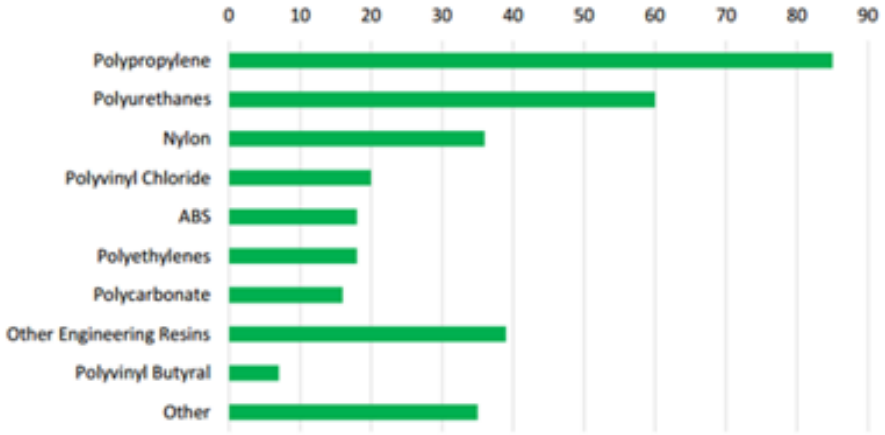

Fig 1.6. The percentage of plastic materials used in light vehicles[49]

Due to the lighter weight and the better impact resistance of ABS even at low temperature compared to other plastics, many parts of cars such as intrumental panels, body parts, wheel covers, and dashboards are made of ABS.

Some other significant applications in industry to the use of ABS are protective head gear,motorcyle helmet, protective cover of cell phones, and some fitting tools as depicted in Fig 1.7.

Fig 1.7. Various industrial applications of ABS

The ABS material is generally used as structural parts that can be possibly subjected to accidental impact loads; consequently, the significance of understanding the mechanical response of ABS under impact loads is a growing demand.

1.2 Background

For several years, deriving a constitutive model for the characterizaion of strain rate and pressure dependent material behavior of amorphous thermoplastics and capturing their complex stress-strain features such as intrinsic yield drop or strain softening and strain hardening have been receiving a considerable attention. There have been many experimental and theoretical studies focused on developing the reliable material models not only to identfy the strain rate response of amorphous thermoplastics subjected to various stress states including uniaxial tension,uniaxial compression and shear, but also to attain the strain softening and strain hardening behaviors observed in their stress-strain curves.

The initial investigations of strain rate dependent material behavior of amorphous thermoplastics began with an effort to obtain their yield stress at different strain rates and temperatures rather than their stress- strain features on the basis of molecular approach.

In 1936, the first study that is devoted to the determination of material behavior of amorphous thermoplastics with strain rate and temperature was done by Eyring[50] who claimed that chain macromolecules rotate to one another with an energy barrier. When that energy barrier is exceeded due to a stimulated shear stress to a material, a stimulated shear stress ,plastic flow or changes in the locations of chain macromolecules occur and he proposed that the plastic flow takes place through only a single stage thermally activated process. He formulated his theory as shown below.

$$\dot{\gamma} = \dot{\gamma}_0 \, exp\left(-\frac{\Delta H}{RT}\right) sin\, h\left(\frac{\Omega\tau}{RT}\right) \tag{1.1}$$

Where ΔH is the energy barrier to flow, R is Boltzman's constant, T is actual temperature, Ω is activation volume, τ is shear stress, $\dot{\gamma}$ is shear strain rate and $\dot{\gamma}_0$ is pre-exponential factor. Nevertheless, his theory is only capable of capturing the yield stress as a function of strain rate in a linear form. As a matter of fact that the relationship between yield stress and strain rate is hyperbolic in amorphous thermoplastics [51].

In 1964, there is more than one deformation mechanism observed on the starin rate dependent material behavior of PMMA by Bauwens and Crowet[52] after tensile tests were performed on PMMA at different strain rates from $2.6x10^{-5}$ s^{-1} to $1.3x10^{-2}$ s^{-1}. They concluded that Eyring's model that is based on only one stage thermally activated deformation mechanism was not successful to predict the strain rate response of PMMA.

In 1965, Roetling [53] carried out tensile tests on the same material (PMMA) but under high strain rates up to $10s^{-1}$ and he also deduced that Eyring's theory did not provide any good agreements as compared to his experimental findings.

After that, analogous experimental findings were reported for various amorphous thermplastics such as PC,PVC and PEMA [54-58].

In 1966, Robertson[59] took the actual structural changes caused by an applied shear stress into account based on intermolecular and intramolecular forces. He theorotically obtained the strain rate dependent material behavior of two different amorphous thermoplastics(polystyrene and polymethyl methacrylate) under tension and compared them to the experimentally measured data. Nevertheless, his theory was unable to estimate the behavior of amorphous thermoplastics over a wide range of strain rates.

In 1968, Haward [60] divided the deformation mechanism of amorphous thermoplastics into various stages such as initial stiffness, viscous flow and rubber elasticity. His model uses a Hookean spring for initial stiffness, Eyring dashpot for viscous flow and rubber elasticity spring shown in Fig 1.8.

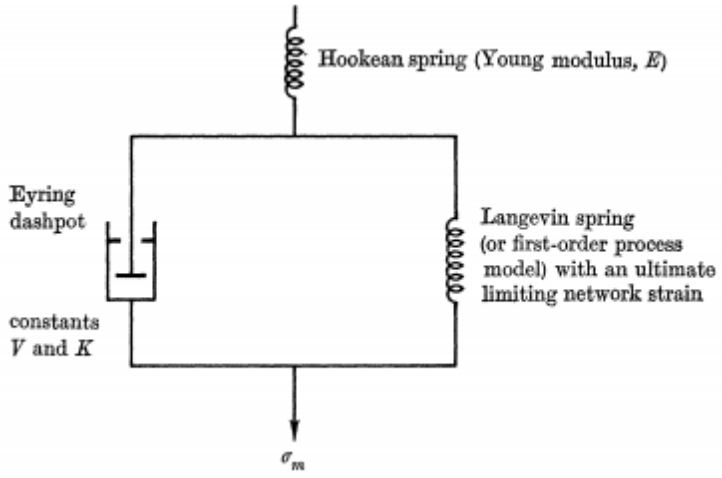

Fig 1.8. Shematic representation of Haward's model[60]

In 1969, depending on the experimentally identified strain rate response of PVC (Polyvinyl chloride) and PC(polycarbonate) tested over a wide range of strain rates from 10^{-5} s^{-1} to 1 s^{-1} under

uniaxial tension, Bauwens and his team [58] rearranged the Eyring's constitutive model (eq.1) and reformulated as written below:

$$\sigma_y = \tilde{A}\left[ln\left(2\tilde{C}\dot{\varepsilon}\right) + \frac{Q}{RT}\right] \tag{1.2}$$

where Q is the replacement of ΔH , σ_y and $\dot{\varepsilon}$ are the tensile yield strength and axial strain rate, respectively. A and C are combined parameters. While their model was applicable to the strain rate behavior of PC, a considerable discrepancy was observed for PVC at high strain rates.

In 1970, Duckett[61] expanded the theory of Robertson by the consideration of pressure influence on the behavior of amorphous thermoplastics; therefore, he successfully predicted the yield stress variation of amorphous poly(methylmethacrylate) (PMMA) with strain rate excluded high strain rates like Robertson's.

In 1973, Argon[35] decomposed the plastic flow mechanism of amorphous thermoplastics into two sepate stages such as intermolecular resistance and entropic resistance. He proposed that the entropic resistance is an actual reason behind the observed strain hardening behavior in amorphous thermoplastics and he represented this entropic resistance deformation stage with a Langevin spring based on rubber elasticty in his constitutive model. Also , pressure dependence and temperature effect on the material behavior of amorphous thermoplastics were considered in his model. His theory gives an expression of shear stress as a function of shear strain as indicated below:

$$\frac{\tau}{\mu} = \frac{0.077}{(1-v)}\left\{1 - \frac{16(1-v)}{3\pi\mu\omega^2 a^3}kT\left[ln\left(\frac{\dot{\gamma}_0}{\dot{\gamma}}\right) - \frac{0.15\mu a^3(\omega-\omega_c)^2(p/\mu)}{kT}\right]\right\}^{6/5} \tag{1.3}$$

where μ is shear modulus,υ is the poisson's ratio, k is the Boltzman's constant, a is the geometric parameter, p is the hydrostatic pressure and ω is the angular rotation of chain segments.

The model provided remarkably good agreement when compared to the experimentally measured the strain rate dependent material behavior of four different amorphous thermoplastics including poly-methyl-methacrylate, polystyrene, polycarbonate of bisphenol and polyethylene-terephthalate at strain rates ranging from low to moderate. Nonetheless, his model requires the user to know the variation of shear modulus with strain rate over a wide range.

In 1974,the another notable attempt was made by Bowden[62]. His approach is based on the modelling of dislocations of chain macromolecules.

In the1980s, a significant amount of attention started to be given to the development of material models for amorphous thermoplastics based on the original approaches of Haward and Argon because it was noticed that there was still a great need to more profound understanding of strain rate response of amorphous thermoplastics, after comparing their experimental investigations with the existing theories.

In 1986, Boyce focused on large inealastic strain rate dependent deformation behavior of amorphous thermoplastics that is seperated into two stages, such as macromolecular structure and micromolecular plastic flow in her proposed material model[63]. In 1988, the previous work of Argon was expanded by Boyce[25].

In 1993, Arruda and Boyce[64] developed a constitutive model on the basis of Argon's strain rate and temperature dependency concept and rubber elasticity for strain hardening in amorphous thermoplastics. The Argon's plastic flow was represented with a viscoplastic dashpot and they modelled the rubber elasticity based on the proposed eight chain network model in their constitutive material model as depicted below.

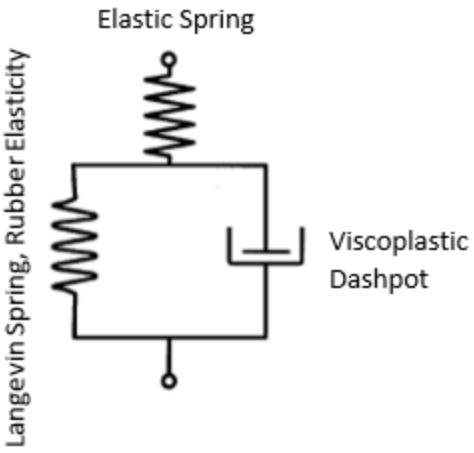

Fig 1.9. Schematic illustration of the proposed model of Arruda[64]

In 1993, Arruda attempted to find out how applicable their previously proposed model[64] to the characterization of anisotropic material response of amorphous polymers in all aspects including rate, temperature, pressure dependency, strain softening and strain hardening. It was concluded that their model was also well applicable to anistropic material response[65].In 1995, Arruda revised the Argon's theory and made some modifications after evaluating the strain rate and temperature influences on the material behavior of amorphous PMMA[66].

In 2000, Boyce [67] devepoled a new constitutive model for strain rate and temperature dependent material behavior of amorphous thermoplastics by decomposing their total stress- strain behavior into two parts, such as intermolecular resistance and molecular network resistance and a contribution of each resistance to the total stress-strain response was formulated separately ,as shown in Fig 1.10. This material model has been widely used in current works.

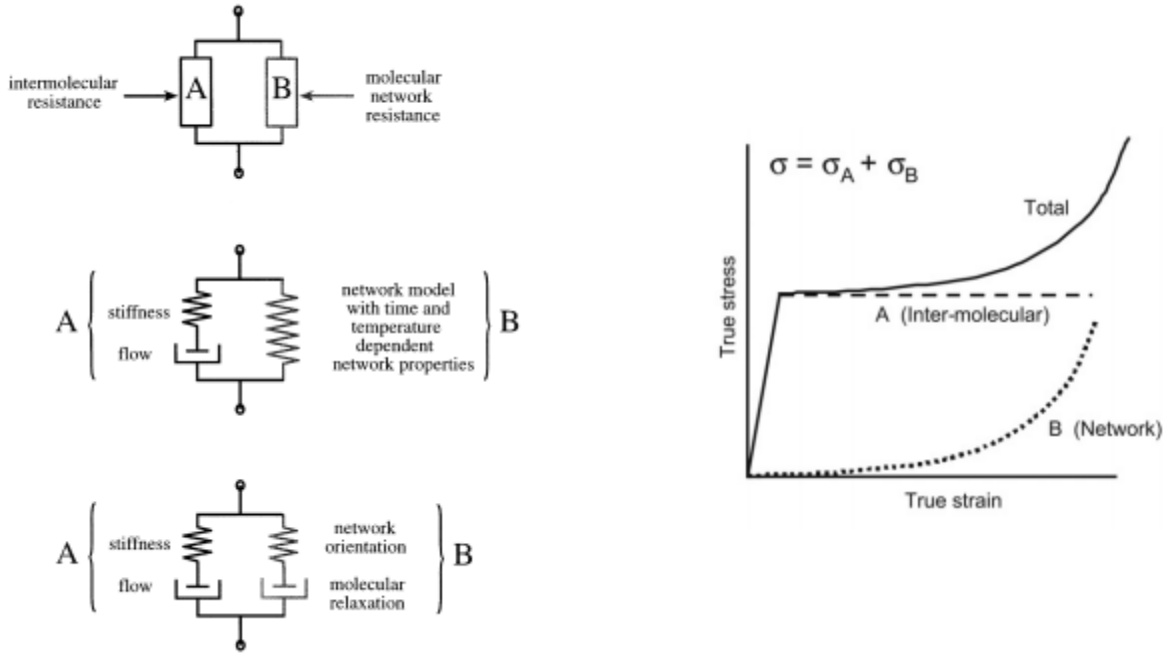

Fig 1.10. Schematic representation of the proposed model of Boyce and contribution of each resistance to total response[67]

This material model counts that deformation gradients of both parts (F_A and F_B) are kinematically identical to each other and equal to the total deformation gradient (F) of the material that can be written as:

$$F = F_A = F_B \tag{1.4}$$

where $F=\Delta_x p$, x is the initial position of material point and p is the actual material point position. Intermolecular resistance part is seperated into two various deformation stages (elastic and plastic) to model the effect of initial elastic stiffness on entire material response and the influences of strain rate and temperature on plastic flow, respectively. Therefore, the total deformation gradient of intermolecular resistance component can be expressed in terms of those elastic and plastic deformation gradients as follows:

$$F_A = F_A^e \cdot F_A^p \tag{1.5}$$

Furthermore, elastic and plastic deformation gradients can be described with respect to rigid body rotations and elongations as written below

$F_A^e = V_A^e \cdot R_A^e$ and $F_A^P = V_A^p \cdot R_A^p$ (1.6)

In accodance with kinematics, velocity gradients of intermolecular resistance component can be defined as:

$L_A = \dot{F}_A \cdot F_A^{-1}$ (1.7)

where $L_A = L_A^e + \tilde{L}_A^p$ and leads to $L_A = \dot{F}_A^e \cdot F_A^{e^{-1}} + F_A^e \cdot \dot{F}_A^p \cdot F_A^{p^{-1}} \cdot F_A^{e^{-1}}$ (1.8)

additionaly, L_A^e and $\tilde{L}_A^p$ elastic and plastic velocity gradients can be expressed in terms of elastic and plastic strain rate tensors, as well as spin tensors as written below:

$L_A^e = D_A^e \cdot W_A^e$, where D_A^e and W_A^e represent symmetric elastic strain rate tensor and symmetric elastic spin tensor, respectively.

$\tilde{L}_A^p = \tilde{D}_A^p \cdot \tilde{W}_A^p$, where $\tilde{D}_A^p$ and $\tilde{W}_A^p$ represent symmetric plastic strain rate tensor and symmetric plastic spin tensor, respectively.

If it is assumed that $\tilde{W}_A^p$ is equal to 0 for an initial configuration of material [68], strain rate dependent plastic flow can be described as:

$\tilde{D}_A^p = \dot{\gamma}_A^p \cdot N_A$ (1.9)

where N_A is the normalized deviatoric stress and $\dot{\gamma}_A^p$ is the strain rate dependent plastic flow those can be defined as:

$N_A = \frac{1}{\sqrt{2}\tau_A} T_A'$ where τ_A is the equivalent deviotric stress defined as:

$\tau_A = \left[\frac{1}{2} T_A' T_A'\right]^{1/2}$ (1.10)

and $\dot{\gamma}_A^p$ can be described through thermally activated process as:

$\dot{\gamma}_A^p = \dot{\gamma}_0^A \, exp\left[-\frac{\Delta G(1-\tau A/s)}{k\theta}\right]$, where s is the shear resistance and s=0.15*(shear modulus)^4 [25, 67].

Finally, a stress contribution of intermolecular resistance part(A) on the total stress response can be written in terms of elastic constants, Hencky strains and volumetric changes as written below:

$$T_A = \frac{1}{J_A}\mathcal{L}^e[InV_A^e] \tag{1.11}$$

where V_A^e and $\mathcal{L}^e$ are representations of Hencky strain and elastic constants, respectively. Additionaly, $J_A = det(F_A^e)$ is a volume change in structure.

The eq(1.11) can also be expressed in terms of Cauchy stress and elastic left Cauchy-Green deformation tensor [69] by considering compressible Neo-Hookean material model[70] for large elastic deformations as follow:

$$\sigma_A = \frac{1}{J_A^e}(\lambda_0 InJ_A^e I + \mu_0[B_A^e - I]) \tag{1.12}$$

where λ_0=elastic modulus, μ_0=poisson's ratio, I=second order unit tensor

Network resistance part (B) is assessed through decomposing it into two parts, including network orientation and molecular resistance. Basically, this part uses the eight-chain rubber elasticity formulation[71]. All deformation and velocity gradients can be described in the same manner of intermolecular resistance part(A) ; therefore, we here write down only the final expression that obtains the correlation between stress and stretch as documented below:

$$T_B = \frac{1}{J_B}\frac{nk\theta}{3}\frac{\sqrt{N}}{\tilde{\lambda}_N}\mathcal{L}^{-1}\left[\frac{\lambda_N}{\sqrt{N}}\right]\left[\tilde{B}^N - \left(\tilde{\lambda}_N\right)^2 I\right] \tag{1.13}$$

where nkθ is the initial elastic modulus of strain hardening, N is the number of rigid links, $\tilde{\lambda}_N$ is thw stretch for each chain and be calculated from $\tilde{\lambda}_N = \sqrt{\frac{1}{3}tr\left(\tilde{B}_N\right)}$, and $\mathcal{L}^{-1}$ is the inverse function

of Langevin spring and described as $\mathcal{L}(\beta) = cot(\beta) - {}^{1}/_{\beta}$

Eventually, the total response of material is $T=T_A + T_B$ (1.14)

The accuracy of the developed constitutive model was evaluated through the comparisions of experimental measurements and it was deduced that the model was enable to capture stress-strain features of amorphous thermoplastics under different strain rates and temperatures. However, the maximum strain rate used in their experiments was $1s^{-1}$.

In 2003, Anand [72] accomplished the prediction of the stress-strain features of amorphous polycarbonate,such as strain softening and strain hardening at one certain strain rate.

Nevertheless, none of the proposed constitutive models mentioned above for the characterization of rate dependent material behavior of amorphous thermoplastics is not capable of capturing stress-strain state at high strain rates[73].

In 2007, Richeton[9] successfully developed a new cooperative model based on the Ree-Eyring's and the previously proposed model of Bauwens-Crowet[58] to investigate the yield behavior of amorphous thermoplastics over a wide range of strain rates and temperatures. He expressed his model in a straightforward mathematics as a function of strain rate and temperature and succeeded in verifying his model by comparing his theoretical findings with the experimentally obtained and documented uniaxial compressive yield stresses of three polycarbonate(PC), polymethylmethacrylate (PMMA), and polyamideimide (PAI).The significance of his model is to almost perfectly predict the yield stresses of amorphous thermoplastics even at high strain rates, which has never been accomplished before. The schematic representation of his model shown in Fig 1.11.

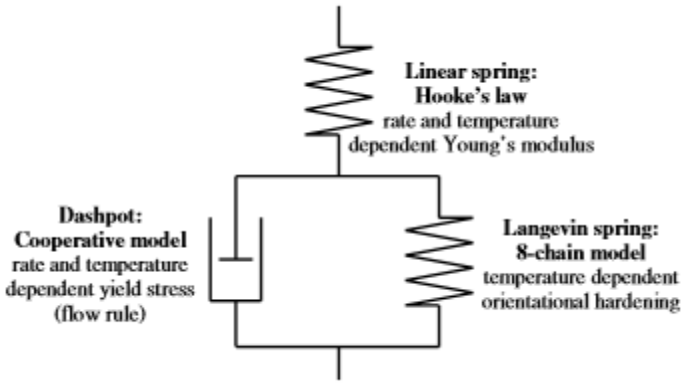

Fig 1.11. Schematic illustration of Richeton material model[9]

Strain Rate Dependent Material Behavior of ABS (Acrylonitrile-Butadiene-Styrene)

The strain rate response of ABS either under tension or compression has been identified over a wide range of strain rates by several researchers.

Walley and Field[101] carried out compression tests on ABS under six different strain rates ranging from low to very high and they documented their experimental findings as shown in Fig 1.12.

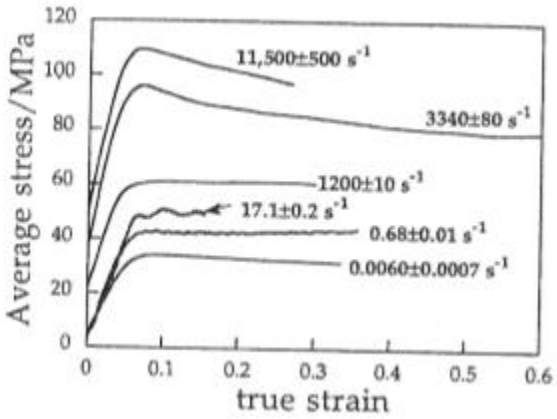

Fig 1.12 Compressive true stress-true strain curves for ABS at various strain rates.[101]

They claimed that ABS experiences neither strain softening nor strain hardening under compression at all strain rates. The compressive yield stress of ABS as a function of strain rate was reported and tabulated as shown in Fig 1.13 and Table 1.1, respectively.

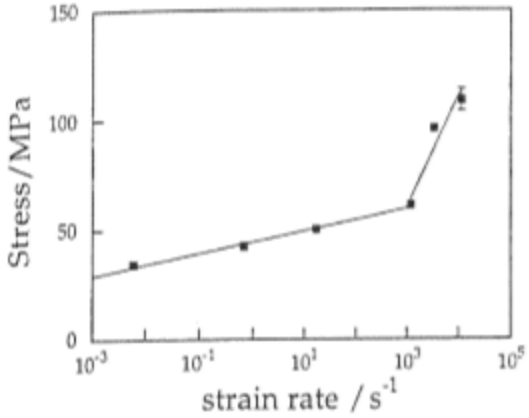

Fig 1.13. Relationship between strain rates and corresponding compressive yield stresses for ABS[101]

Table 1.1. Compressive yield strength of ABS (MPa) as a function of strain rate[101]

Polymer	0.006 (1/s)	0.68 (1/s)	17.1 (1/s)	1200 (1/s)	3340 (1/s)	11500 (1/s)
ABS	34.2±0.8	42.5±0.5	50±1	61±0.5	96±1.5	109±5

They observed a drastic rate sensitivity change for ABS under compression after strain rate of 1200 (1/s) as seen in Fig 1.13.

Duan[102] investigated the material behavior of ABS under compression at three different very low strain rates and two distinct high strain rates as illustrated in Fig 1.14 and Fig 1.15 ,respectively.

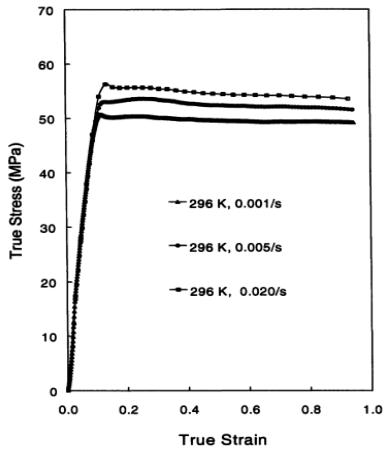

Fig 1.14 Compressive true stress-true strain curves for ABS under low strain rates[102]

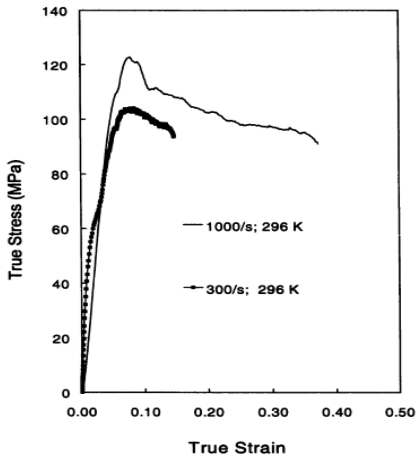

Fig 1.15 Compressive true stress-true strain curves for ABS under high strain rates[102]

While the feature of compressive true stress-true strain curves of ABS was identical at very low strain rates, he observed a considerable change at high strain rates. In comparison to the documented compressive strength of ABS as a function of strain rate by Walley and Field, he reported higher compressive strength for ABS.

The compressive strain rate response of 3D-printed ABS under high strain rates from 500 s^{-1} and 2000 s^{-1} was also reported by [103] Owolabi. He attained five different strain rates during his compression tests. Compressed ABS specimens at various strain rates are illustrated in Fig 1.16.

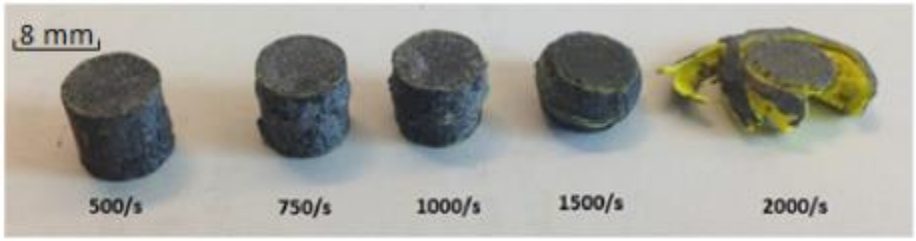

Fig 1.16. Compressed 3D-Printed ABS specimens at high strain rates

While the compression test data of 3D-printed ABS was obtained from software based optical method digital image correlation (DIC) for the strain rates of $500s^{-1}$, $750s^{-1}$ and $1000s^{-1}$, the Split Hopkinson Pressure Bar (SHPB) was utilized for the strain rates of $1500s^{-1}$ and $2000s^{-1}$.

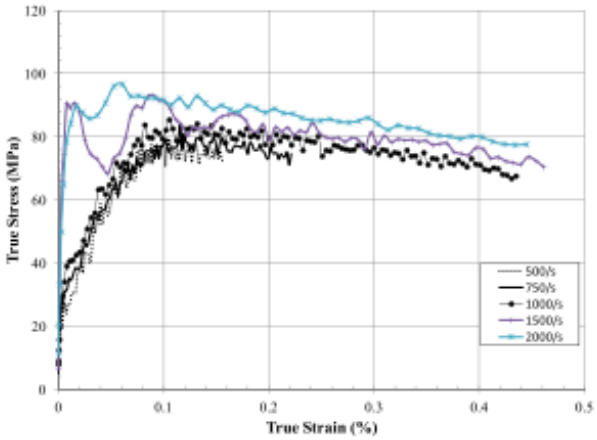

Fig 1.17. Compressive true stress-true strain curves for 3-D printed ABS at different strain rates[103]

The compressive strain rate dependent material behavior of 3D-printed ABS at high strain rates is shown in Fig 1.17. He reported the compressive strength of 3D-printed ABS as 91.6 MPa and 89.7 MPa for strain rates of $1500s^{-1}$ and $2000s^{-1}$, respectively. It was claimed that 3D printed ABS shows strain softening followed by strain hardening in its stress state under compression at strain rates of both $1500s^{-1}$ and $2000s^{-1}$.

Perhaps, Dean and Wright[104] were the first researchers who characterized the strain rate response of ABS under tension over a wide range of strain rates varying from very low ($0.0006\ s^{-1}$) to moderate ($104\ s^{-1}$) and they documented their findings as shown in Fig 1.18.

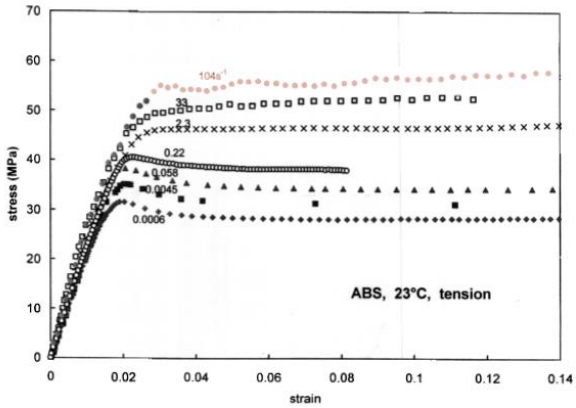

Fig 1.18. Tensile stress-strain curves for ABS at various strain rates[104].

From the obtained tensile stress-strain curves of ABS under different strain rates, it was deduced that the tensile elastic moduli of ABS like its yield strength was also strain rate dependent and they tabulated the tensile elastic moduli of ABS as a function of strain rate as shown in Table 1.2.

Table 1.2. Tensile elastic modulus of ABS as a function of strain rate

E(GPa)	Strain rate (s^{-1})
2.27	0.0006
2.30	0.004
2.34	0.06
2.36	0.2
2.40	2.3
2.44	33
2.47	104

Additionally, they carried out uniaxial compression and shear tests on ABS under quasi-static conditions and reported the different behavior of ABS in tension and in compression as well as in shear, as indicated in Fig 1.19.

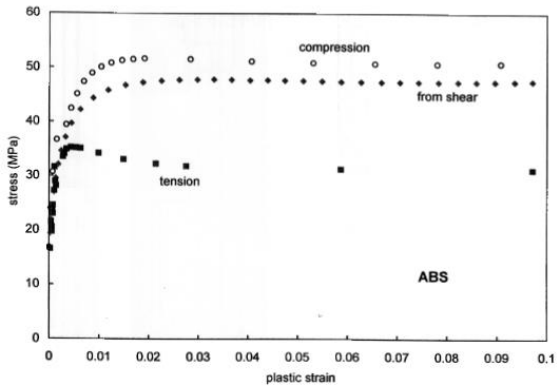

Fig 1.19. True plastic tensile, compressive and effective shear stress-strain curves for ABS

They stated that the reason behind the relatively low strength of ABS under tension compared to compression is the formation of cavities near rubber particles that can only be took place under tension. Cavities cause a stiffness reduction in ABS under tension that leads to a decrease in the strength of ABS.

Yin[105] evaluated the high deformation behavior of ABS through conducting tension tests in Split Hopkinson Tension Bar (SHTB) under the high strain rates of 600 s^{-1},1200 s^{-1} and 2200 s^{-1} . He plotted engineering strains against engineering stresses for each strain rate as shown in Fig 1.20.

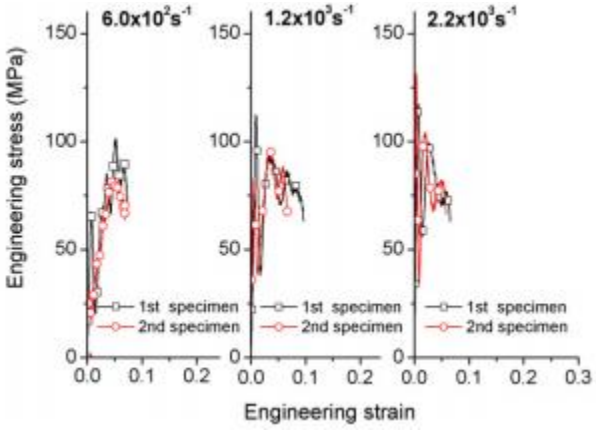

Fig 1.20. Engineering stress-strain curves for ABS at three different strain rates[105].

Like Dean and Wright, he also observed an increase in both elastic moduli and yield stress of ABS with an increased strain rate.

Anton[106] documented the tensile behavior of ABS for two different deformation rates of 1mm/min and 500 mm/min as shown in Fig 1.21 and Fig 1.22, respectively.

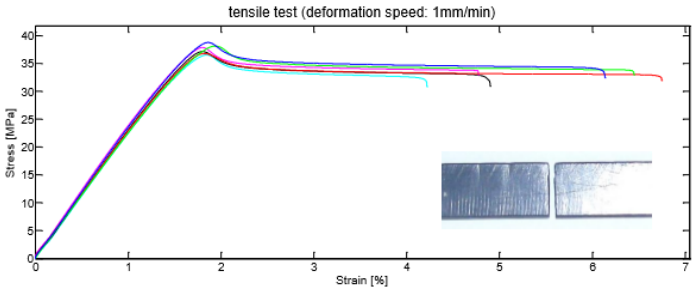

Fig 1.21. Stress-strain curve of ABS for deformation rate of 1mm/min

It was concluded that the fracture behavior of ABS is brittle and the necking area of ABS is barely distinguishable. He determined the lower yield stress and upper yield stress of ABS as 30

MPa and 38 MPa for the deformation rate of 1mm/min, respectively. He provided the elastic and plastic material properties as tabulated in Table1.3.

Table 1.3. Material behavior of ABS for deformation rate of 1mm/min[106]

yield stress	30 MPa	nominal strain at break	6,5 %
tensile modulus	2200 MPa	stress at break	34 MPa
possions ratio	0,3 (assumption)		

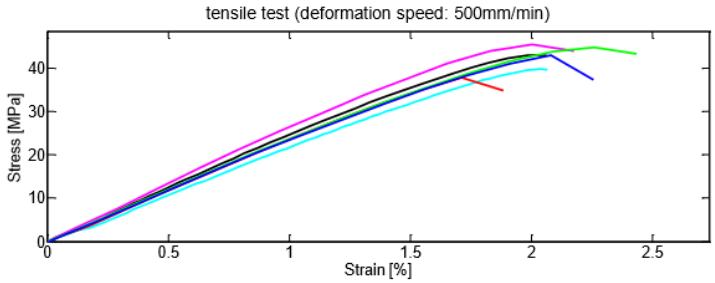

Fig 1.22. Stress-strain curve of ABS for deformation rate of 500 mm/min[106]

For the tensile material behavior of ABS under the deformation rate of 500 mm/min, it was claimed that there was no good correlation between conducted 6 tension tests in terms of yield stresses of ABS.

Louche[107] characterized the strain rate dependent material behavior of ABS at six various strain rates from 0.001 s^{-1} and 2 s^{-1} and provided the load-displacement curves of ABS for those strain rates as shown in Fig 1.23.

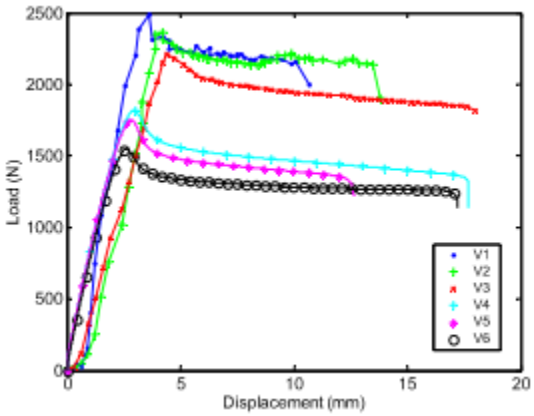

Fig 1.23. Tensile load-displacement curves for ABS (V1=2 s^{-1}, V2=1 s^{-1}, V3=0.2 s^{-1}, V4=3.10^{-2} s^{-1}, V5=1.10^{-2} s^{-1}, V6=1.10^{-3} s^{-1})[107]

Similar to previous researchers, he observed that higher deformation rates lead to higher tensile yield stress and tensile elastic moduli for ABS. He utilized an extensometer and digital image correlation tools to obtain tension test data and compared the extensometer data to digital image correlation data for one certain strain rate as indicated in Fig 1.24. He reported the yield stress of ABS as 39 MPa for this certain strain rate.

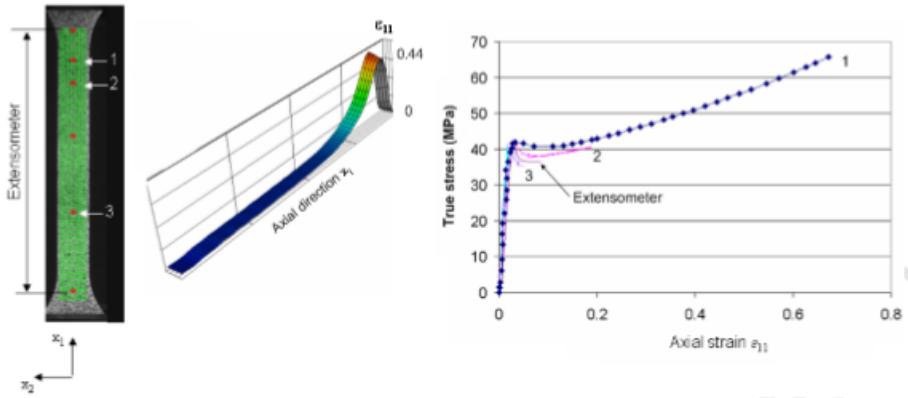

Fig 1.24. True stress-strain curve for ABS, extensometer vs. DIC[107]

He observed the strain softening and strain hardening material behavior in tensile true stress-strain curves of ABS. Moreover, he noticed a volume increase during deformation of ABS under tension.

Three has been no such a study found for the strain rate dependent material behavior of ABS under shear.

While there has been no numerical study dedicated for the strain rate response of ABS under compression, there has been only one numerical implementation of uniaxial tension test for ABS noticed in literature. Anton [106] simulated the material behavior of ABS under tension utilizing two distinct elastic -plastic material models such as MAT_PIECEWISE_LINEAR_PLASTICITY (Mat_24) and a newly developed SEMI-ANALTICAL MATERIAL MODEL for POLYMERS (SAMP-1) in LS-DYNA. Both material models use experimental data as an input to identify plastic material

behavior. He compared the experimental results with his numerical predictions as shown in Fig 1.25.

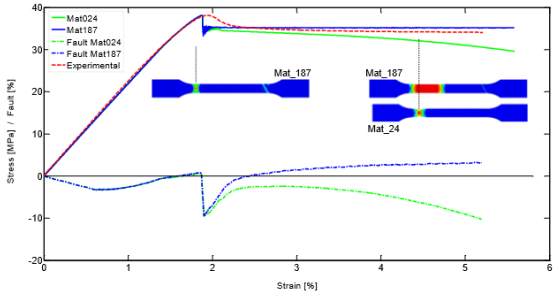

Fig 1.25. Experiment vs FEM for ABS under tension[106]

Identifying material behavior of ABS under different stress states such as tension, compression and shear does not reflect the actual material behavior of ABS that can only be characterized through simultaneously dictating all those stress states which can be accomplished by means of conducting 3-point bending and impact tests.

Material Behavior of ABS under Multiaxial Loads

Mechanical response of ABS subjected to multiaxial loads including 3-point bending and impact provides a direct concrete detail regarding its actual material behavior. Nevertheless, neither dynamic or static 3-point bending test nor its numerical implementation has been performed on ABS so far.

Louche [107] studied on a heel of woman's shoe made of ABS to experimentally characterize its impact response and to numerically predict its impact behavior. The representation of woman's shoe heel is depicted in Fig 1.26.

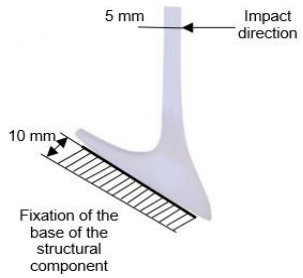

Fig 1.26. Impacted Woman's shoe heel made of ABS.

He determined Johnson Cook plasticity material parameters including hardening coefficient and utilized them in his impact simulations. He believed that strain rate and temperature effects on impact response of ABS can readily be taken into account by this material model. He compared his experimental findings with his numerical implementations in terms of impact force vs. time and displacement vs. time as shown in Fig 1.27.

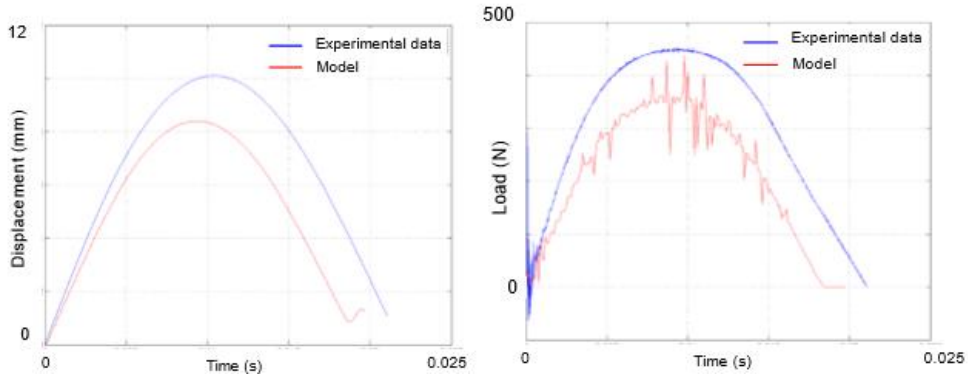

(a) (b)

Fig 1.27. Experiment vs FEM for impact response of woman's heel made of ABS[107]

After comparing his experimental results with his numerical predictions, he pointed out that Johnson Cook material model assumes an identical material behavior in tension compared to compression, as well as shear and he strongly recommended to identify material behavior of ABS under compression and/or shear and to include them in material model for more accurate predictions. Therefore, he addressed the Drucker-Prager plasticity material model that is capable of accounting strain rate effect and dissimilar material behavior of ABS under tension and compression.

However, Dean and Wright [104] defined liner Drucker-Prager plasticity parameters for ABS including pressure sensitivity coefficient and hardening factor that were obtained from shear and compression tests conducted under the same strain rate and they used those parameters in numerical implementation of indentation tests performed under monotonic loading with different

tests speeds. They concluded that linear Drucker-Prager plasticity material model is not well applicable to describe the mechanical response of ABS under monotonic multiaxial loading conditions. They compared the measured load-displacement curves with various monotonic test speeds to numerical predictions as shown in Fig 1.28.

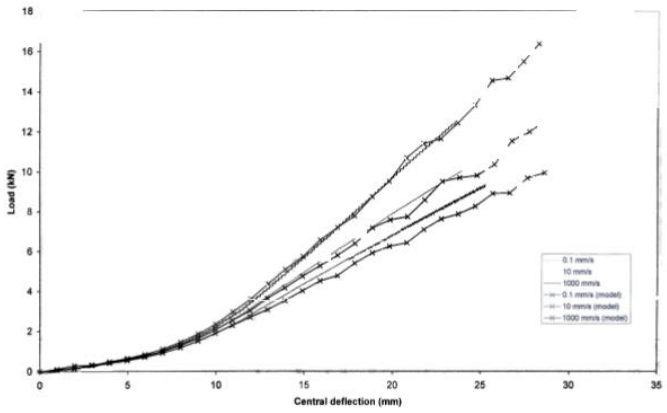

Fig 1.28. Comparisons of experimental load-displacement curves for ABS under different monotonic test speeds with numerical predictions.

Duan[102] is the only researcher who conducted impact experiments on 3 mm thick ABS specimen with circular shape under four different impact velocities varying from 1 m/s to 4.2 m/s and performed the numerical implementation of impact tests. In his impact experiments, he used 22.7 kg projectile with hemispherical nose. A catastrophic failure was observed in ABS for impact velocities above 1 m/s. Based on compressive data of ABS as a function of strain rate, he developed a mathematical model called DSGZ for the determination of material behavior of ABS under impact. His material model uses 9 coefficients and he attempted to validate his mathematical model with performing the numerical analysis of impact tests through user subroutine in Abaqus. Although his mathematical model was successful to capture the compressive stress-strain feature of ABS for low strain rates, the impact response of ABS was not well predicted by his model, particularly in terms of peak loads as shown in Fig 1.29 and Fig 1.30. Therefore, he emphasized

that only well predicting the material behavior of ABS either under tension or under compression does not signify the real material behavior of ABS under multiaxial loads.

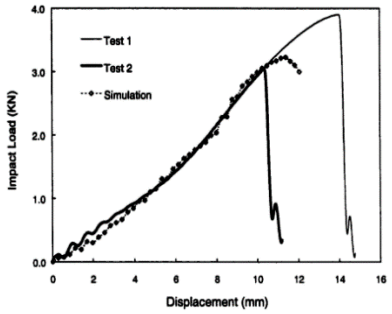

Fig 1.29. DSGZ vs. Experiment, impact load-displacement curves for ABS at 2 (m/s)

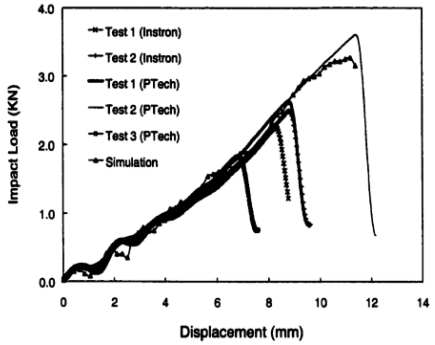

Fig 1.30. DSGZ vs. Experiment, impact load-displacement curves for ABS at 4.2 (m/s)

Numerical Implementation of Amorphous Thermoplastics like ABS under Multiaxial Loads

There have been still many open questions and difficulties for numerical implementation of impact tests of amorphous thermoplastics like ABS [108, 109] due to lack of available convenient material models in finite element codes that enable to define their complex material behaviors such as strain softening, strain hardening, strain rate dependency and dissimilar material behaviors under different stress states including tension, compression and shear. Thus, to fully determine mechanical response of amorphous thermoplastics to multiaxial loads, at least three mechanical tests need to be performed over a wide range of strain rates as shown in Fig 1.31 and

any material model utilized in any finite element code should have ability to handle strain rate dependent material behavior of amorphous thermoplastics under tension, compression and shear, simultaneously[10].

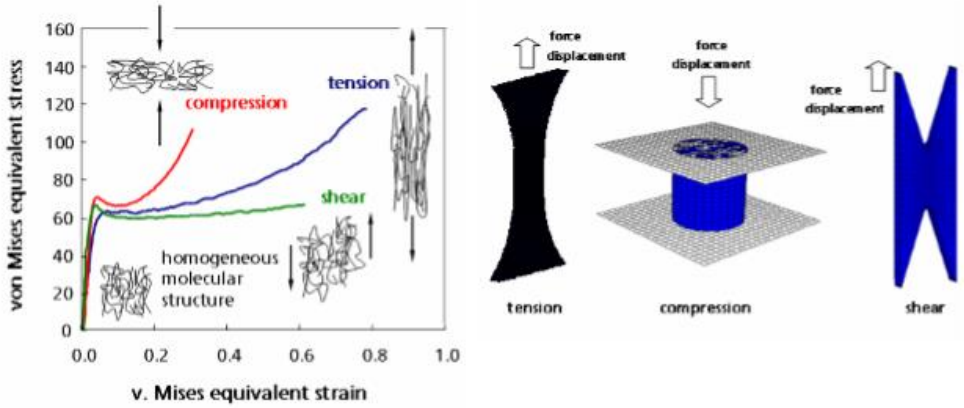

Fig 1.31. Necessary mechanical tests to fully determine mechanical response of amorphous thermoplastics under multiaxial load.[110]

Verification of material model used in finite element codes for the multiaxial mechanical response of amorphous thermoplastics can be accomplished through comparison of experimentally determined 3-point bending load-displacement curves with numerical predictions.

Kolling [111] focused on numerical analysis of material behavior for Polypropylene (PP) amorphous rubbery material under multiaxial loads. Firstly, he conducted tension, compression and shear tests on Polypropylene (PP) and he simulated the conducted mechanical tests utilizing semi-analytical material model for polymers (SAMP-1) and compared his numerical predictions with experimental results. After that, with using the same material model, the mechanical response of Polypropylene (PP) under 3-point bending was numerically examined he compared the load-displacement curve measured from 3-point bending test with his numerical predictions as shown in Fig 1.32.

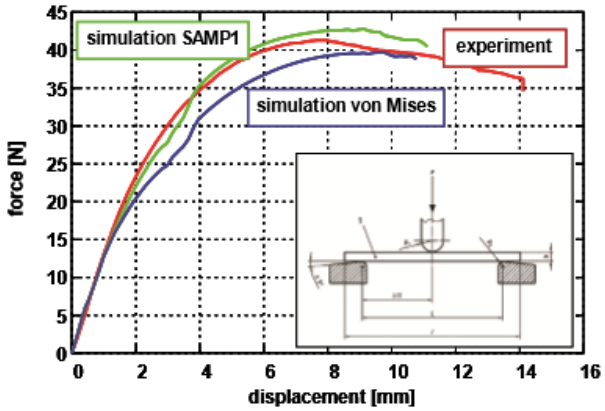

Fig 1.32. Experiment vs. FEM for Polypropylene (PP) under 3-point bending[111]

He run two distinct simulations using the same material model (SAMP-1) with taking different material behavior under tension, compression and shear into account and without considering the dissimilar material behavior under those stress states (Von-Misses) as indicated again in Fig 1.32. After comparisons, he stated that SAMP-1 material model is highly capable of capturing almost all deformation mechanism of Polypropylene (PP) including strain rate effect, pressure dependency, strain softening and strain hardening.

Daiyan [112] conducted low velocity impact tests on Polypropylene (PP) and he mainly focused on its numerical implementations. The impact behavior of Polypropylene (PP) was predicted using the SAMP-1 in LS-DYNA. He favorably compared his experimental results with his numerical predictions as indicated in Fig 1.33.

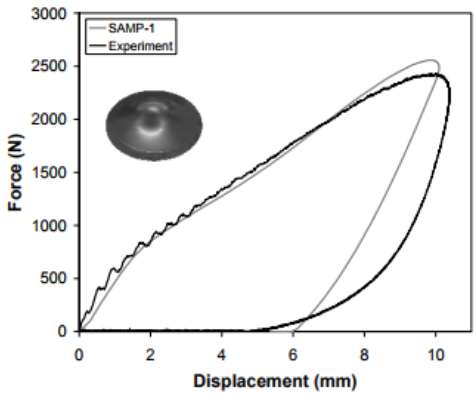

Fig 1.33. Comparisons of impact force-displacement curves for Polypropylene (PP) under impact velocity of 3 m/s

There was a very good correlation found between experimental results and numerical predictions (Fig 1.33).

Polanco[113] determined the material parameters of currently used constitutive material model for thermoplastics formulated step by step in our literature review (background) for Polypropylene (PP) amorphous rubbery material depending on tension and compression test data as a function of strain rate. He firstly simulated the material behavior of Polypropylene (PP) subjected to 3-point bending under various deformation rates by means of using the described material parameters in user subroutine in Abaqus. His comparisons for the mechanical response of Polypropylene (PP) under 3-point bending is shown in Fig 1.34.

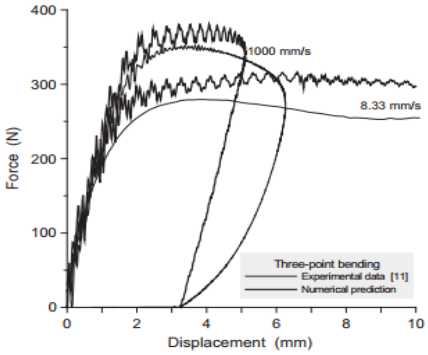

Fig 1.34. Experiment vs. FEM for Polypropylene (PP) under 3-point bending at various deformation rates[113]

Additionally, he carried out low velocity impact tests on Polypropylene (PP) at two various impact velocities of 1 m/s and 2 m/s. Similar to numerical implementation of 3-point bending tests, he compared his experimental impact data with his numerical data as shown in Fig 1.35.

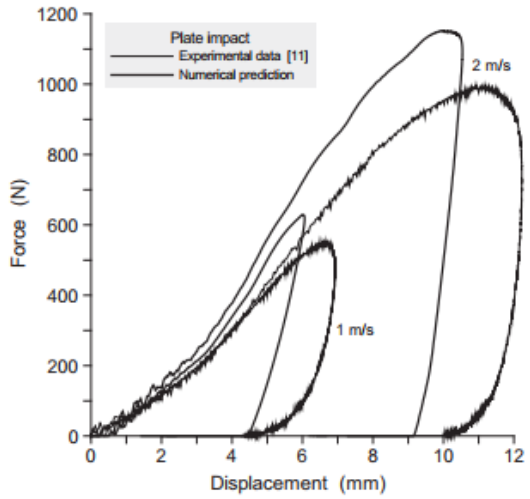

Fig 1.35. Comparisons of impact force-displacement curves for Polypropylene (PP) under different impact velocities[13]

He emphasized that this material model can be improved by considering more complex yield surface definition and thoroughly capturing strain hardening or strain softening during plastic deformation.

In this section, we primarily provided details regarding the numerical implementation of multiaxial material behavior of Polypropylene (PP) amorphous rubbery material due to lack of numerical implementation of ABS under multiaxial loads. Nevertheless, both materials represent the same family of material group (amorphous rubber toughened thermoplastic).

1.3 Motivations

In the past four decades, the significance of utilizing polymer based materials, such as ABS, as an alternative to metals over a wide range of engineering applications, including automotive, aerospace, marine, safety helmets and electronic enclosures has been increasing drastically, due to their outstanding material qualities, such as light weight, high toughness and stiffness, good impact resistance and high strength. The most appealing material property of ABS is its extremely good impact resistance compared to other glassy polymers because randomly dispersed rubber particles in its structure lead to a considerable increase in its toughness and impact resistance. Therefore,

ABS is used as structural components in unique applications where good impact resistance is highly desired. Nonetheless, amorphous thermoplastics exhibit highly complex material behaviors subjected to mechanical loads because of randomly arranged macromolecules in their natural structures.

It is known that the material properties of amorphous thermoplastics are significantly dependent on strain rate and temperature. Furthermore, their material behaviors are susceptible to pressure implying that their material behavior under tension is not the same under compression, nor shear. In addition, true intrinsic yield drop and strain hardening are observed in their stress-strain features under tension and compression.

Currently, developing a constitutive material model that possesses the ability to take all those complex material behaviors with respect to all aspects stated above into account is of high interest. It is compulsory to know the material behaviors of amorphous thermoplastics at least under three dissimilar stress states, including tension, compression and shear over a wide range of strain rates for safe design of amorphous thermoplastics. A need for more comprehensive understanding of their strain rate dependent behaviors especially under high strain rates and a lack of well applicable constitutive material models suggest an experimental investigation and numerical validation using empirical or semi empirical material models in finite element code. For this reason, we are motivated to experimentally characterize the stress-strain response of ABS under uniaxial tension, uniaxial compression and shear at different strain rates ranging from low to medium and to experimentally determine its impact behavior subjected to various impact energies, as well as, to utilize semi empirical material model in our numerical implementations for verification.

1.4 Objectives

The primary and direct target of this study was to successfully predict the actual mechanical response of ABS under impact at three various impact velocities, including 4.43 (m/s),5.775 (m/s) and 6.264 (m/s), and under 3- point bending at five different deformation rates varying from 0.005 (mm/s) to 10 (mm/s) through utilizing the newly developed semi-analytical material model for polymers (SAMP-1) in the explicit solver of LS-DYNA that requires tension, compression and shear test data over a wide range of strain rates.

The second aim of this research was to utilize two powerful Non-Destructive evaluation methods including ultrasonic C-Scan and laser scanning microscopy, to detect damage areas and surface imperfections, respectively after ABS specimens were subjected to impacts.

CHAPTER 2 EXPERIMENTAL SETUP

2.1 Uniaxial Tension

Tension tests were carried out based on ASTM D638-14, which is extensively used in defining the tensile properties of plastics, such as tensile strength, elastic modulus, elongation at yield and elongation at break[74] and the ABS tension test specimens were prepared from 6 (mm) thick plate as shown in Fig 2.1.

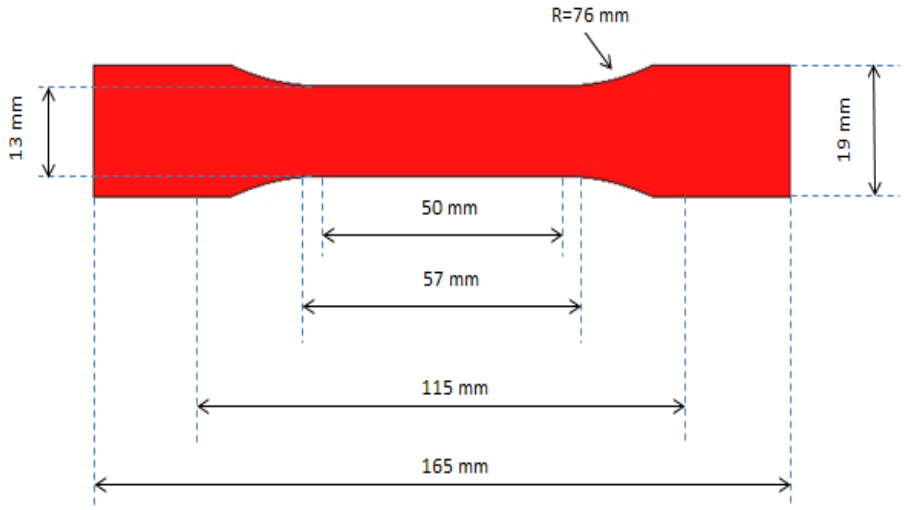

Fig 2.1. Dimensions of the ABS tension test specimen (dumbbell shape), t=6mm

Acquiring a tension test data from only grip separation does not provide any accurate results for plastic materials because of the following two reasons:

i. In general, plastic materials almost instantly attain their yield points corresponding to very small strains.

ii. Due to geometrical characteristic of the dumbbell shape, width of the tension test specimen is not uniform along its entire length and this non-uniform width leads to a different elongation rate between the narrow section and other sections.

We therefore obtained the tension test data using a longitudinal extensometer that is highly required to measure the tensile properties of plastic materials. The experimental setup for uniaxial tension is illustrated in Fig 2.2.

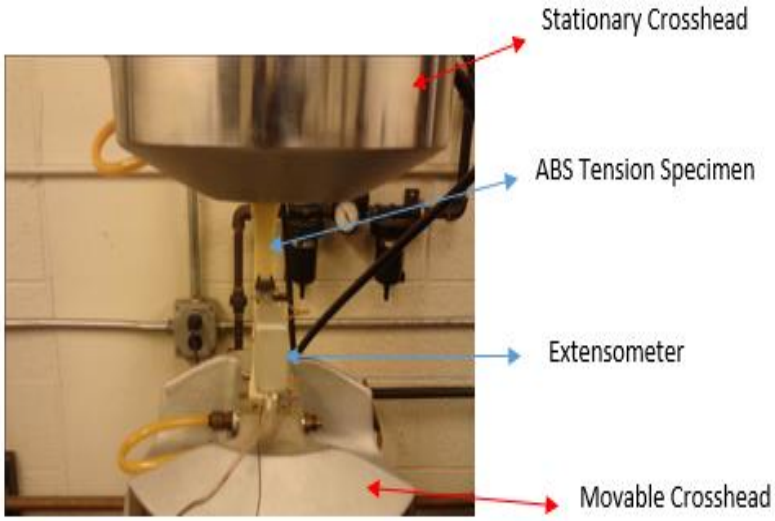

Fig 2.2. Experimental Setup of Uniaxial Tension Test

The stress-strain response of ABS under uniaxial tension was measured at five different strain rates varying from 0.0001 s^{-1} to 0.2 s^{-1} in MTC machine and five uniaxial tension tests were conducted for each strain rate. True stresses and their corresponding strains were calculated with the following well known formulas:

$$\sigma_{true} = \sigma_{nom} \times (1 + \varepsilon_x) \tag{2.1}$$

where σ_{true} is true stress, σ_{nom} is nominal stress, and ε_x is nominal longitudinal strain

$$\varepsilon_{true} = ln(1 + \varepsilon_x) \tag{2.2}$$

where ε_{true} is true longitudinal strain

The way of deriving true stress-true strain values documented above does not account for any volume change in structure throughout deformation. Nevertheless, as a matter of fact that the onset of crazing which is the actual reason for damage in rubber toughened amorphous thermoplastics like ABS causes voids near rubber particles which may result in a volume change

during deformation[75]. Consequently, the volume change needs to be taken into consideration in the determination of tensile true stress-true strain behavior of amorphous thermoplastics[76-81]. Hence, the software based optical method of digitial image correlation (DIC) was utilized to obtain true longitudinal and true transverse strains and true stressess were extracted based on transverse strains with an assumtion of transverse isotropy as shown below:

$$\sigma_{true} = \sigma_{nom} \times e^{-2\varepsilon_y} \tag{2.3}$$

where ε_y is the transverse strain and it is equal to the strain in the thickness direction ε_y with an assumption of transverse isotropy.

The ABS tension test specimens used in acquiring data from DIC were prepared again depending on the same ASTM standard but with different dimensions and thickness as illustrated in Fig 2.3.

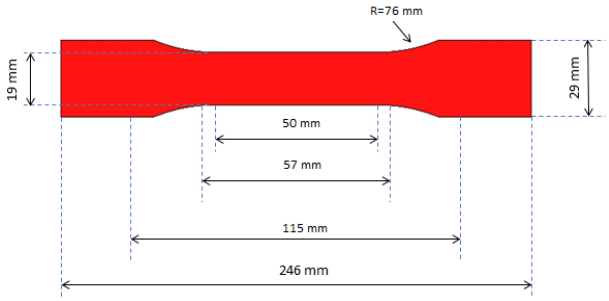

Fig 2.3. Dimensions of the ABS tension test specimen (dumbbell shape), t=12.7mm

True longitudinal and true transverse strains were obtained from DIC for the lowest two strain rates ($2x10^{-4}$ s^{-1} and $2x10^{-3}$ s^{-1}) and true stresses were calculated form the eq. (2.3) to observe the influence of volume changes on true stresses through the comparisons of true stresses and true strains calculated from extensometer data. The prepared ABS tension test specimen used in DIC is depicted in Fig 2.4.

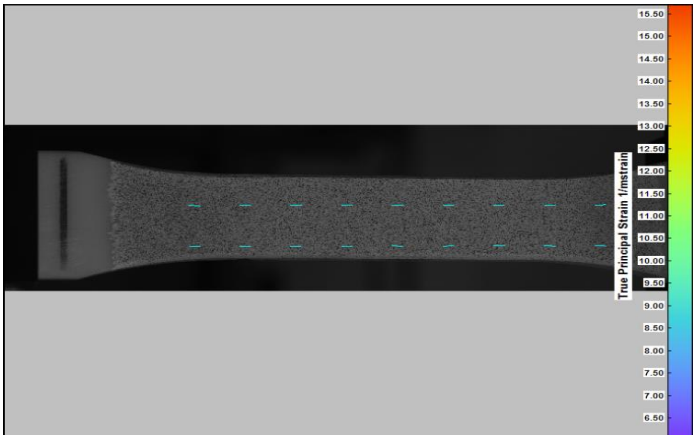

Fig 2.4. The illustration of ABS tension test specimen used in DIC

Furthermore, high strain rate uniaxial tension tests were carried out in high speed Instron test machine as shown in Fig 2.5.

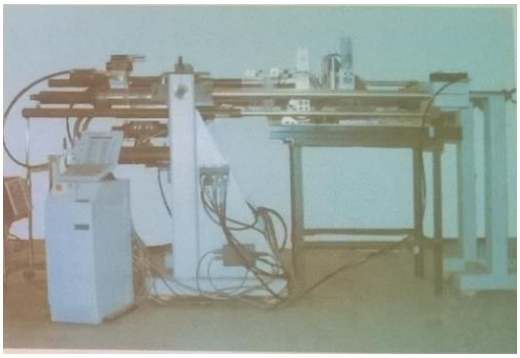

Fig 2.5. High Speed Instron Test Machine

During the high deformation uniaxial tensile tests, three various strain rates (10 s^{-1}, 30 s^{-1} and 45 s^{-1}) were attained. Tension test data for the strain rate of 45 s^{-1} including longitudinal and transverse strains were measured through biaxial strain gages placed on different locations along gage length where rupture was highly expected as illustrated in Fig 2.6.

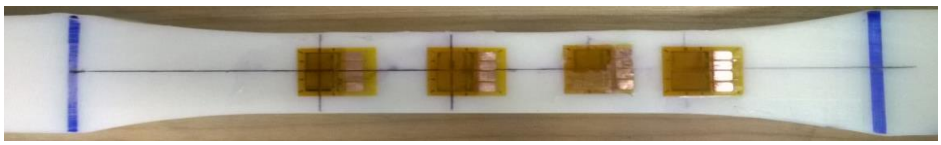

Fig 2.6 ABS tension test specimen with biaxial strain gages for strain rate of 45 s^{-1}.

For the attained strain rates of 10 s^{-1} and 30 s^{-1}, both longitudinal and transverse strain gages were utilized to obtain tension test data as shown in Fig 2.7.

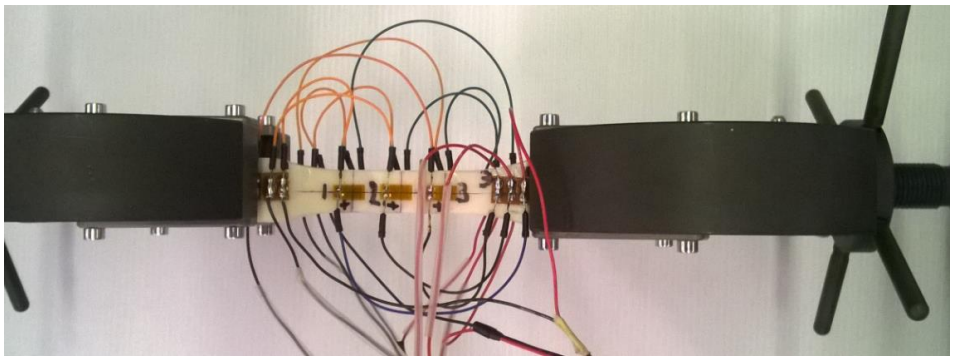

Fig 2.7. ABS tension test specimen with longitudinal and transverse strain gages for strain rates of 10 s^{-1} and 30 s^{-1}

2.2 Uniaxial Compression

In order to identify the strain rate dependent compressive material behavior of ABS, test specimens were prepared and the uniaxial compression tests were carried out based on ASTM D695-15[82].

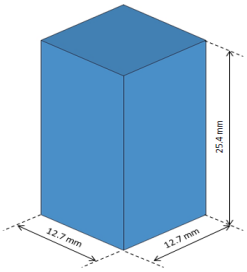

Fig 2.8. Dimensions of the uniaxial compression ABS test specimen (ASTM D695-15)

Uniaxial compression tests were performed under five various strain rates ranging from 0.0002 s^{-1} to 0.4 s^{-1}. and 5 tests were conducted for each strain rate. The all uniaxial compression test specimens were strained up to %78 calculated from the crosshead movement of platen. Uniaxial compression test setup is displayed in Fig 2.9.

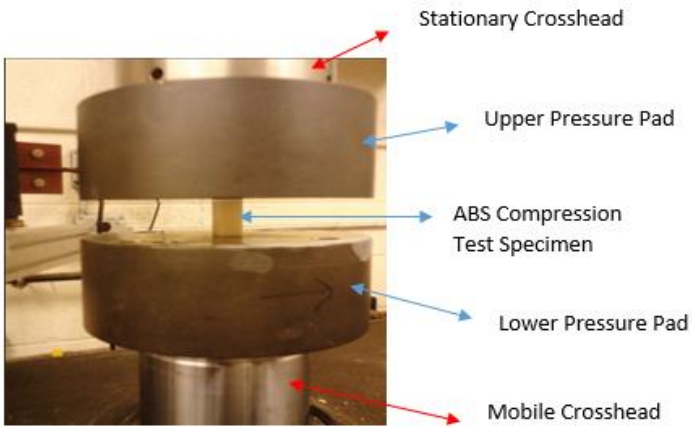

Fig 2.9. Experimental Setup of Uniaxial Compression Test

2.3 Shear

In general, a shear fracture is not observed in amorphous thermoplastics, such as ABS[83-85]. There are various types of shear test methods that utilize dissimilar shear test fixtures for the determination of shear behavior of plastics; nonetheless, nonidentical shear test fixtures provide different results. For this reason, shear response of amorphous thermoplastics is not counted for reliable design [86]. Although ASTM D5379 [87] is designed for the determination of shear properties of composite materials, it is also found to be well applicable to amorphous thermoplastics[86]. This test method is also known as the Modified Wyoming Iosipescu shear test method. The dimension of shear test specimen is shown in Fig 2.10.

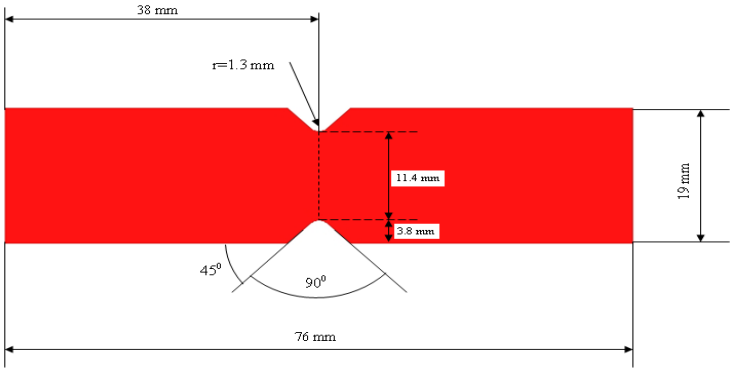

Fig 2.10. Dimensions of the ABS shear test specimen, t=3.18 mm

The shear stress-shear strain response of ABS was obtained from conducted shear tests under five different strain rates ranged from $4.4x10^{-4}$ s^{-1} to $8.77x10^{-1}$ s^{-1}. The utilized shear test fixture and the experimental setup of the shear test are shown in Fig 2.11 and Fig 2.12, respectively.

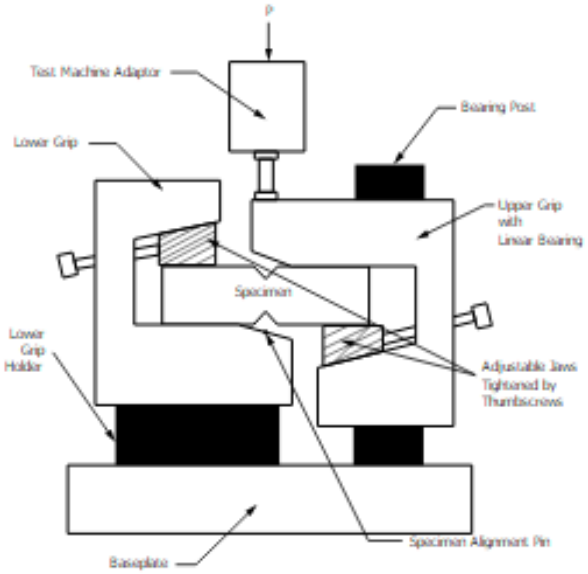

Fig 2.11. V-Notched shear test fixture[87]

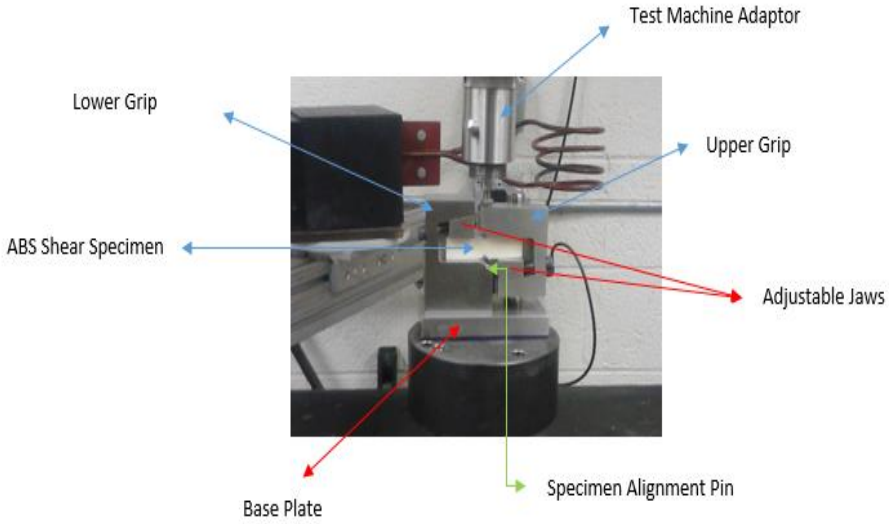

Fig 2.12. Experimental setup of the shear test

The digital image correlation (DIC) was also utilized to monitor the shear strain variations under two lowest shear strain rates ($4.4x10^{-4}$ s^{-1} and $4.4x10^{-3}$) to make sure our shear strain calculations obtained from dividing crosshead displacement by width of shear band. The monitored region on the ABS shear test specimen during shear tests is depicted in Fig 2.13.

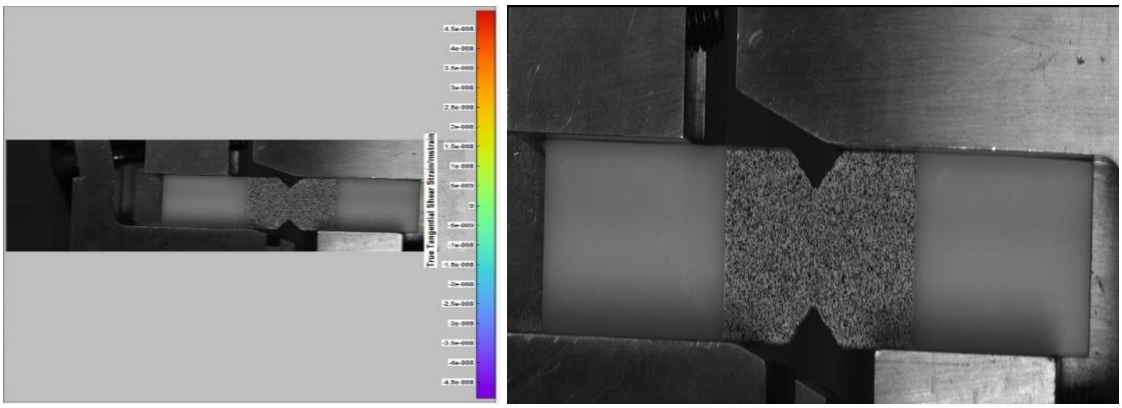

Fig 2.13. The monitored region on ABS shear test specimen

2.4 Three-Point Bending

The flexural material behavior of ABS was investigated by conducting 3-point bending tests under five different deformation rates varying from 0.005 (mm/s) to 10 (mm/s), based on ASTM D790[88]. The important aspect of conducting 3-point bending test on ABS that does not indicate analogous material behavior under tension, compression and shear, is to obtain more fundamental understanding of its mechanical response when subjected to tension, compression and shear stress states, simultaneously[37] and 3-point bending test is the simplest experimental approach to concurrently impose those three stress states.

Five 3-point bending tests were conducted for each deformation rate and 3-point bending ABS test specimens were bended up to 20mm. Geometrical specifications of the prepared 3-point bending ABS test specimen, loading nose and supports are depicted in Fig 2.14.

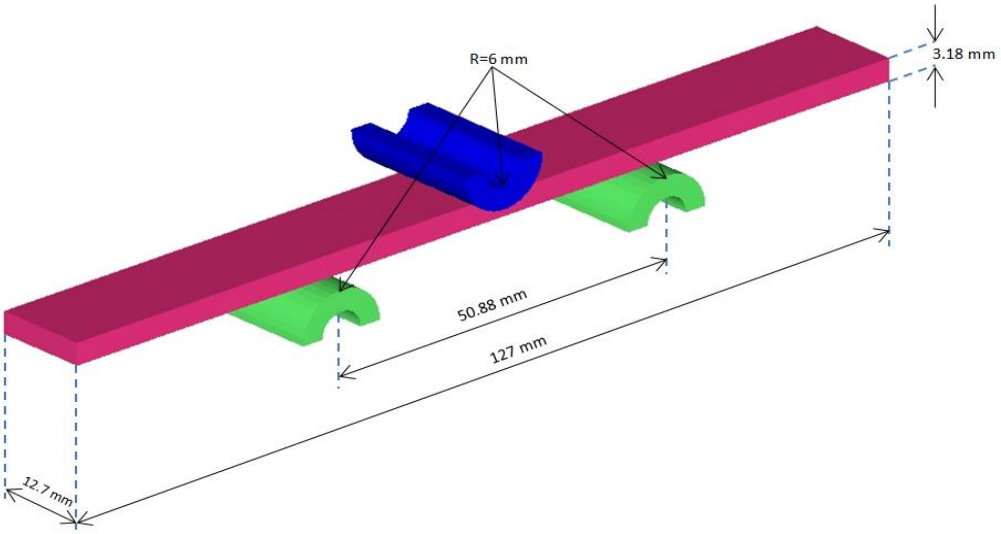

Fig 2.14. Geometrical specifications of 3-point bending ABS test specimen, supports and loading nose

The primary reason for conducting 3-point bending test on ABS is to validate the material model used in our numerical simulations. This is going to be explained more in the finite element part. The experimental setup of 3-point bending test is indicated in Fig 2.15.

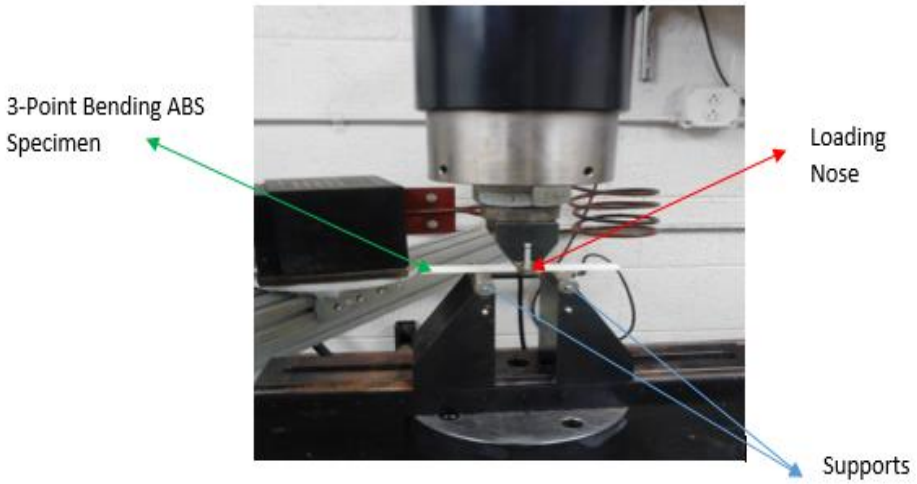

Fig 2.15. Experimental Setup for 3-Point Bending Test

2.5 Multiaxial Impact

The characterization of impact performance of ABS under various impact energies was accomplished carrying out impact experiments in the drop weight impact tower as shown in Fig 2.16. Three various impact velocities such as 4.429 m/s, 5.775 m/s and 6.2641 m/s were attained releasing a mass of 4 kg steel projectile with 1.3 inch hemispherical diameter nose from three different heights 1 m, 1.7 m and 2 m, respectively.

Fig 2.16. Drop weight impact tower

The ABS impact test specimens with the dimensions of 6-inch length and 4-inch width were prepared cutting off from 0.25-inch-thick plate. Clamped boundary conditions were applied to the ABS impact test specimen by means of a steel plate, that possess a rectangular inner hole with the dimension of 5-inch length and 3-inch width as illustrated in Fig 2.17.

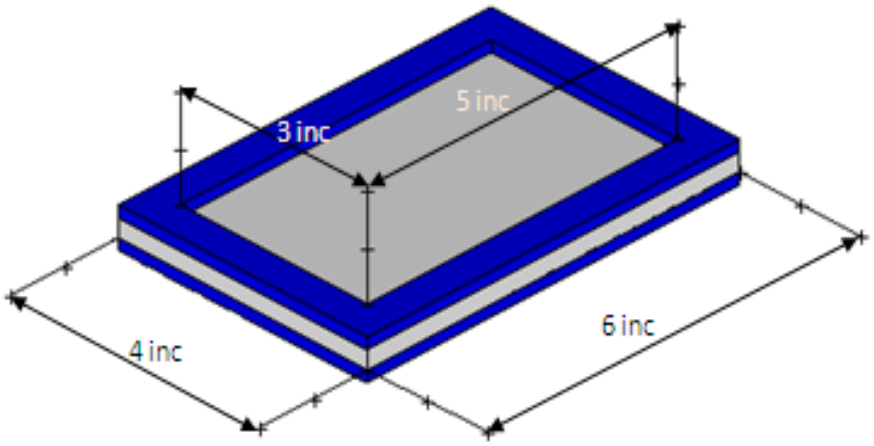

Fig 2.17. Geometrical specifications of steel fixture and the ABS impact test specimen

Throughout the impact tests, variation of acceleration with time was recorded for each impact velocity and impact force-time, displacement-time and kinetic energy change with time were extracted from the acceleration data.

Morover, the radial strains and strain rates were measured by means of three strain gages assembled on the back surfaces (non-impacted) of ABS impact specimens at points where 11 mm far away from impact point as illustrated in Fig 2.18. The main purpose of measuring radial strain rates was to make sure that resulted strain rates by impacts do not exceed the maximum strain rate used as an input in SAMP-1 material model for numerical simulations of impact tests.

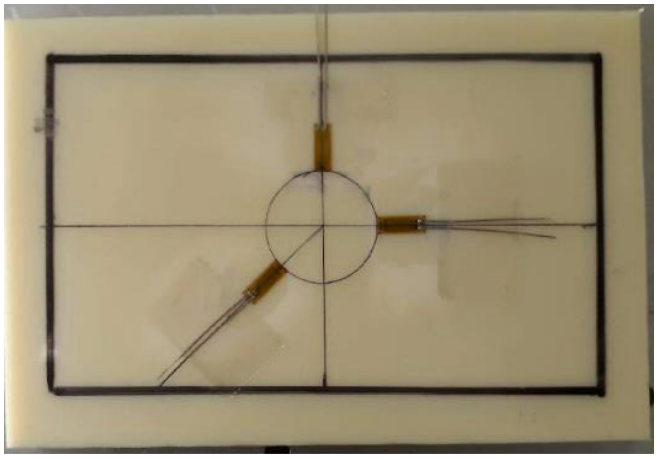

Fig 2.18. ABS impact specimen with strain gages (back surface)

CHAPTER 3 FINITE ELEMENT MODELLING

Numerical implementations of thermoplastic materials to predict their mechanical response subjected to different types of loading conditions such as tension, compression, shear and impact has been a great deal of interest for robust design[89-91]. Particularly, accurate estimation of their mechanical response under impact is becoming more significant because many thermoplastic materials are utilized as structural components that probably can be subjected to impact events[92, 93]. Nonetheless, developing a reliable numerical material model to predict the impact response of thermoplastics is currently under particular examination[94], due to their highly sophisticated material behaviors. As explained before, the material behaviors of thermoplastics are significantly influenced by strain rate, pressure and temperature. Furthermore, the most thermoplastics experience strain softening and strain hardening in their stress-strain states under tension and compression. A material model that is going to be used in the modeling of thermoplastics in any finite element code needs to possess the ability to capture all those material features of thermoplastics. Although many elastic-viscoplastic material models are commercially available in various finite element packages, the most of them are not well applicable to thermoplastics. Among the available finite element packages, we here intend to use the explicit solver of LS-DYNA. Regarding the usage of elastic-viscoplastic material models to describe the material behavior of thermoplastics in LS-DYNA, each available elastic-viscoplastic material model possesses some advantages and disadvantages compared to one another. Therefore, selecting a well applicable material model that enables to capture all relevant material behaviors is highly vital for accurate numerical prediction of the mechanical response of thermoplastics.

Among those elastic-viscoplastic material models tabulated above, semi-empricial material model for polymers (SAMP-1) that is recently developed by Kolling [96] can take all effects excepting temperature on material behavior of thermoplastics into account. This material model generates a convex yield surface through using the four distinct true pastic stress-true plastic strain curves as tabulated data that need to be obtained from four various mechanical tests such as uniaxial tension, uniaxial compression, shear and biaxial tension. Mat Samp-1 definetly requires at least one true plastic stress-true plastic strain curve as an input that must be obtained from either quasi static or dynamic uniaxial tension test.However the usage of only one true tensile plastic stress-platic strain curve in Mat Samp-1 does not reflect the exact material behavior of amorphous thermoplastics. Therefore, at least three distinct curves obtained from uniaxial tension, uniaxial compression and shear mechanical tests need to be introduced to the Mat Samp-1 as shown in Fig 3.1.

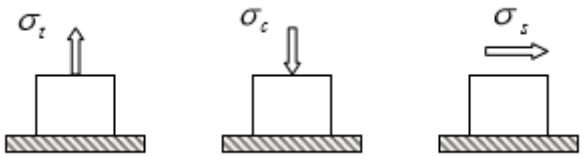

Fig 3.1. Essential mechanical tests for thermoplastics in Mat Samp-1 [96]

Numerical validation of this material model can be done through the finite element modelling of 3-point bending test as shown in Fig 3.2 because the dictated stress-state by 3-point bending reflects the actual material behavior of amorphous thermoplastics. To validate this material model, load-displacement curve needs to be obtained from 3-point bending test and experimental results should be compared to the numerical predictions.

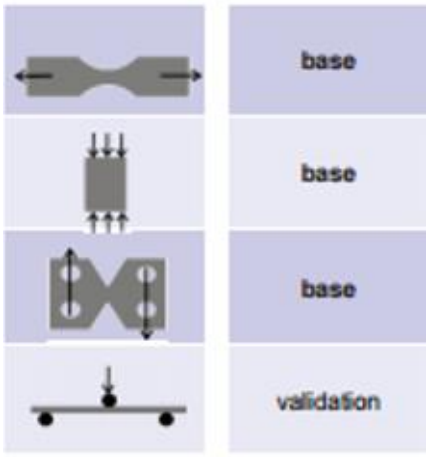

Fig 3.2. Compulsory mechanical tests for Mat Samp-1 and its validation[97]

If an amorphous thermoplastic is subjected to dynamic loads like impact, uniaxial tension tests need to be performed over a wide range of deformation rates as possible, depending on loading conditions, because Mat Samp-1 defines the strain rate dependency through multiple true tensile plastic stress-true plastic strain curves as a function of strain rates. Both uniaxial compression and shear tests can be conducted under quasi-static deformation state. The way how Mat Samp-1 generates yield surface based on provided experimental data obtained from different mechanical tests can be seen in Fig 3.3.

$$\left.\begin{matrix}\text{LCID\_C} = 0\\ \text{LCID\_S} = 0\\ \text{LCID\_B} = 0\end{matrix}\right\} \Rightarrow \begin{cases}\sigma_c = \sigma_t\\ \sigma_s = \dfrac{\sigma_t}{\sqrt{3}}\end{cases}$$

$$\left.\begin{matrix}\text{LCID\_C} = 0\\ \text{LCID\_S} \neq 0\\ \text{LCID\_B} = 0\end{matrix}\right\} \Rightarrow \sigma_c = \frac{\sqrt{3}\sigma_t\sigma_s}{2\sigma_t - \sqrt{3}\sigma_s}$$

$$\left.\begin{matrix}\text{LCID\_C} \neq 0\\ \text{LCID\_S} = 0\\ \text{LCID\_B} = 0\end{matrix}\right\} \Rightarrow \sigma_s = \frac{2\sigma_c\sigma_t}{\sqrt{3}(\sigma_t + \sigma_c)}$$

$$\left.\begin{matrix}\text{LCID\_C} = 0\\ \text{LCID\_S} = 0\\ \text{LCID\_B} \neq 0\end{matrix}\right\} \Rightarrow \begin{cases}\sigma_c = \dfrac{\sigma_t\sigma_b}{3\sigma_b - 2\sigma_t}\\ \sigma_s = \dfrac{\sigma_t\sigma_b}{\sqrt{3}(2\sigma_b - \sigma_t)}\end{cases}$$

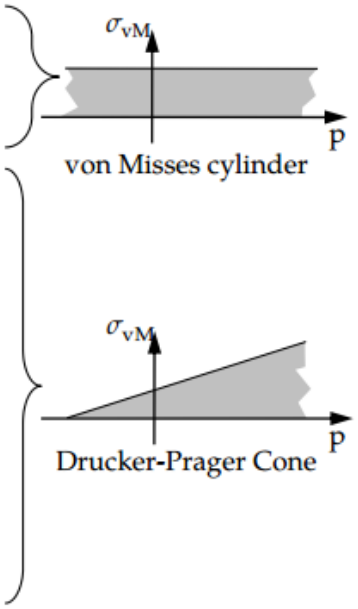

If there is more than one curve given as an input, excluded uniaxial tension;

$$\left.\begin{matrix}\text{LCID\_C} \neq 0\\ \text{LCID\_S} \neq 0\\ \text{LCID\_B} = 0\end{matrix}\right\} \Rightarrow \text{normal SAMP-1 behavior}$$

$$\left.\begin{matrix}\text{LCID\_C} \neq 0\\ \text{LCID\_S} = 0\\ \text{LCID\_B} \neq 0\end{matrix}\right\} \Rightarrow \sigma_s = \frac{1}{\sqrt{3}}\sqrt{\frac{3\sigma_b^2\sigma_c\sigma_t}{(2\sigma_b + \sigma_c)(2\sigma_b - \sigma_t)}}$$

$$\left.\begin{matrix}\text{LCID\_C} = 0\\ \text{LCID\_S} \neq 0\\ \text{LCID\_B} \neq 0\end{matrix}\right\} \Rightarrow \sigma_c = \frac{6\left(162\sigma_b^2\sigma_s^2 + \sigma_b\sigma_s^2\sigma_t\right)}{6\sigma_b\sigma_s^2 + 323\sigma_b^2\sigma_t + 3\sigma_s^2\sigma_t}$$

$$\left.\begin{matrix}\text{LCID\_C} \neq 0\\ \text{LCID\_S} \neq 0\\ \text{LCID\_B} \neq 0\end{matrix}\right\} \Rightarrow \text{oversepcified, least squares}$$

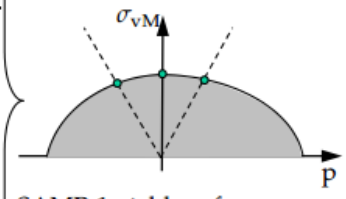

Figure 3.3. Yield surface formulation of Mat Samp-1 based on given stress-strain curves[98]

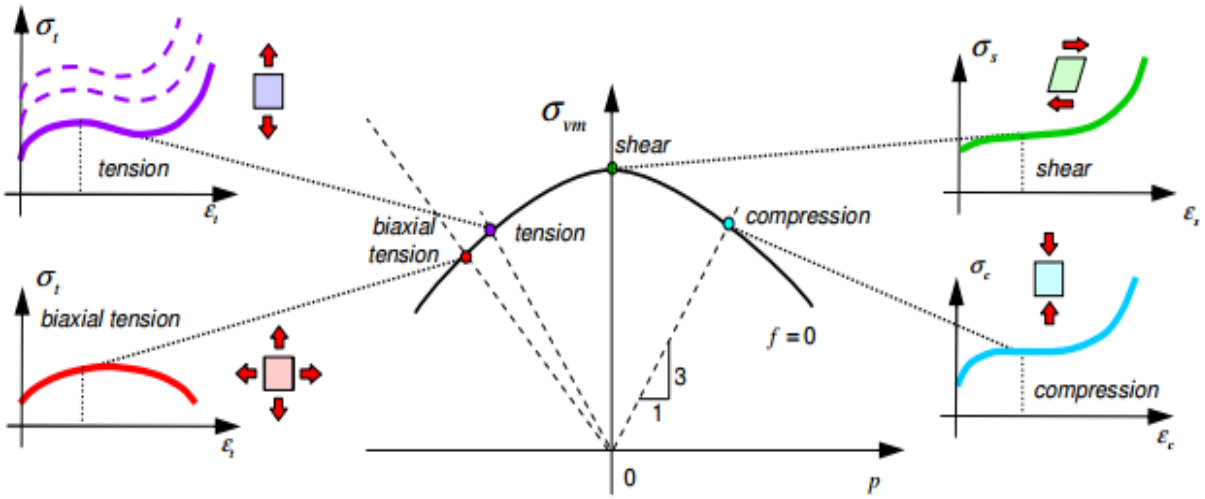

Fig 3.4. Yield surface of Mat Samp-1[99]

The quadratic yield surface defined by Mat Samp-1 for calculations is shown in Fig 3.4 and this quadratic yield surface can be formulated for isotropic thermoplastics as follows;

$$f = \sigma_{vm}^2 - A_0 - A_1 p - A_2 p^2 \leq 0 \tag{3.1}$$

where

$p = -\frac{\sigma_{xx}+\sigma_{yy}+\sigma_{zz}}{3}$, p is the first stress invariant (pressure)

and

$\sigma_{vm} = \sqrt{\frac{3}{2}[(\sigma_{xx}+p)^2 + (\sigma_{yy}+p)^2 + (\sigma_{zz}+p)^2 + 2\sigma_{xy}^2 + 2\sigma_{yz}^2 + 2\sigma_{xz}^2]}$, σ_{vm} is the first stress invariant (Von-Misses)

The unknown coefficients of A_0, A_1 and A_2 can be extracted from uniaxial tension,uniaxial compression and shear tests and they can be expressed in terms of test results as written below:

$$A_0 = \sigma_s^2 \tag{3.2}$$

$$\sigma_t^2 = 3\sigma_s^2 - A_1\frac{\sigma_t}{3} + A_2\frac{\sigma_t^2}{9} \tag{3.3}$$

$$\sigma_c^2 = 3\sigma_s^2 + A_1 \frac{\sigma_C}{3} + A_2 \frac{\sigma_c^2}{9} \tag{3.4}$$

A_1 and A_2 coefficients can readily be derived from eq (3.3) and eq (3.4) as;

$$A_1 = 9\sigma_s^2 \left(\frac{\sigma_C - \sigma_t}{\sigma_t \sigma_C}\right) \tag{3.5}$$

$$A_2 = 9\left(\frac{\sigma_t \sigma_C - 3\sigma_s^2}{\sigma_t \sigma_C}\right) \tag{3.6}$$

When the calculated coefficients as a function of mechanical test results are substituted into eq. (3.1) , we obtain quadratic yield surface for thermoplastics.

Similar to other elastic-viscoplastic material models, Mat Samp-1 has also some limitations as follows;

This material model uses an identical elastic modulus in tension and compression, as well as in all strain rates but this is not true for amorphous thermoplastics.

This material model considers the same strain rate effect on tensile and compressive yield stresses in all strain rates;however, some amorphous thermoplastics can be more sensitive to strain rate under compression.

This material model assumes that shape of the compressive and shear hardening curves obtained from quasi static tests are similar in all strain rates but generally the shape of compressive and shear hardening curves vary with strain rate.

3.1 Uniaxial Tension

The actual shape of uniaxial tension ABS test specimen was meshed with 6 elements through thickness and 24 elements along width as shown in Fig 3.5.

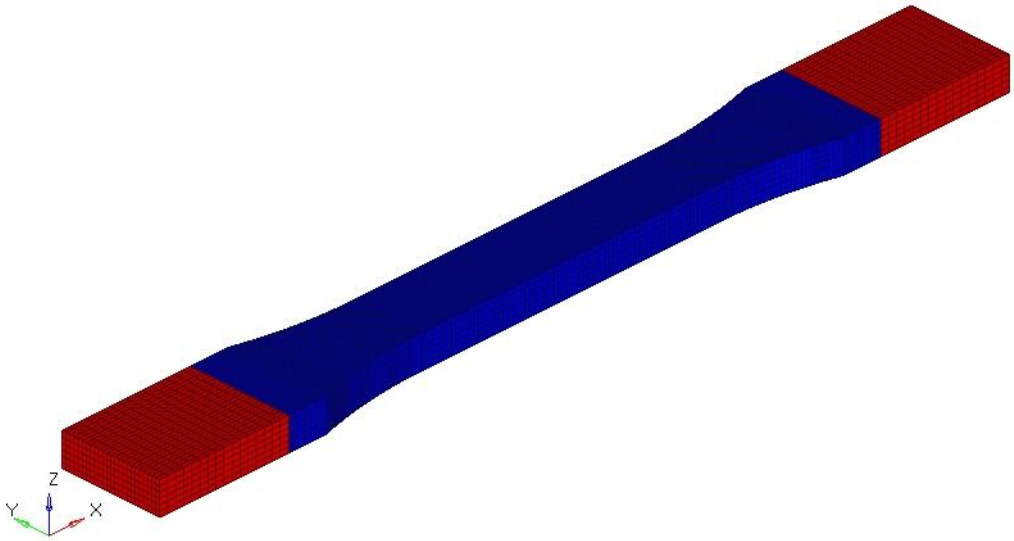

Fig 3.5. 3-Dimensional Finite Element Model of Uniaxial Tension Test

Both ends represented with red color in Fig 3.5 were considered as a rigid body. While fixed boundary conditions were applied to the one end, the actual test speeds with displacement control attained during uniaxial tension tests were directly imposed to another end. Solid element formulation with stiffness based hourglass control to eliminate unphysical hourglass energy modes was utilized in simulations.

In the numerical prediction of the mechanical response of ABS under uniaxial tension, five distinct true plastic stress-true plastic strain curves as a function of strain rate obtained from uniaxial tension tests were used as an input in SAMP-1. Additionally, plastic Poisson's ratio as a function of plastic strain measured by DIC during quasi static uniaxial tension test was introduced to SAMP-1. Depending on strain rates caused by the applied actual test speeds, the mechanical response of ABS under uniaxial tension was computed by SAMP-1.

3.2 Uniaxial Compression

The finite element modelling of uniaxial compression tests was prepared based on our actual test setup as depicted in Fig 3.6. Both lower and upper compression platens were modelled as a rigid body. The uniaxial compression ABS test specimen was strained up 78% for each

deformation rate by means of applying displacement control rigid body motion to upper platen. The lower platen was fixed.

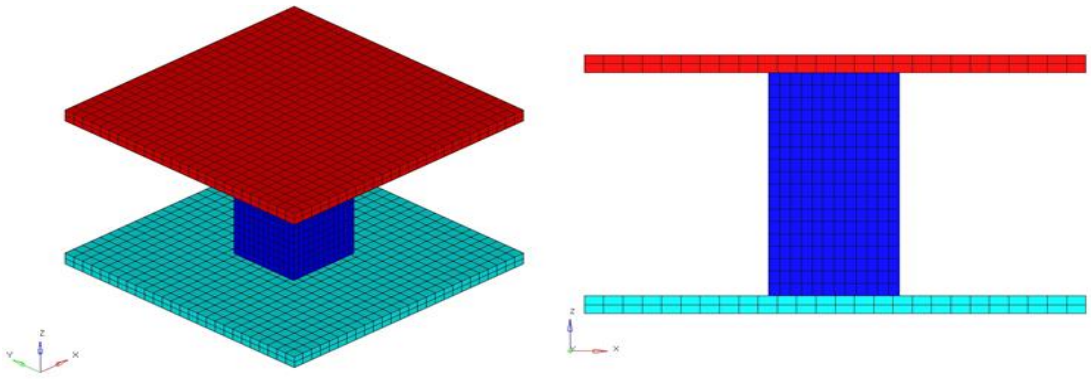

(a) (b)

Fig 3.6. 3-Dimensional Finite Element Model of Uniaxial Compression Test, (a) Isometric view, (b) Front view

The attained ultimate strain about 78% in simulations causes an excessive large plastic deformation and extensive distortion in elements that adversely affects the accuracy of numerical predictions. To eliminate numerical instabilities in simulations of uniaxial compression tests, Automatic general contact type with interior option was specified between lower platen and ABS, as well as the upper platen. This interior option assists to reduce numerical instabilities caused by extensively distorted elements during simulations. There was no friction coefficient defined between contact surfaces.

3.3 Three-Point Bending

The finite element modeling of the 3-point bending test is shown in Fig 3.7. Due to symmetry, the half of it was modelled and symmetry boundary conditions were assigned to nodes on elements along x-y symmetry axis. The grid geometry of 3-point bending ABS test specimen was meshed with 7 elements through thickness and 7 elements along width. The regions of ABS

that are in contact with loading nose and supports were meshed finer to increase the contact accuracy, as well as the overall numerical prediction accuracy. Both loading nose and supports were modelled as a rigid body. While the supports were completely fixed, the loading nose was only allowed to move along bending direction (-y direction) and the displacement control rigid body motion was successfully assigned to the loading nose. The bending deformation rates used in actual 3-point bending tests was directly applied to the loading nose.

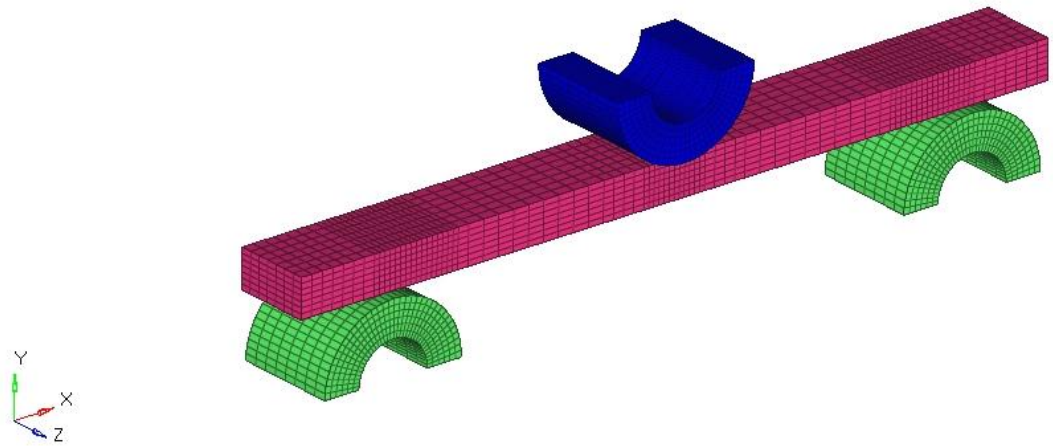

Fig 3.7. 3-Dimensional Finite Element Model of 3-Point Bending Test

Automatic surface-to-surface contact algortihm was defined between contact surfaces and a bending force as afunction of displacement were obtained from the defined contact surface on the loading nose. The predicted bending forces were plotted against displacement for each deformation rate. There was no friction defined between contact surfaces. To decrease time step and achieve quasi static conditions, mass scaling of 1e-7 was activated in simulations.

In the numerical simulations of 3-point bending tests, the strain rate dependent material behavior of ABS was introduced to mat SAMP-1 by means of tensile true stress-true strain curves as a function of strain rate. The material behavior of ABS is not identical in tension and in compression, as well as shear. For this reason, compressive true plastic stress-plastic strain curve

measured from quasi staic uniaxial compression test was also used as an input, shear as well. After each simulation, effective strain rate caused by the assigned actual test speeds to the loading nose was numerically obtained from elements at mid-span in the lower surface to find out whether ot not the produced strain rates are in the range of strain rates that we used as an input in the material model. The numerically obtained effective strain rates are documented in the finite element result section after each simulation. Also, the same simulations were run with the Von-Misses plasticy to figure out the influence of different behavior between tension and compression on ovearall mechanical response of ABS. To attain Von-Misses plasticty in Mat Samp-1, we simply removed the compression and shear test data. For each deformation rate, the load-displacement curve predicted by Mat Samp-1 was compared to the load-displacement curve obtained from Von-Misses plasticty.

3.4 Multiaxial Impact

The finite element modeling of multiaxial impact test is shown in Fig 3.8. The projectile was modelled as a rigid body and elastic steel material properties were assigned to the projectile. Only the hemispherical section (nose) of the entire projectile was meshed and to achieve the real mass of projectile, an additional mass was added to the geometrical center of projectile at the top. All degrees of freedom were fixed with the exception of impact direction for the projectile. The actual three different initial velocities were dictated to the projectile.

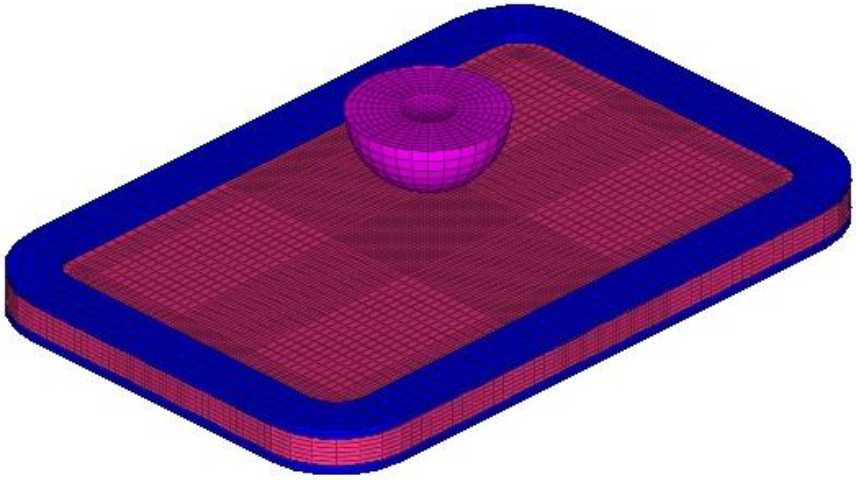

Fig 3.8. Finite Element Modelling of Impact Test

The clamped boundary conditions was applied to the finite element model of ABS impact test specimen through the upper and lower fixtures modelled as a rigid body like the projectile. Two fixtures were fixed with rigid body boundary conditions in rigid body material card in LS-DYNA. Because of the very small inner radious at the four corners of the fixtures, the outer sharp corners of ABS and fixtures were smoothed for simplicity and to prevent numerical instabilities but the inner dimension of fixtures were remained the same.

In the same fashion of finite element modelling of 3-point bending, the grid geometry of ABS specimen was divided into smaller elements where it is in direct contact with the profectile and the fixtures as illustrated in Fig 3.4.1. While automatic surface to surface contact type was defined between the projectile and ABS impact specimen, automatic general contact algorith was utilized between ABS impact specimen and fixtures. No friction coefficient was assigned during simulations.

The similar experimental data used in the simulations of 3-point bending tests were used as an input in Mat SAMP-1 to describe the material behavior of ABS material during impact simulations. The experimental data used in the determination of material behavior of ABS under

impact generally cover the actual material features of ABS such as strain rate dependency and pressure sensitivity. We additionally run the same impact simulations without the consideration of strain rate effect on overall impact performance of ABS. The predicted results with strain rate effect and without strain rate effcet were compared to each other in terms of impact force,displacement and kinetic energy variation during impact. Also, those numerical findings were compared to experimental impact results.

CHAPTER 4 EXPERIMENTAL RESULTS

4.1 Uniaxial Tension

The strain rate response of ABS was achieved by the implementations of uniaxial tension tests under five different strain rates ranging from low to moderate and true stressess were plotted against corresponded true strains for each strain rate and documented. As stated before, ABS consists of randomly dispersed rubber particles in its structure and during deformation voids may be formed near rubber particles caused by crazes that are the main reason for damage in rubber toughnened amorphous thermoplastics, like ABS. Voids formation results in a volume change in structure under deformation and true stresses can be considerably affected by this volume change that can only be detected by the use of software based optical methods such as digital image correlation during tension tests because extensometer only records average elongations along gage length. We obtained uniaxial tension test data for all strain rates by means of the extensometer; however, digitial image correlation optical method was also utilized in monitoring true longitudinal and true transverse strain variations in uniaxial tension tests where the first two lowest strain rates ($1x10^{-4}$ s^{-1} and $1x10^{-3}$ s^{-1}) were attained. The aim of using DIC for only those strain rates is to compare DIC data to extensometer data, if there is no considerable effect observed on true stresess and their corresponding strains, we can depend on extensometer data[101] for other moderate strain rates from 0.02 s^{-1} to 0.2 s^{-1}.

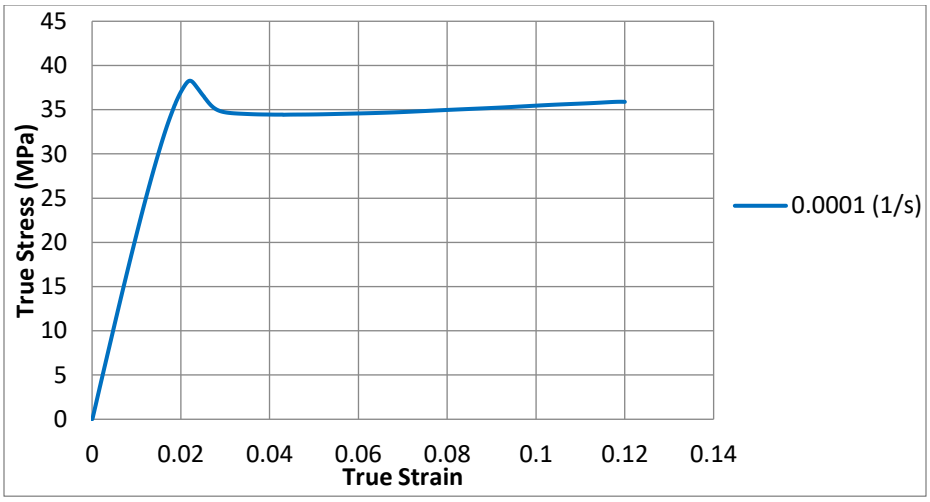

(a)

(b)

Fig 4.1. (a) Tensile true stress-true strain curve of ABS at strain rate of $1x10^{-4}$ s^{-1} (b) Ruptured specimen

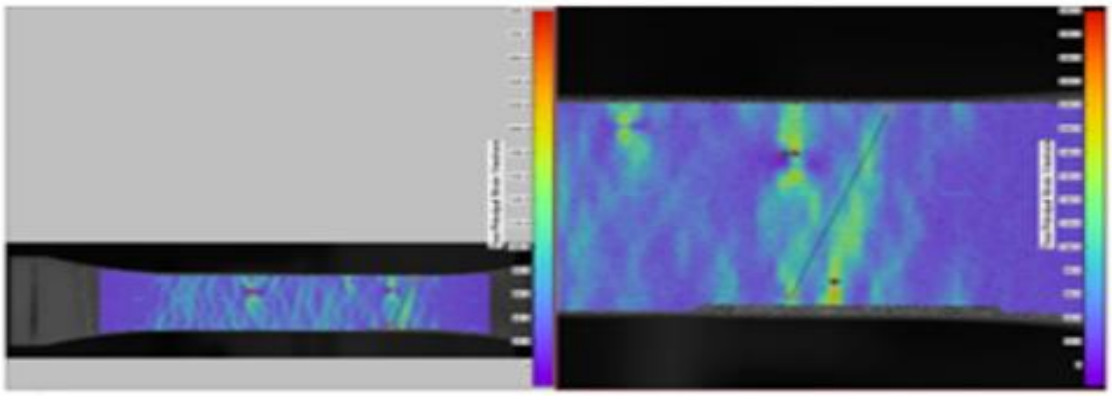

Fig 4.2. DIC tensile true stress-true strain under $1x10^{-4}$ s^{-1}

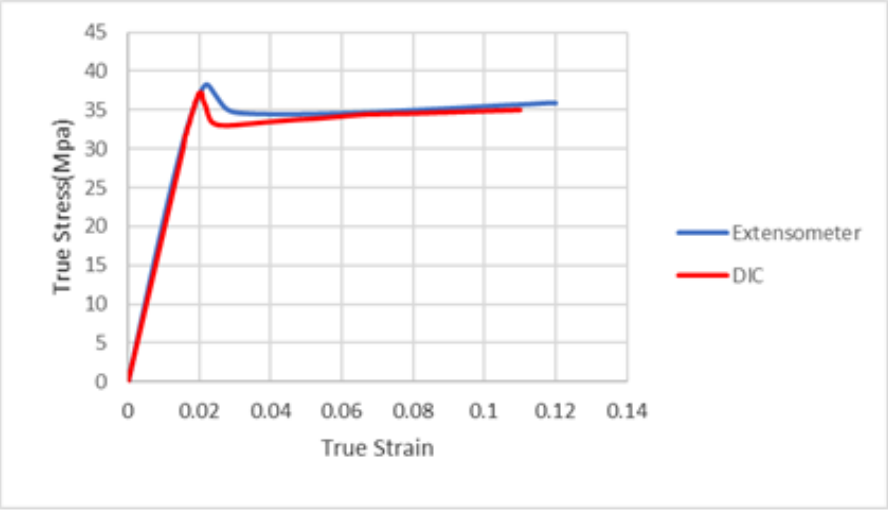

Fig 4.3. DIC result compared to extensometer result under $1x10^{-4}$ s^{-1}

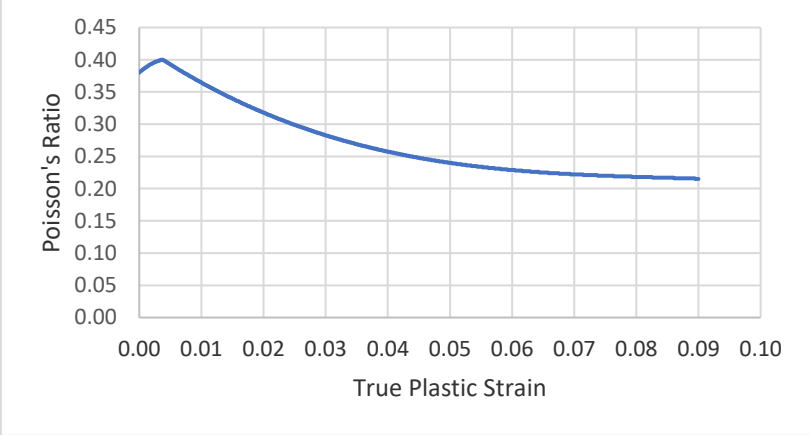

Fig 4.4. Plastic Poisson's ratio variation with true plastic strain under $1x10^{-4}$ s^{-1}

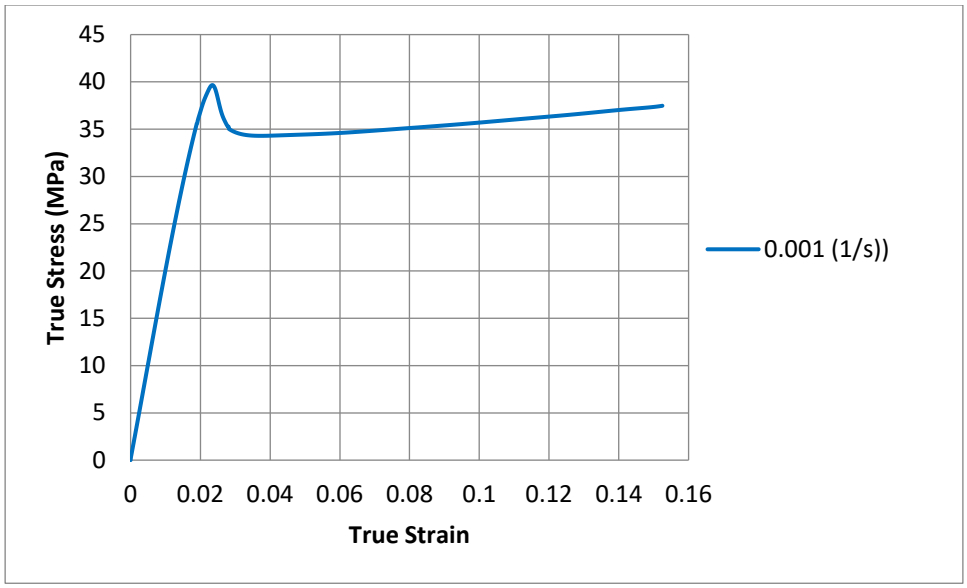

(a)

(b)

Fig 4.5. (a) Tensile true stress-true strain curve of ABS at strain rate of $1x10^{-3}$ s^{-1} (b) Ruptured specimen

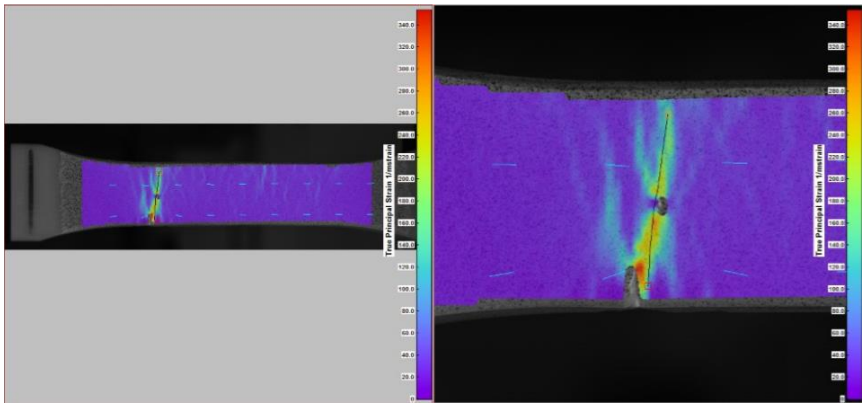

Fig 4.6. DIC tensile true stress-true strain under $1x10^{-3}$ s^{-1}

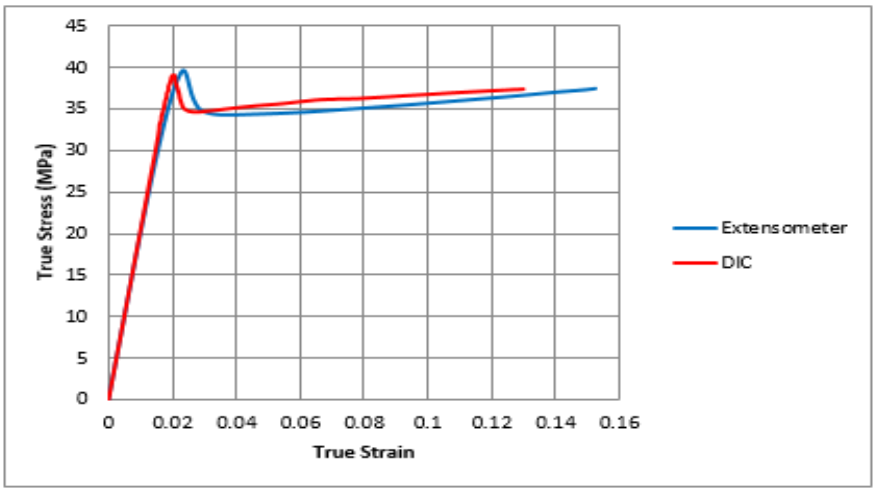

Fig 4.7. DIC result compared to extensometer result under $1x10^{-3}$ s^{-1}

True stress-true strain curves obtained from DIC were compared to extensometer data for the strain rates of $1x10^{-4}$ s^{-1} and $1x10^{-3}$ s^{-1} as shown in Fig 4.3 and Fig 4.7, respectively. Since both the extensometer and DIC provided similar results in terms of yield stresses and rupture strains for ABS, we were only dependent on extensometer data for other strain rates. It needs to be emphasized that we assumed that transverse strain equals strain through thickness based on assumption of transverse isotropy in the true stress calculations from DIC data. The DIC data was taken from the section of ABS where a necking started and was eventually ruptured. We drew a line on the shear band along width and we took the average of transverse and longitudinal true strains on that line for both strain rates as seen in Fig 4.2 and Fig 4.6. Plastic Poisson's ratio distribution with plastic strain was calculated from the transverse and longitudinal strains obtained from DIC under the strain rate of $1x10^{-4}$ and a variation of plastic Poisson's ratio were plotted against true plastic strains shown in Fig 4.4. The similar feature of plastic poison's ratio distribution for ABS was also found in [20].

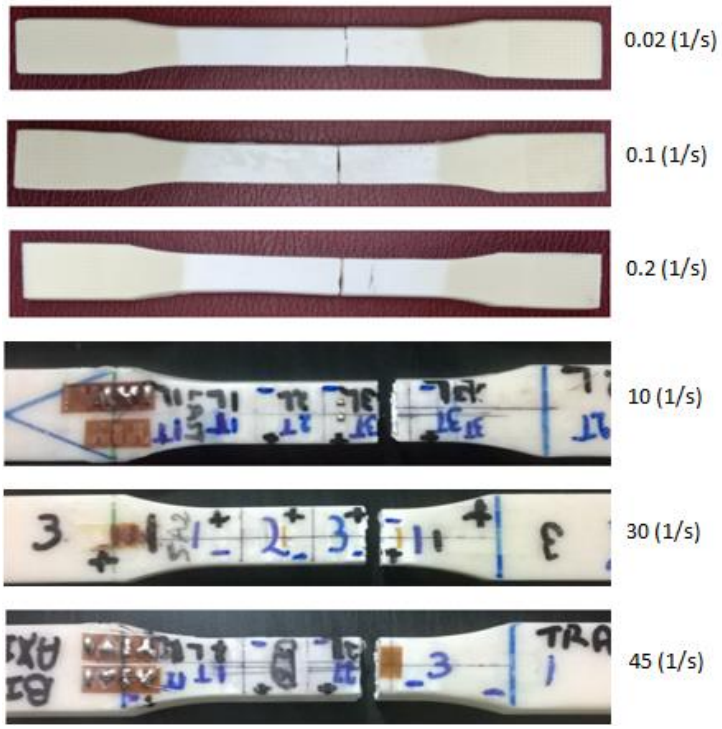

Fig 4.8. Ruptured tension specimens under various strain rates

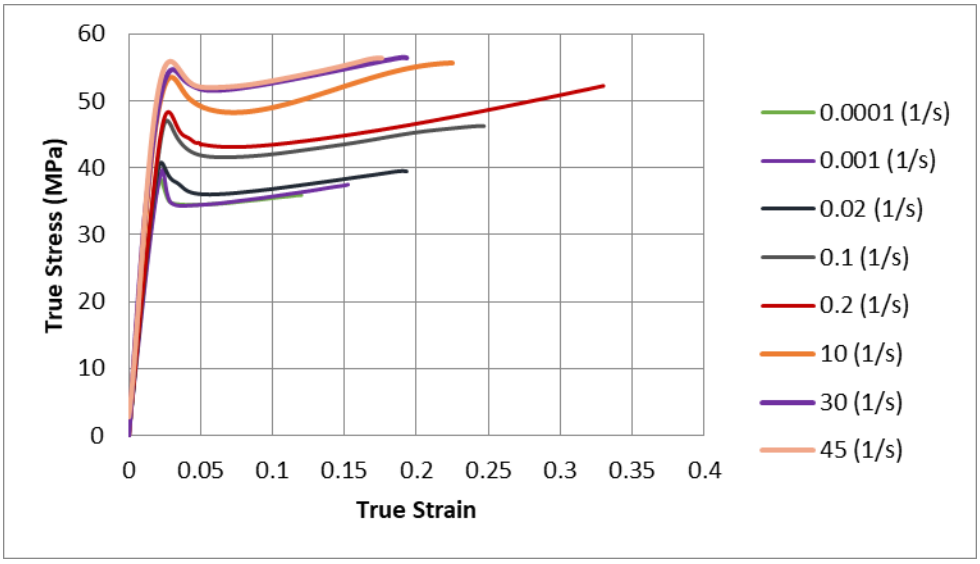

Fig 4.9. The comparisons of true stress-strain curves for ABS under uniaxial tension at different strain rate

Table 4.1. Upper, Lower and Intrinsic Yield Drop Stresses of ABS under uniaxial tension at various strain rates

Log Strain Rate (s^{-1})	σ_{upper}(MPa)	σ_{Lower}(MPa)	Intrinsic Yield Drop(MPa)
-4	38.273	34.7	3.573
-3	39.658	34.5	5.158
-1.69897	40.76	36	4.76
-1	47.046	41.6	5.446
-0.69897	48.322	43.1	5.222
1	53.5	49.2	4.3
1.477121	54.6	51.8	2.8
1.653213	55.9	52.1	3.8

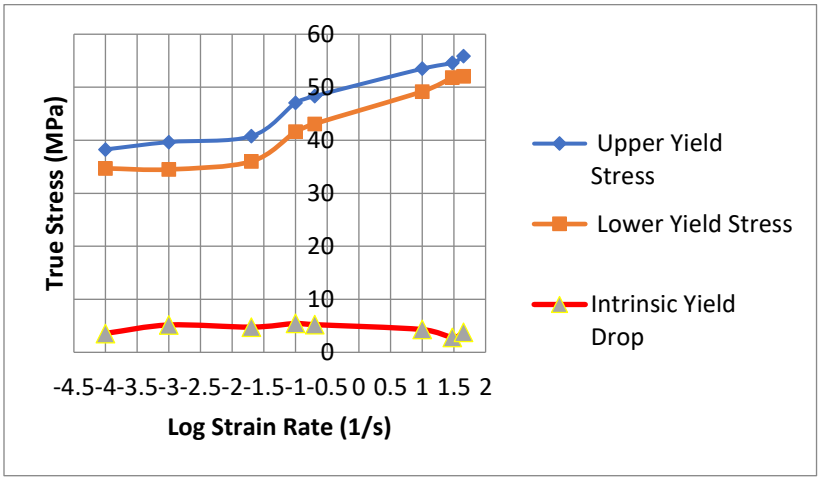

Fig 4.10. The comparison of upper, lower and intrinsic yield drop stresses of ABS under uniaxial tension at various strain rates

Table 4.2. Tensile Elastic Modulus of ABS under Various Strain Rates

Strain Rate (1/s)	True Tensile Elastic Modulus (MPa)
0.0001	1826
0.001	1826.58
0.02	1938
0.1	2026
0.2	2070
10	2485
30	2512
45	2547

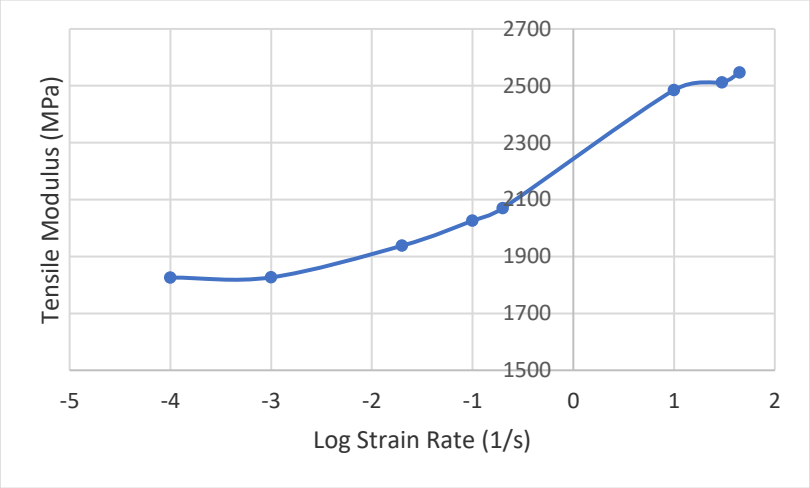

Fig 4.11. Tensile modulus of ABS at various strain rates

The following conclusions can be made from the conducted uniaxial tension tests on ABS under various strain rates ranging from low (0.0001 s^{-1}) to moderate (45 $s^{-1)}$.

- From Fig 4.1, Fig 4.5 and Fig 4.5, it can be concluded that the fracture behavior of ABS is brittle; therefore, necking areas for all strain rates are barely distinguishable. Additionally, after uniaxial tension tests, the natural color of ABS throughout the gage length turned into a light white color under all strain rates indicating that micro voids formation took place due to the movements of chain macromolecules to each other during deformation.
- From Fig 4.9 and Fig 4.10, it can be deduced that intrinsic yield drop that is followed by strain hardening occurs within a very small range of strains showing that necking is instantly stabilized. While the maximum intrinsic yield drop was found as 5.446 MPa under the strain rate of 0.1 s^{-1}, the minimum one was observed as 2.8 MPa under the strain rate of 30 s^{-1}.
- From Table 4.2, it can be pointed out that the quasi-static tensile elastic modulus of ABS can be given as about 1826 MPa. Furthermore, the elastic modulus of ABS

for the maximum attained strain rate of 45 s^{-1} during tension experiments was calculated as 2547 MPa.

4.2 Uniaxial Compression

Compressive strain rate dependent material behavior of ABS was investigated through conducted uniaxial compression tests at five distinct strain rates varying from $2x10^{-4}$ s^{-1} to $4x10^{-1}$ s^{-1}. The measured compressive true stress-true strain curves of ABS were reported for each compressive strain rate and favorably compared to one another to examine the strain rate influence on the material behavior of ABS.

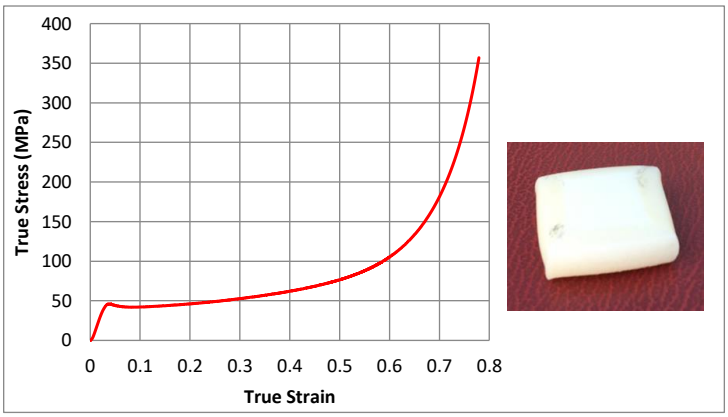

Fig 4.12. Compressive true stress-true strain curve of ABS at strain rate of $2x10^{-4}$ s^{-1}

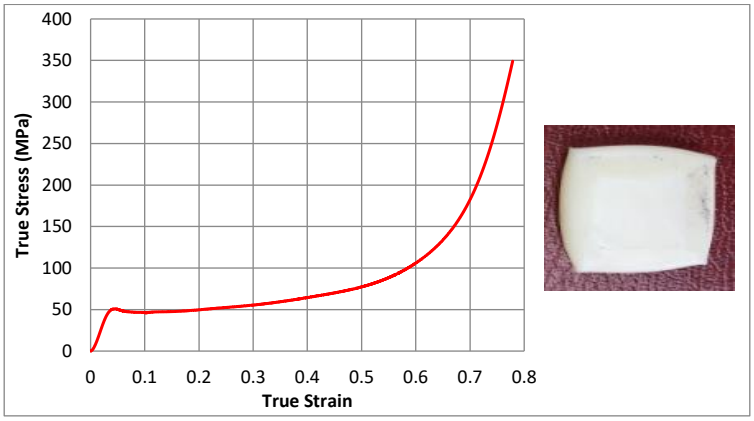

Fig 4.13. Compressive true stress-true strain curve of ABS at strain rate of $2x10^{-3}$ s^{-1}

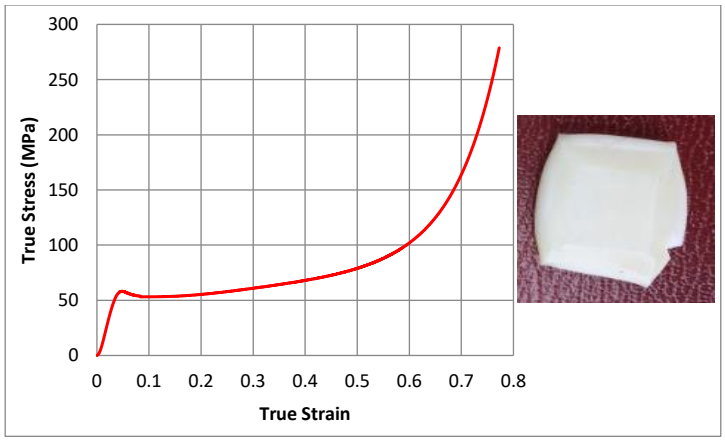

Fig 4.14. Compressive true stress-true strain curve of ABS at strain rate of $4x10^{-2}$ s^{-1}

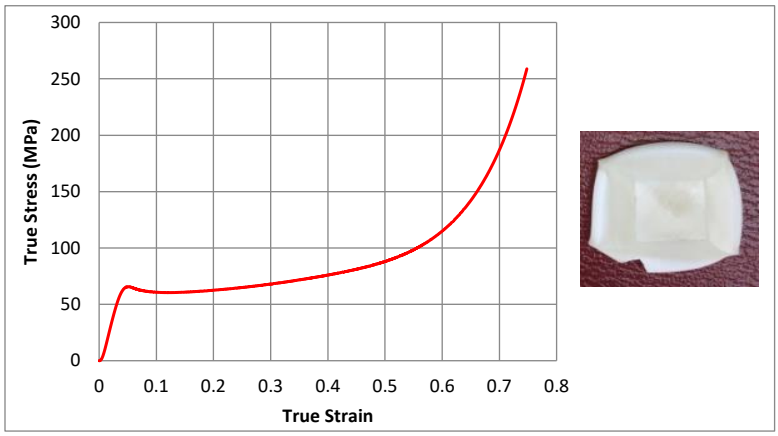

Fig 4.15. Compressive true stress-true strain curve of ABS at strain rate of $2x10^{-1}$ s^{-1}

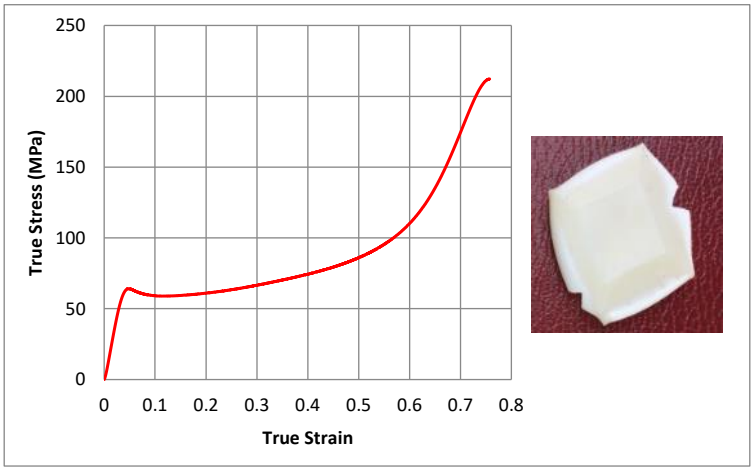

Fig 4.16. Compressive true stress-true strain curve of ABS at strain rate of $4x10^{-1}$ s^{-1}

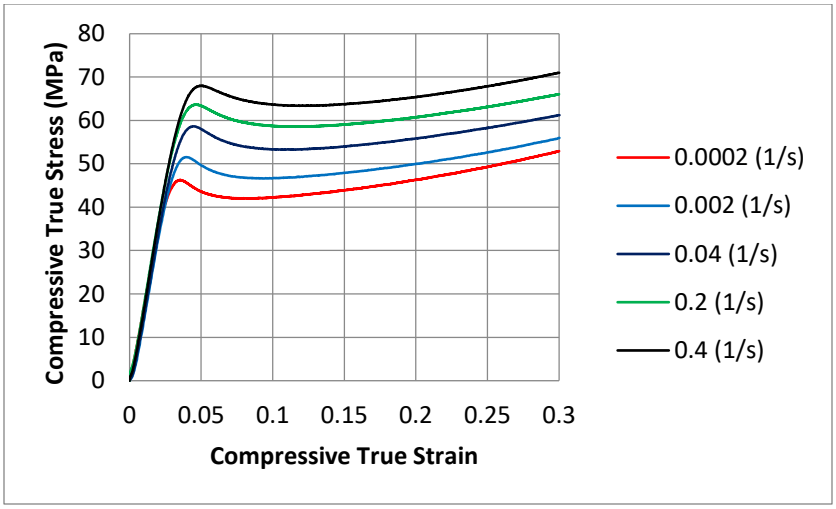

Fig 4.17. Comparisons of compressive true stress-true strain curves of ABS at various strain rates

Table 4.3. Compressive Upper-Yield Stresses of ABS with Strain Rate

Strain Rate (1/s)	**Compressive Post-Yield Point (MPa)**
0.0002	46.1
0.002	50.83
0.04	58.175
0.2	63.56
0.4	65.63

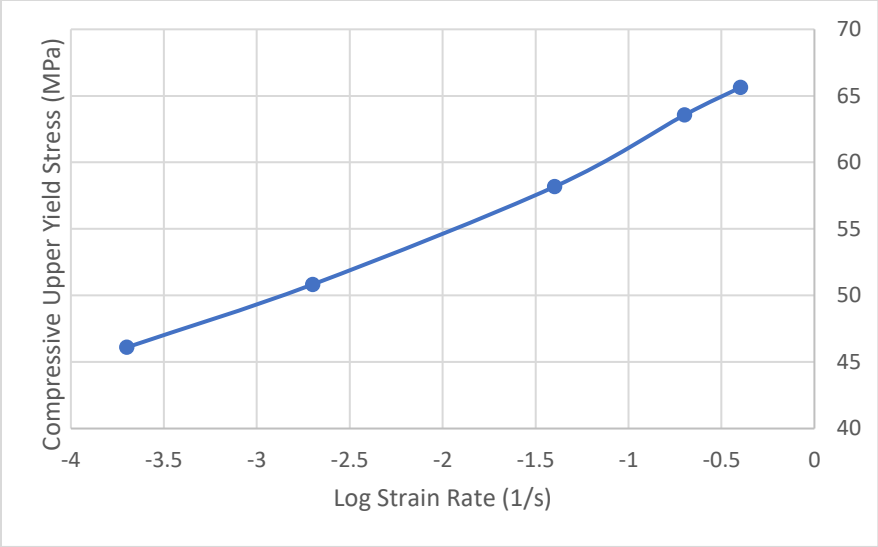

Fig 4.18. Compressive upper yield stresses of ABS with strain rate.

Table 4.4. Compressive Elastic Modulus of ABS with Strain Rate

Strain Rate (1/s)	**True Compressive Elastic Modulus (MPa)**
0.0002	1878
0.002	2105.5
0.04	2186
0.2	2209
0.4	2255

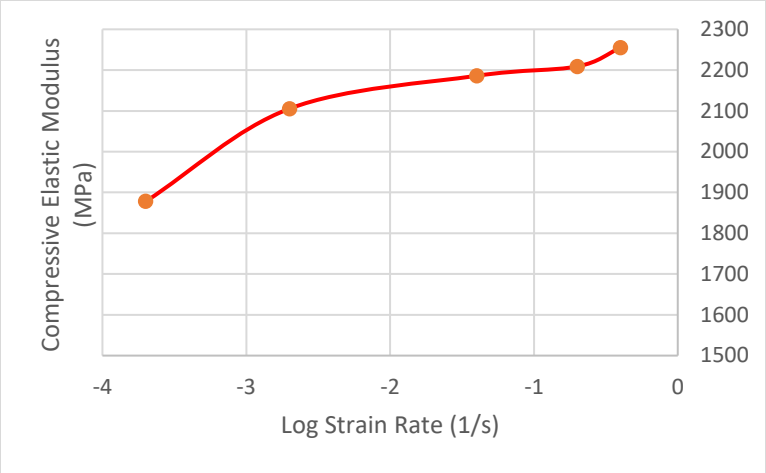

Fig 4.19. Compressive elastic modulus of ABS with strain rate

The strain rate response of ABS under uniaxial compression was successfully identified for different strain rates and documented above. A helpful way to comprehend material behavior of ABS under tension and compression is to compare tensile true stress-strain curves with compressive true stress-strain curves for identical strain rates. Thus, they are compared to each other for two same strain rates in the following figures.

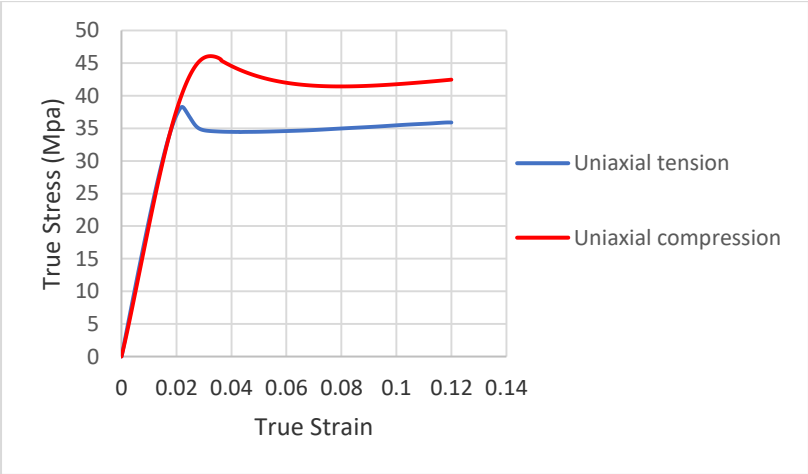

Fig 4.20. Comparisons of true stress-true strain curves under the same strain rate (quasi – static)

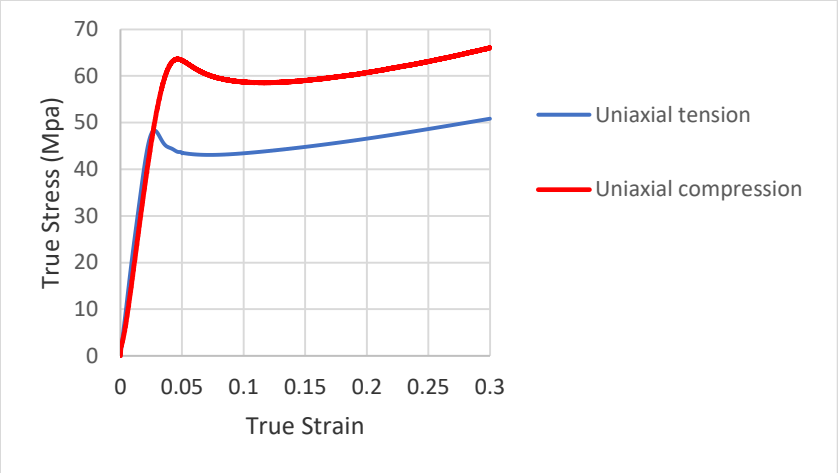

Fig 4.21. Comparisons of true stress-true strain curves under the same strain rate of $2x10^{-1}$ s^{-1}

Table 4.5. Comparison of tensile yield stresses and tensile elastic modulus of ABS with compressive yield stress and compressive elastic modulus under the same strain rates

	Yield Stress(MPa)		**Elastic Modulus(MPa)**			
Strain Rate (1/s)	Uniaxial Tension	Uniaxial Compression	Uniaxial Tension	Uniaxial Compression	σ_C/σ_T	E_C/E_T
Quasi Static	38.273	46.1	1826	1878	1.204	1.028
0.2	48.322	63.56	2070	2209	1.315	1.067

The following conclusions may be summarized from the outcomes of uniaxial compression tests, as well as, the comparisons of uniaxial tension curves with uniaxial compression curves for the same strain rates.

- In contrast to tension tests, there is no color change observed in compressed ABS specimens for any attained strain rate explaining that micro voids formation does not take place in ABS subjected to compression.

- From Fig 4.20 and Fig 4.21, it can be stated that the features of the tensile true stress-strain curves are generally identical with the compressive curves but intrinsic yield drop is more drastic under tension compared to compression.
- Compressive yield stress and compressive elastic modulus were found always larger than the tensile yield stress and tensile elastic modulus. While the ratio of σ_C/σ_T and E_C/E_T were calculated as 1.204 and 1.028 for the strain rate of 0.0001 s^{-1} (quasi-static), respectively, the same ratios were reported as 1.315 and 1.067 for the strain rate of 0.2 $^{s-1}$ as documented in Table 4.5. Which indicate that the material behavior of ABS is more sensitive to strain rate under compression than under tension.
- Why there are more drastic intrinsic yield drop, less yield stress and elastic modulus under tension observed in ABS can be explained from the movements of chain macromolecules to one another. For instance, while chain macromolecules change their initial positions under tension, micro voids take place near rubber particles and the direct indication of micro voids formation is a color change (light white color) in ABS that was never observed under compression. Micro voids cause a reduction in the stiffness of ABS that leads to a reduction in the yield stresses and elastic modulus of ABS subjected to tension.

4.3 Shear

In order to examine the strain rate dependent shear response of ABS, shear tests were carried out by the use of Modified Wyoming Iosipescu shear test method (ASTM D5379) at five distinct shear strain rates from low to moderate. In general, since plastics or amorphous thermoplastics do not experience any shear fracture, shear failure is not considered for robust design. The primary problem to the specification of shear behavior of amorphous thermoplastics

is the existence of several different shear test methods that utilize different shear test fixtures yielding different results.

Similar to the uniaxial tension tests, we measured shear strains by the use of digital image correlation method for the first lowest shear strain rates ($4.54x10^{-4}$ and $4.54x10^{-3}$) to make sure our shear strain calculations based on grip separation. If there is no significant discrepancy in shear strains between DIC and our calculations from grip separation, we will be dependent on grip separation for other shear strain rates.

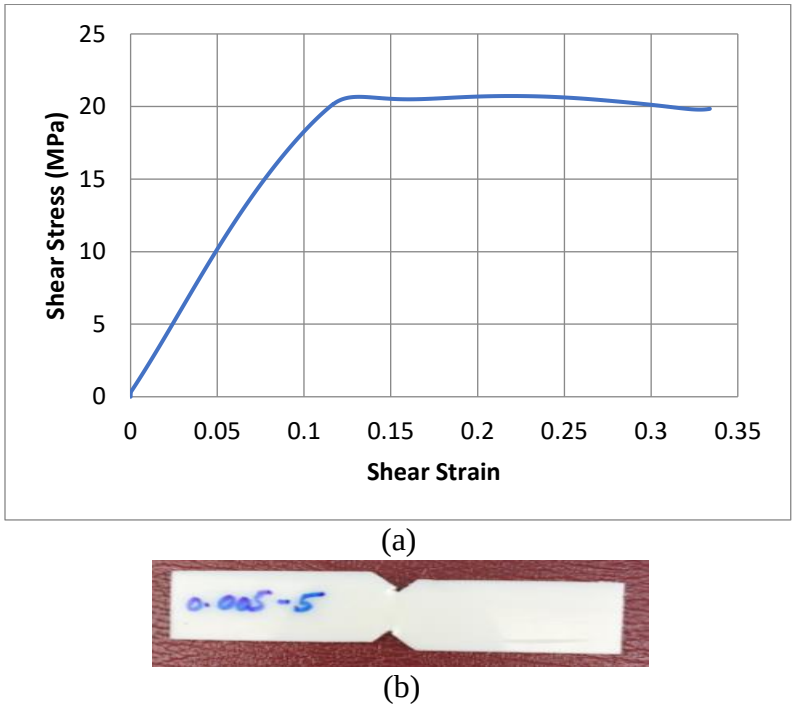

Fig 4.22. (a) Shear stress-shear strain curve of ABS at strain rate of $4.54x10^{-4}$ s^{-1}, (b) deformed specimen.

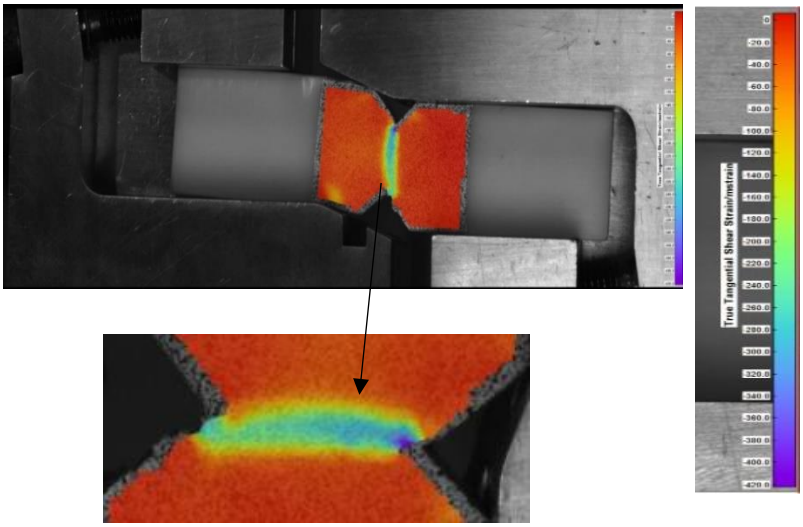

Fig 4.23. DIC true tangential shear strain of ABS at strain rate of 4.54×10^{-4} s^{-1}

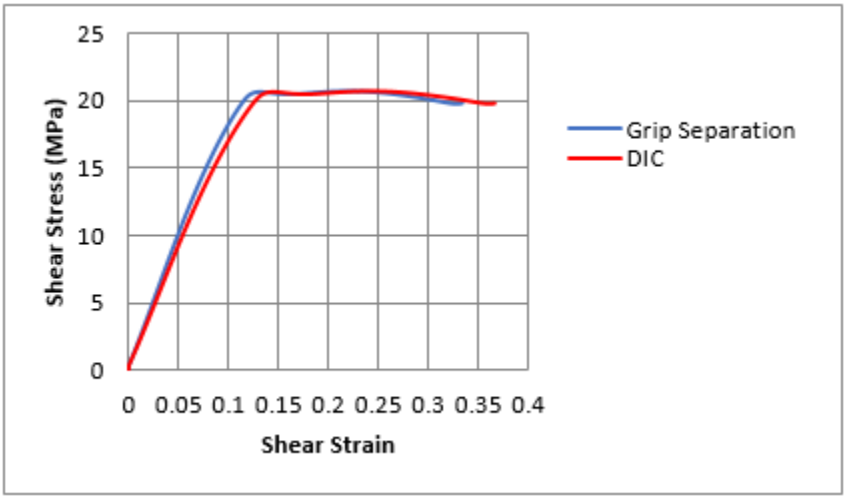

Fig 4.24. Grip separation vs. DIC for shear strain rate of 4.54×10^{-4} s^{-1}

There is a very good consistency observed between the calculated shear strains and the monitored ones from DIC for this shear strain rate of 4.54×10^{-4} s^{-1}. DIC gives ultimate shear strain a little larger.

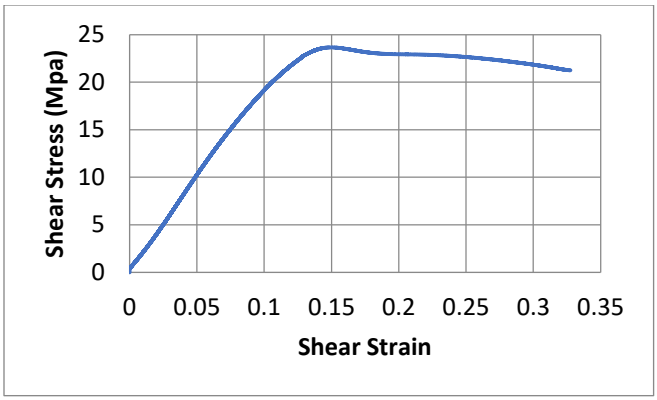

(a)

(b)

Fig 4.25. (a) Shear stress-shear strain curve of ABS at strain rate of $4.54x10^{-3}$ s^{-1}, (b) deformed specimen

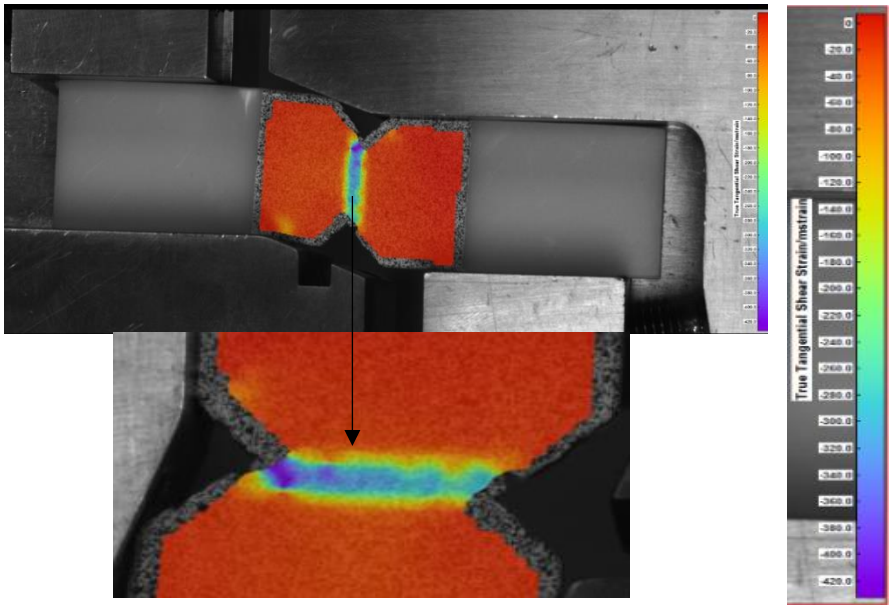

Fig 4.26. DIC true tangential shear strain of ABS at strain rate of $4.54x10^{-3}$ s^{-1}

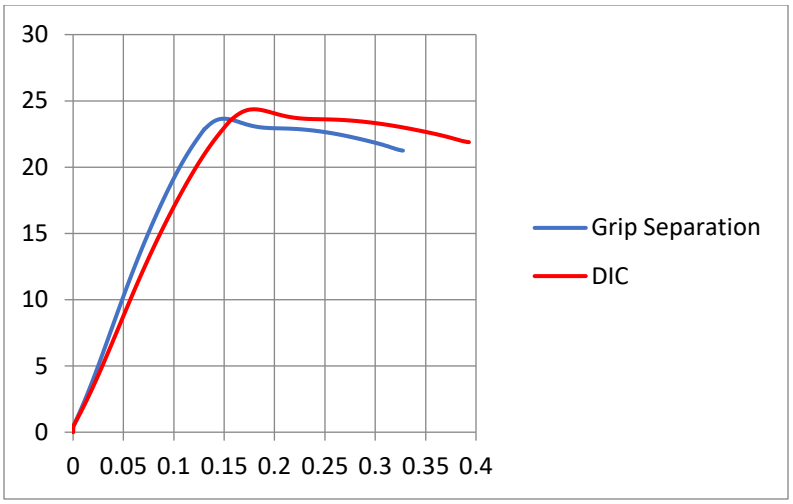

Fig 4.27. Grip separation vs. DIC for shear strain rate of 4.54×10^{-3} s^{-1}

For this strain rate of 4.54×10^{-3} $s^{-1,}$ the relationship between extracted shear strains from DIC and the calculated shear strains depending on machine displacement was considered as acceptable and we were dependent on grip separation for shear strain calculations in other shear strain rates.

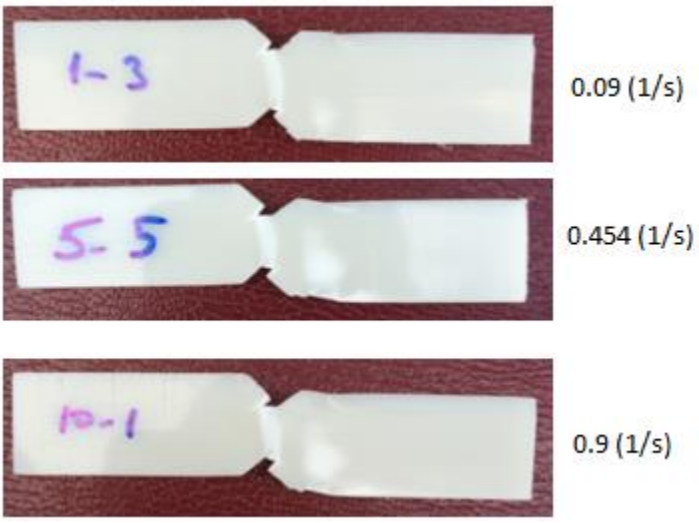

Fig 4.28. Deformed ABS test specimens under shear for different strain rates

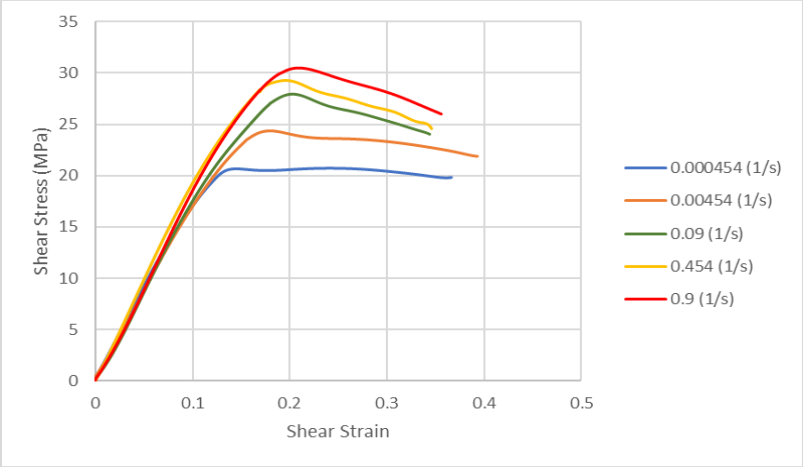

Fig 4.29. Comparisons of shear stress-strain curves of ABS under various strain rates

Table 4.6. Shear yield stresses of ABS with shear strain rate

Shear Strain Rate (1/s)	**Shear Yield Stress (MPa)**
0.000454	15.002
0.00454	16.795
0.09	17.837
0.454	20.05
0.9	24.019

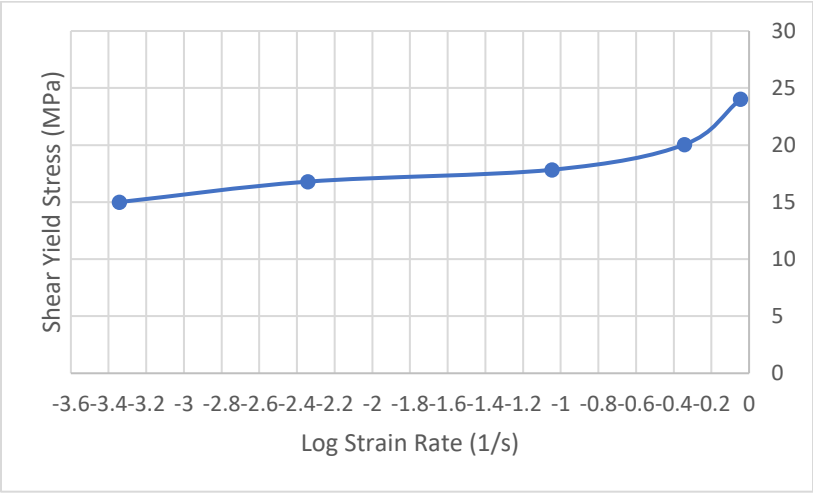

Fig 4.30. Shear yield stress of ABS for various strain rates

From the obtained results of shear tests, conclusions can be summarized as;

As expectedly, a shear fracture was not observed in ABS. An increased shear strain rate leads to an increase in shear yield stresses of ABS as shown in Fig 4.29 and tabulated in Table 4.6. Like yield stresses in uniaxial tension and uniaxial compression, shear yield stresses of ABS increases hyperbolically with shear strain rate as seen in Fig 4.30. While the feature of shear stress-strain curves of ABS at two lowest shear strain rates are identical to each other, the shear stress-strain curves at three highest shear strain rates are analogue compared to each other. However, In contrast to uniaxial tension and compression, the shape of shear stress-shear strain curves change with shear strain rate.

4.4 Three-Point Bending

Mechanical response of ABS to flexural loads with various deformation rates from very low (0.005 mm/s) to moderate (10 mm/s) was evaluated by means of 3-point bending tests. ABS material was forced to be simultaneously subjected to there various stress states such as tension, compression and shear through 3-point bending tests. The dictated stress states by 3-point bending tests with different deformation rates reflect the actual material behavior of ABS because it covers all material aspects of ABS, including strain rate dependence and different behavior in tension and compression as well as shear.

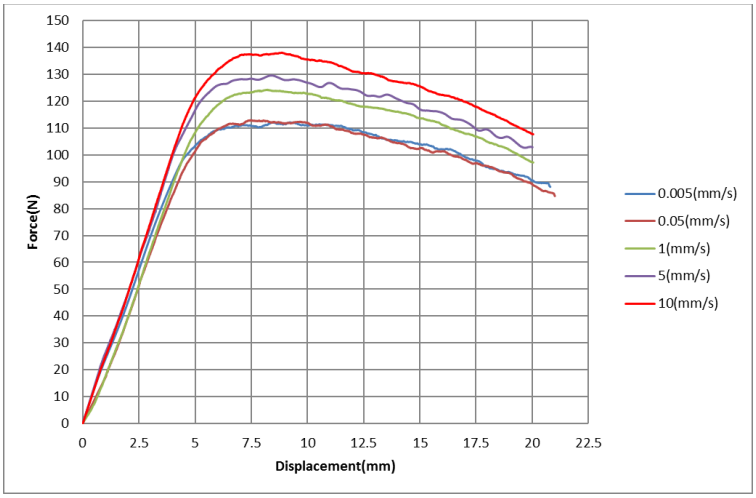

Fig 4.31. Comparisions of 3-Point Bending Load-Displacement Curves of ABS at Various Test Speeds

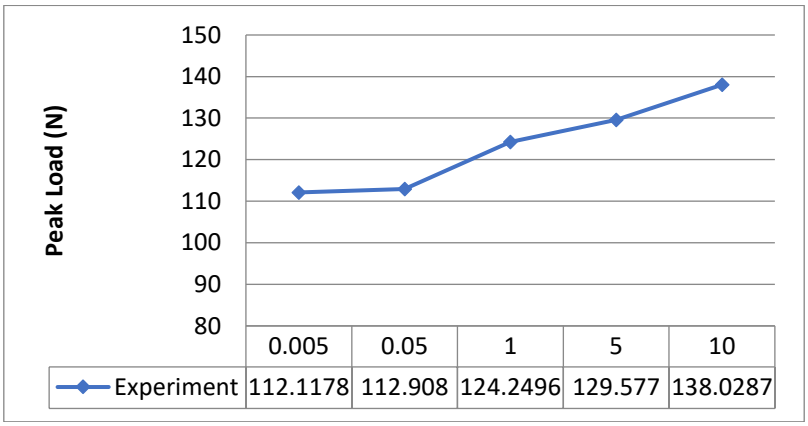

Fig 4.32. Peak loads vs. deformation rates for ABS under 3-point bending

The measured 3-point bending loads were plotted against displacements for each deformation rate as illustrated in Fig 4.30. The feature of load-displacement curves is similar in each deformation rate except for peak loads as indicated in Fig 4.31. Higher deformation rates result a higher peak load. In other words, ABS acts much stiffer with an increasing deformation rates under -3-point bending. This behavior is completely expected since a higher deformation rate imposes higher strain rate deformation and as explained before, yield strength of ABS under all those stress states increases with an increasing strain rate.

4.5 Multiaxial Impact

The impact behavior of ABS was determined through the conducted impact experiments under three different impact velocities such as 4.43 (m/s), 5.775 (m/s) and 6.264 (m/s) that were attained in drop weight impact tower by the drop of 4 kg projectile with 1.3 inch nose radius from three different heights including 1m, 1.7m and 2 m, respectively. The necessary outcomes of impact tests like impact force, displacement and kinetic energy variation during impact to the determination of impact behavior of ABS was measured and compared to one another.

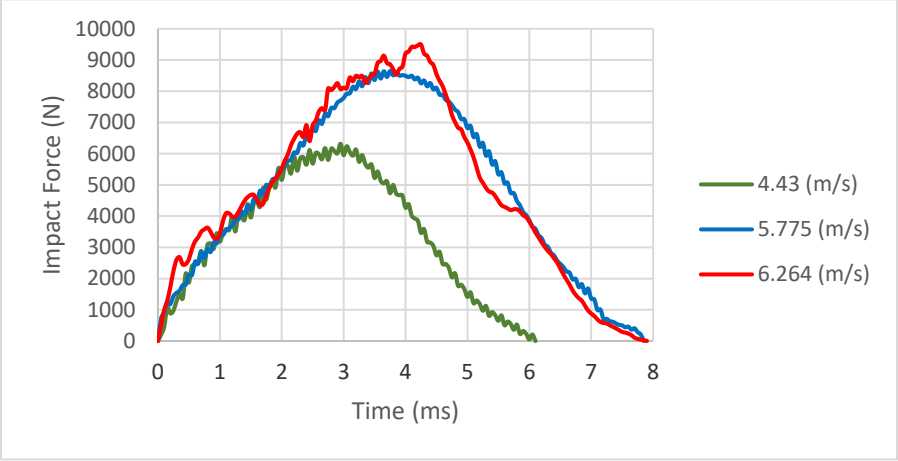

Fig 4.33. Comparisons of experimental impact forces under various impact velocities

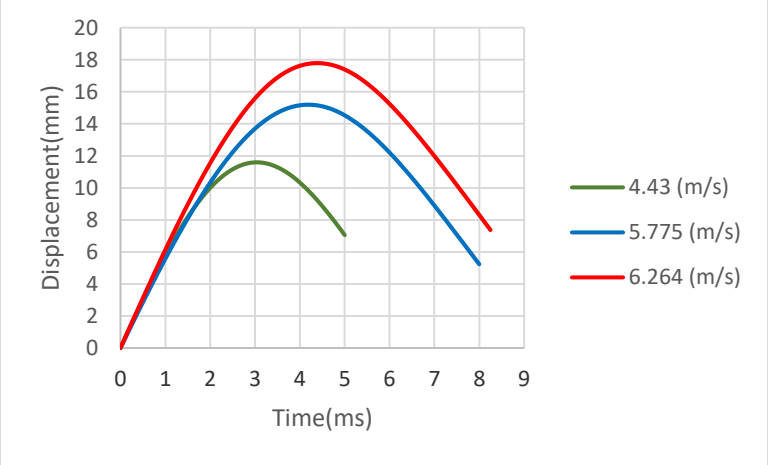

Fig 4.34. Comparisons of experimental displacements under various impact velocities

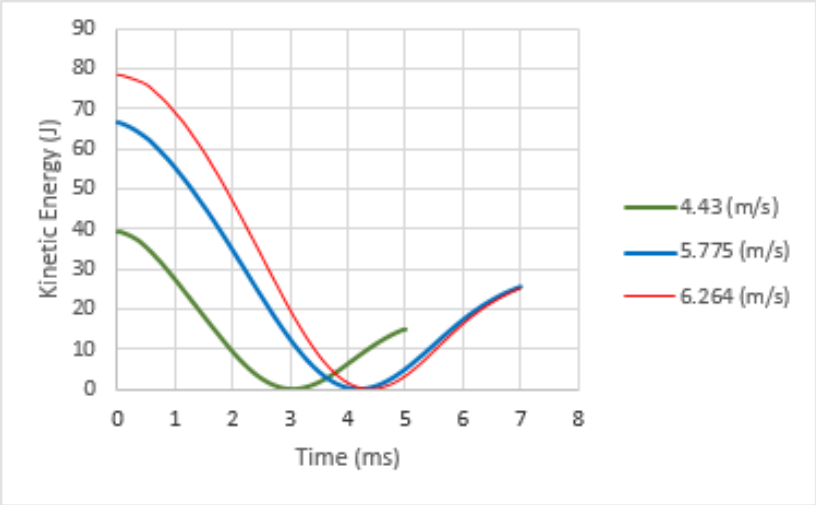

Fig 4.35. Comparisons of kinetic energy variations under various impact energies

There is an increase in impact force and displacement with an increased impact velocity. Both impact forces and displacements nearly reach their peaks at the same period of time for impact velocities of 5.775 (m/s) and 6.264 (m/s).

Strains and strain rates during impact were measured for each impact velocity using three strain gages placed near impact point at the back surfaces of ABS as shown in Fig 4.35.

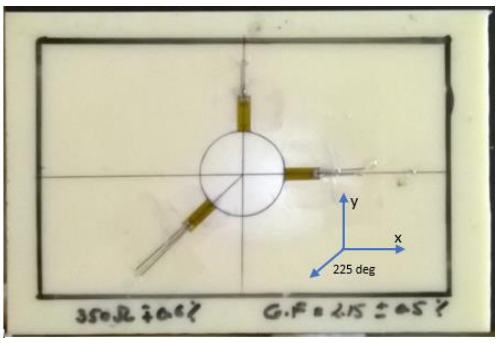

Fig 4.36. Back surface of ABS with strain gages after impact (velocity= 4.43 (m/s))

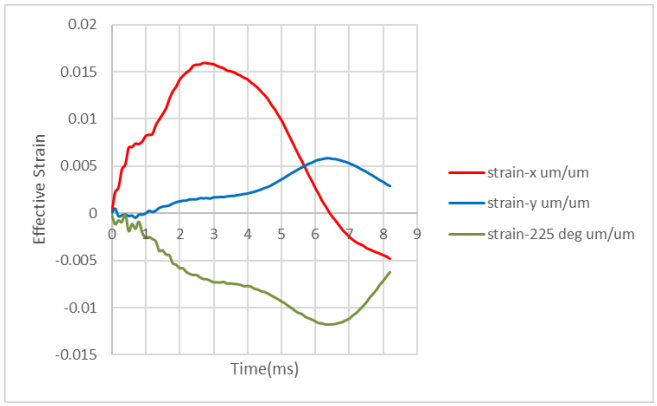

Fig 4.37. Measured strains near impact area under impact velocity of 4.43 (m/s)

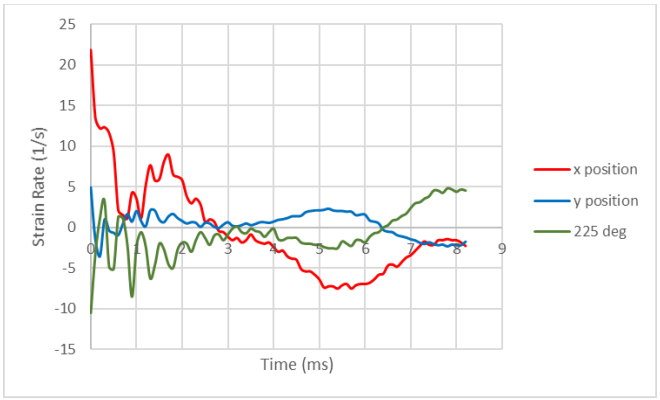

Fig 4.38. Measured strain rates near impact area under impact velocity of 4.43 (m/s)

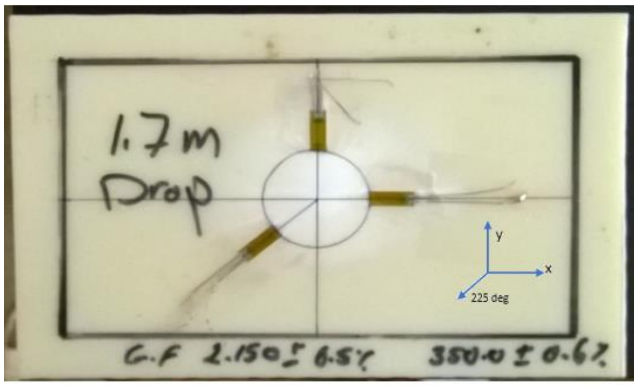

Fig 4.39. Back surface of ABS with strain gages after impact velocity of 5.775 (m/s)

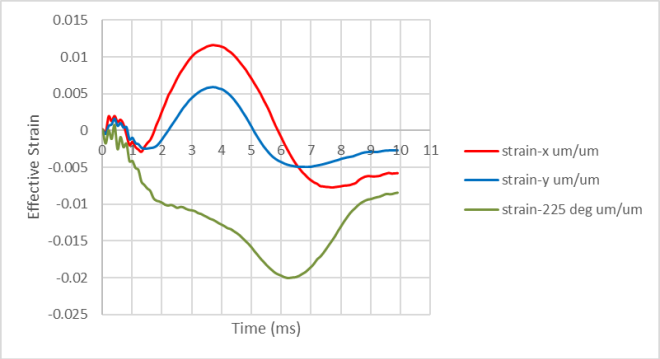

Fig 4.40. Measured strains near impact area under impact velocity of 5.775 (m/s)

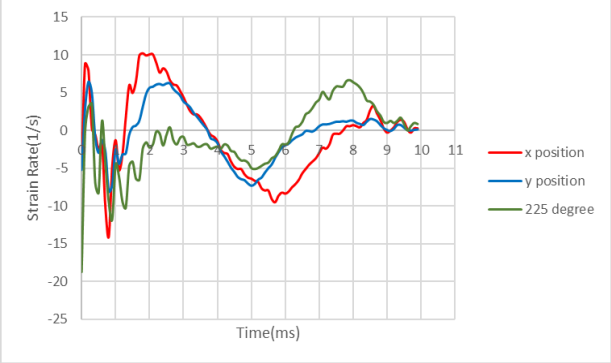

Fig 4.41. Measured strain rates near impact area under impact velocity of 5.775 (m/s)

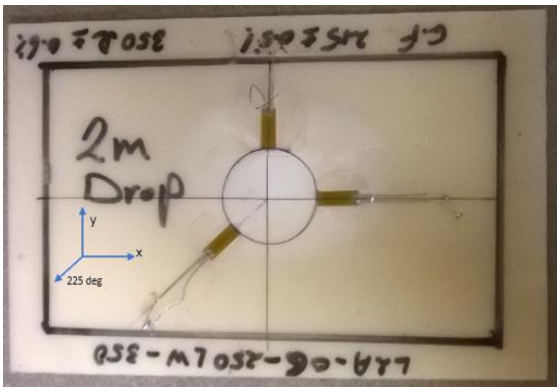

Fig 4.42. Back surface of ABS with strain gages after impact velocity of 6.264 (m/s)

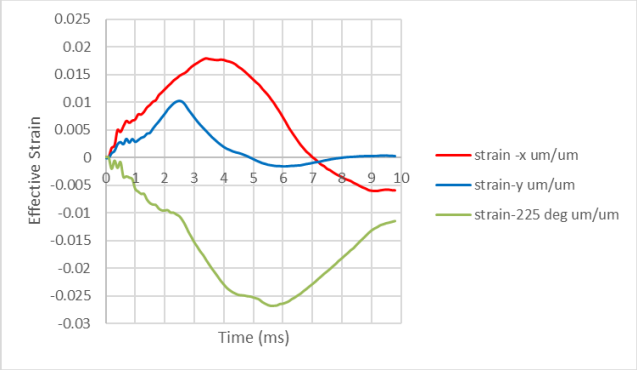

Fig 4.43. Measured strains near impact area under impact velocity of 6.264 (m/s)

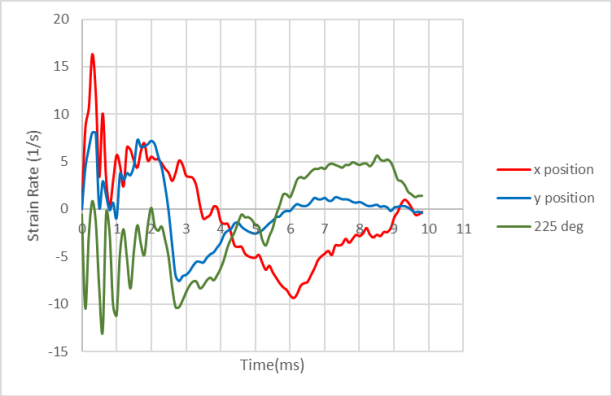

Fig 4.44. Measured strain rates near impact area under impact velocity of 6.264 (m/s)

Although none of the impact energy caused a catastrophic failure in ABS, color changes were observed at the back surface of ABS after impact in all impact energies. Natural color of ABS turned into white near impact areas at the back surfaces. No color change was noticed at the front surfaces where the projectile hit the ABS. This color change is a common phenomenon in amorphous thermoplastics and it is known as stress whitening that only occurs under tension. The back surface of ABS is under tension and front surface is under compression during impact. This color change express that a localized material changes in ABS during impact are formed under all impact energies because chaotically arranged chain macromolecules under tension elongates and they move their new locations; however, when they change their initial positions micro voids are

formed between chains and accumulated throughout to deformation. The accumulated micro voids are the reason behind a color change at the back surfaces of ABS during impact tests. When we inspect the damage areas with ultrasonic c-scan and surfaces with laser scanning microscopy we will have more fundamental understanding of the reason behind color change at the back surfaces of ABS.

In the beginning of impact tests, all strain gages recorded very high strain rates. In other words, strain rates jumped up to their maximum values and then they decreased sharply and after that started to fluctuate. If we do not consider the very absurd increase of strain rates in the beginning of impacts, the detected maximum strains and strain rates can be documented as follows.

Table 4.7. The recorded maximum strains and strain rates for impact velocity of 4.43 (m/s)

Strain gage position	**Maximum strain**	**Maximum strain rate(s^{-1})**
x position	0.016	8.5
y position	0.0052	2.5
225 deg	-0.0125	-7.3

Table 4.8. The recorded maximum strains and strain rates for impact velocity of 5.775 (m/s)

Strain gage position	**Maximum strain**	**Maximum strain rate(s^{-1})**
x position	0.0115	10
y position	0.0052	5.2
225 deg	-0.02	-10.5

Table 4.9. The recorded maximum strains and strain rates for impact velocity of 6.264 (m/s)

Strain gage position	**Maximum strain**	**Maximum strain rate(s^{-1})**
x position	0.0172	10
y position	0.01	5.5
225 deg	-0.0265	-13

The tabulated results in terms of strains and strain rates need to be validated through the comparisons of numerical outcomes because we observed unusual deformation pattern near strain gages, perhaps glue that we used in placing strain gages on the surface of ABS caused a stiffness change in ABS.

CHAPTER 5 NUMERICAL RESULTS

5.1 Uniaxial Tension

Elastic and plastic material material properties of ABS obtained from uniaxial tension tests under different strain rates were used in the numerical implementations of uniaxial tension tests. Mat Samp-1 uses only constant tensile elastic modulus for all strain rates but the tensile elastic modulus of ABS is strain rate dependent that can be seen in Table 4.2. Therefore we took the average tensile elastic modulus. The elastic material parameters of ABS used in the simulations are reported in Table 5.1.

Table 5.1. The used elastic material properties of ABS in the simulations of uniaxial tension tests

Tensile Modulus (MPa)	Poisson's Ratio	Density (tonn/mm^3)
1937	0.38	1024e-12

Plastic material properties and strain rate effect on yield stresses of ABS were introduced to the material model (Mat Samp-1) through tablutated data of experimentally determined five distinct true plastic strain-true plastic stress curves as a function of strain rate as show in Fig 5.1. Also the plastic poisson's ratio measured with DIC during uniaxial tension test under the lowest strain rate was used as an input. The actual elongation rates attained in uniaxial tension tests were directly applied to the ABS in our simulations. Our material model selects the tabulated data that is defined as a function of strain rate based on corresponded strain rate produced by deformation speed. After numerical implementations of uniaxial tension tests carried on ABS, corresponded strain rates were numerically extracted for there actual deformation rates such as 1 (mm/s) , 5 (mm/s) and 10 (mm/s)

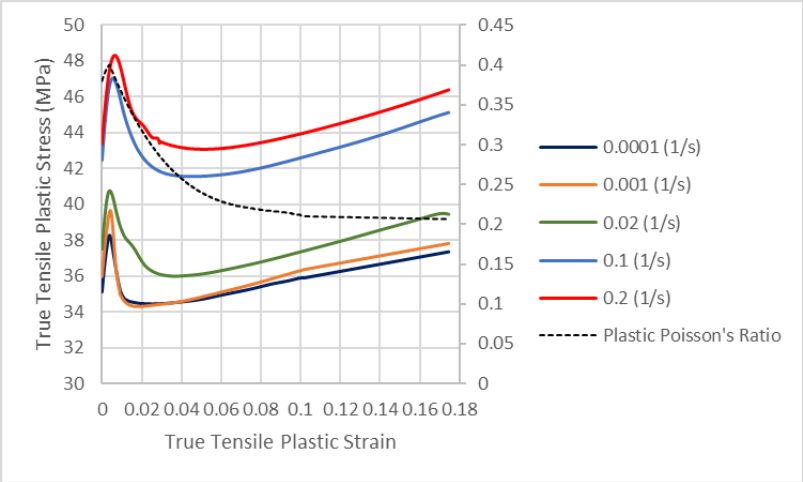

Fig 5.1. The used test data as an input in SAMP-1 for numerical implementation of uniaxial tension tests

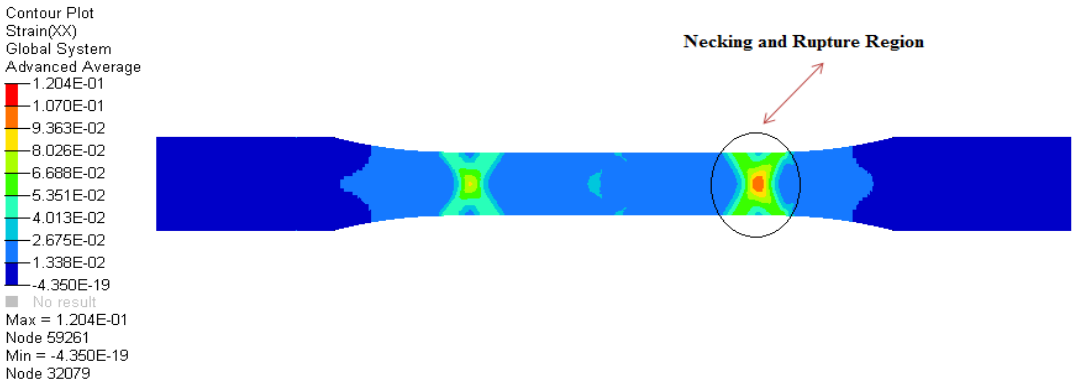

Fig 5.2. Strain (XX) Contour of Uniaxial Tension Specimen at Elongation Speed of 0.005 (mm/s)

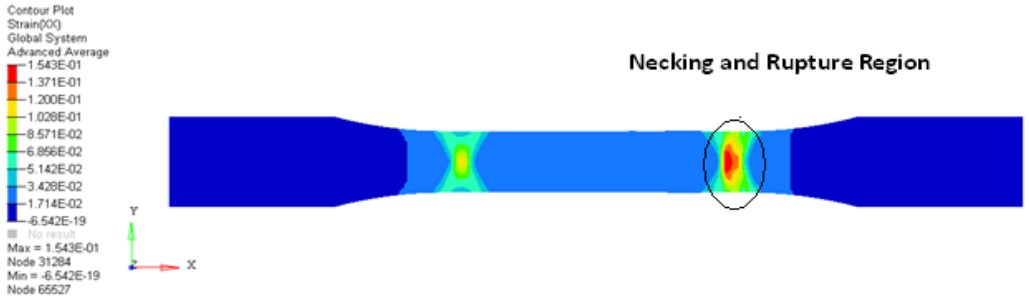

Fig 5.3. Strain (XX) Contour of Uniaxial Tension Specimen at Elongation Speed of 0.05 (mm/s)

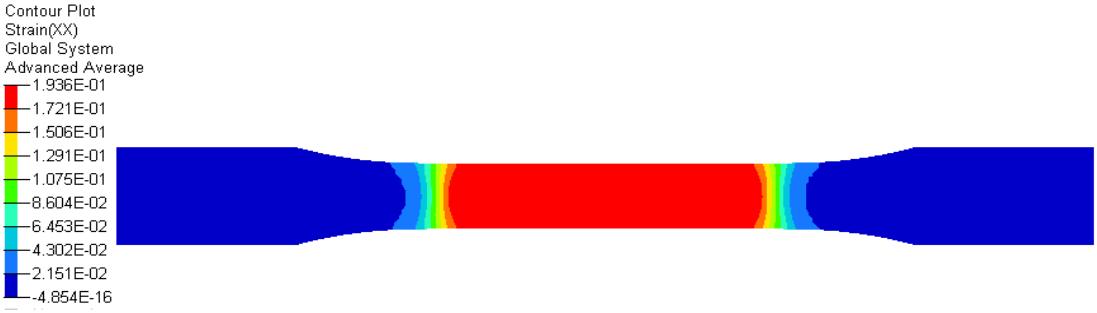

Fig 5.4. Strain (XX) Contour of Uniaxial Tension Specimen at Elongation Speed of 1 (mm/s)

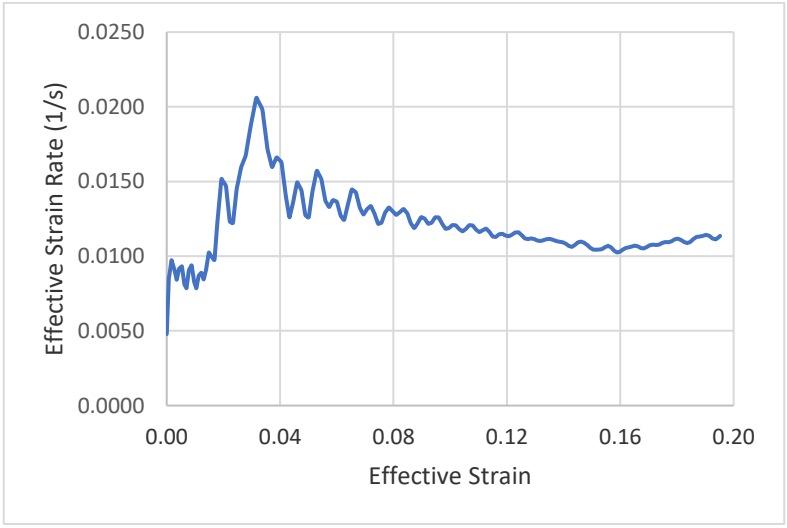

Fig 5.5. Effective strain rate vs effective strain under elongation speed of 1 (mm/s)

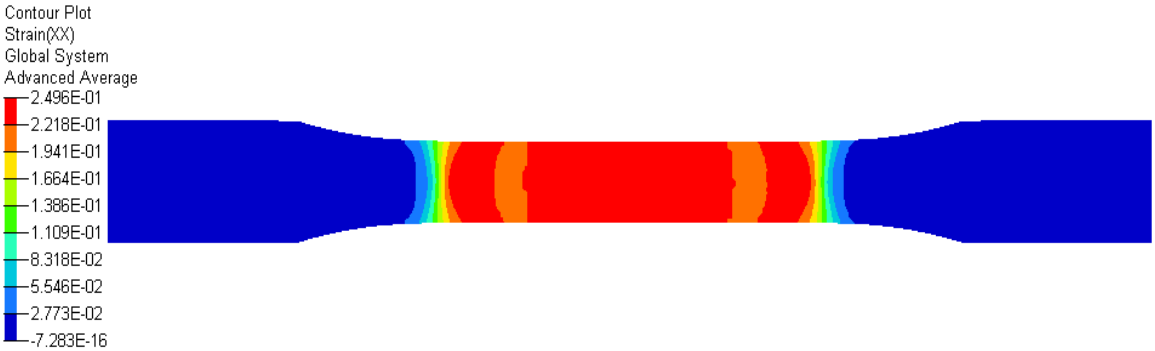

Fig 5.6. Strain (XX) Contour of Uniaxial Tension Specimen at Elongation Speed of 5 (mm/s)

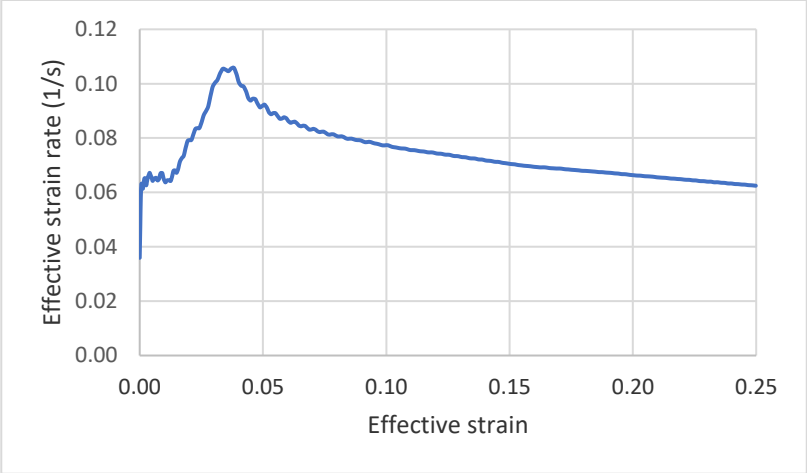

Fig 5.7. Effective strain rate vs effective strain under elongation speed of 5 (mm/s)

Fig 5.8. Strain (XX) Contour of Uniaxial Tension Specimen at Elongation Speed of 10 (mm/s)

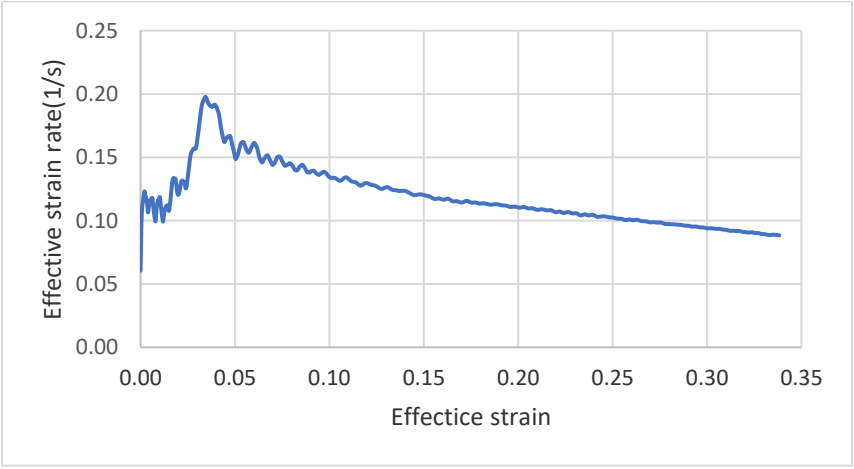

Fig 5.9. Effective strain rate vs effective strain under elongation speed of 10 (mm/s)

5.2 Uniaxial Compression

The utilized stress strain curves as a tabulated data in our finite element material model (Samp-1) to the prediction of compressive response of ABS are illustrated in Fig 5.10. In contrast to finite element modeling of uniaxial tension tests, we did not define any strain rate dependence through multiple tension stress-strain curves as a function of strain rate since uniaxial compression test impose homogenous stress state ;therefore, each compressive true stress-true strain curve experimentally obtained from each deformation rate were separetly utilized in simulations implying that one compressive true plastic stress-true plastic strain curve as a tabulated data was used in each simulation. Using at least one tensile stress-strain curve is required in mat Samp-1. For this reason, we used only one tensile stress-strain curve obtained from quasi-static uniaxial tension test.

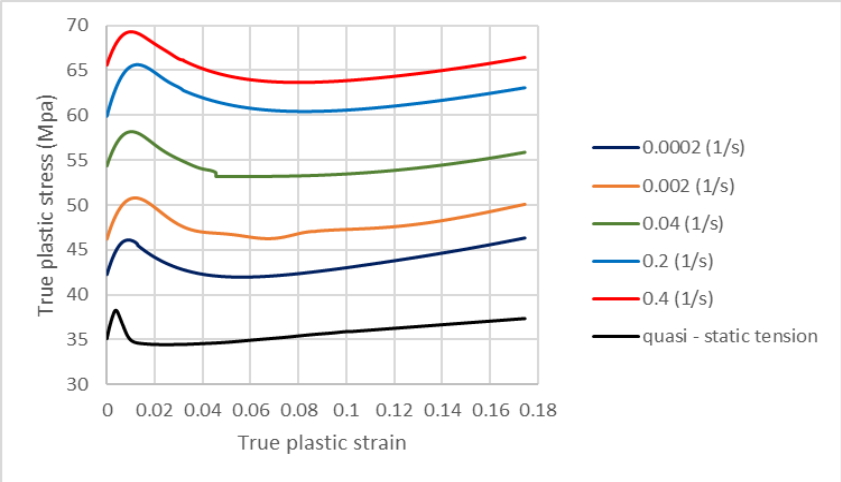

Fig 5.10. The used test data for numerical implementation of uniaxial compression tests.

Additionaly, plastic Poisson's ratio as a function of plastic strain obtained from quasi-static tension test was introduced to our material model as illustrated in Fig 5.11. Under pure compression, Mat Samp-1 accepts the variation of plastic Poisson's ratio with negative plastic strains.

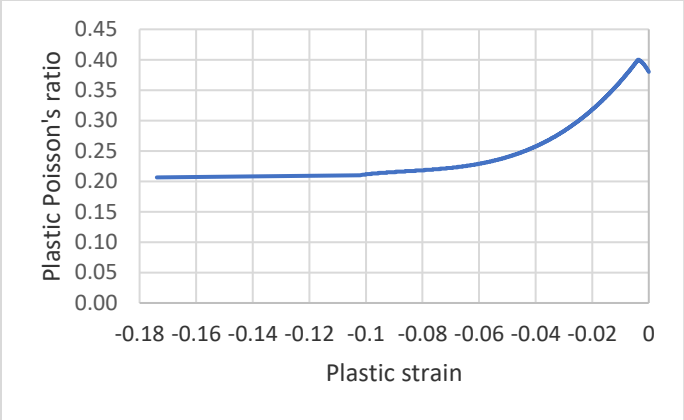

Fig 5.11. Plastic Poisson's ratio as a function of plastic strain

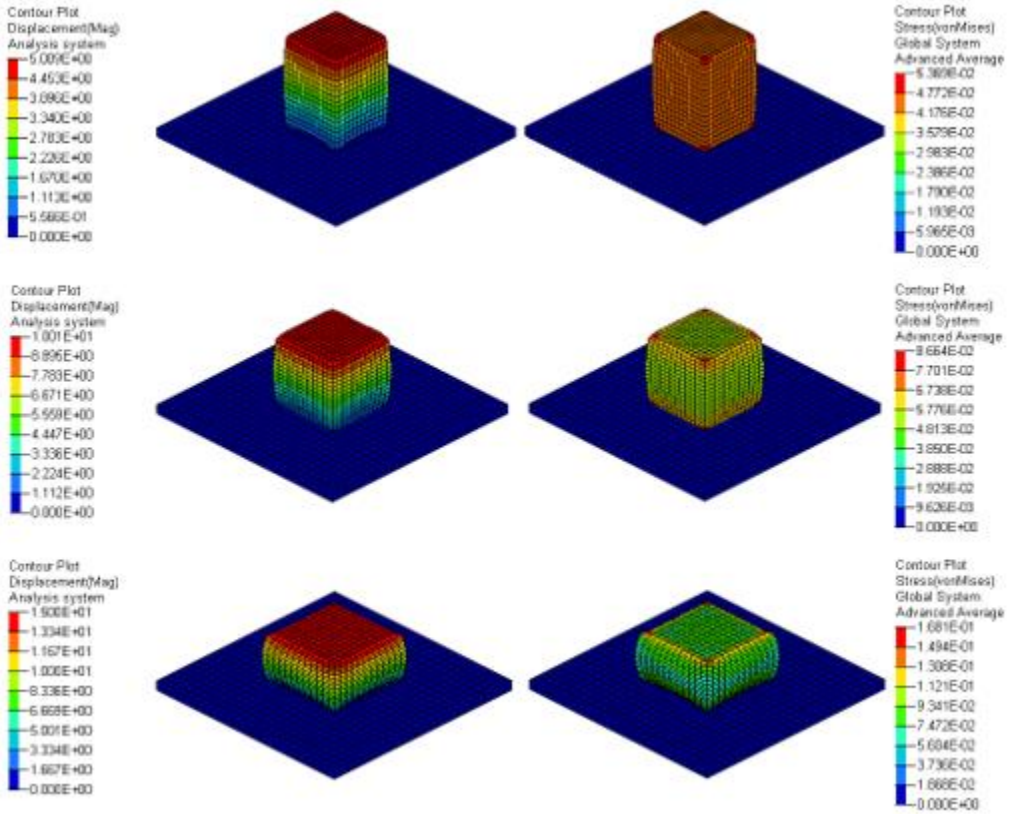

Fig 5.12. Displacement (mm) and corresponding Von-Misses Stress (GPa) contours of compresssed ABS specimen under 0.005 (mm/s) compressive rate.

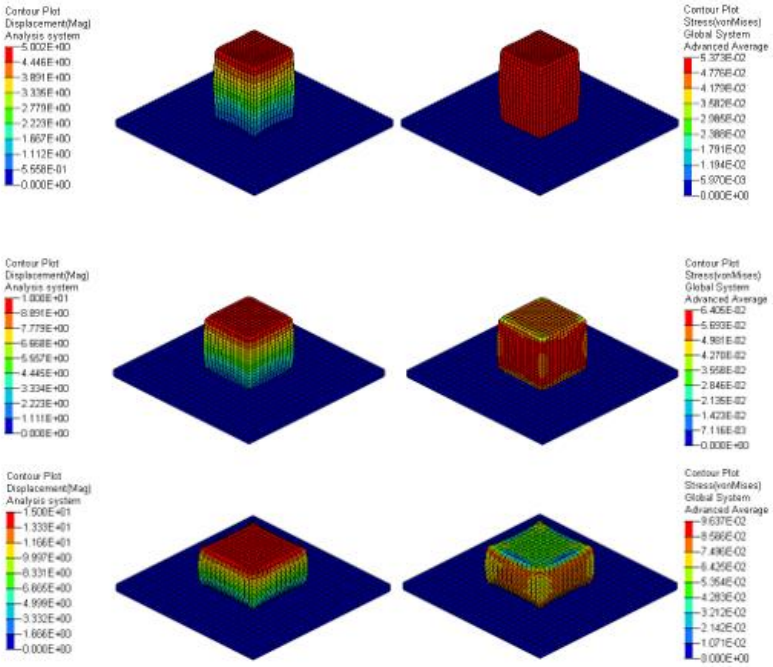

Fig 5.13. Displacement (mm) and corresponding Von-Misses Stress (GPa) contours of compresssed ABS specimen under 0.05 (mm/s) compressive rate.

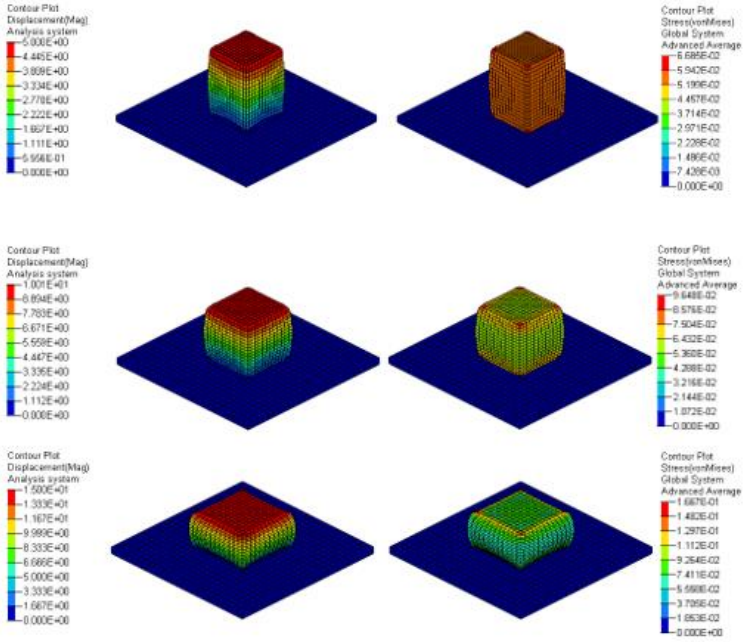

Fig 5.14. Displacement (mm) and corresponding Von-Misses Stress (GPa) contours of compresssed ABS specimen under 1 (mm/s) compressive rate.

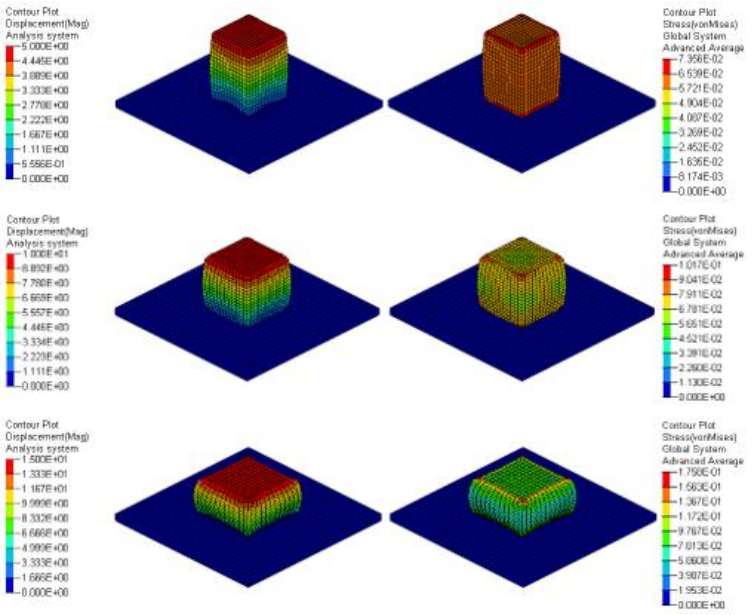

Fig 5.15. Displacement (mm) and corresponding Von-Misses Stress (GPa) contours of compresssed ABS specimen under 5 (mm/s) compressive rate.

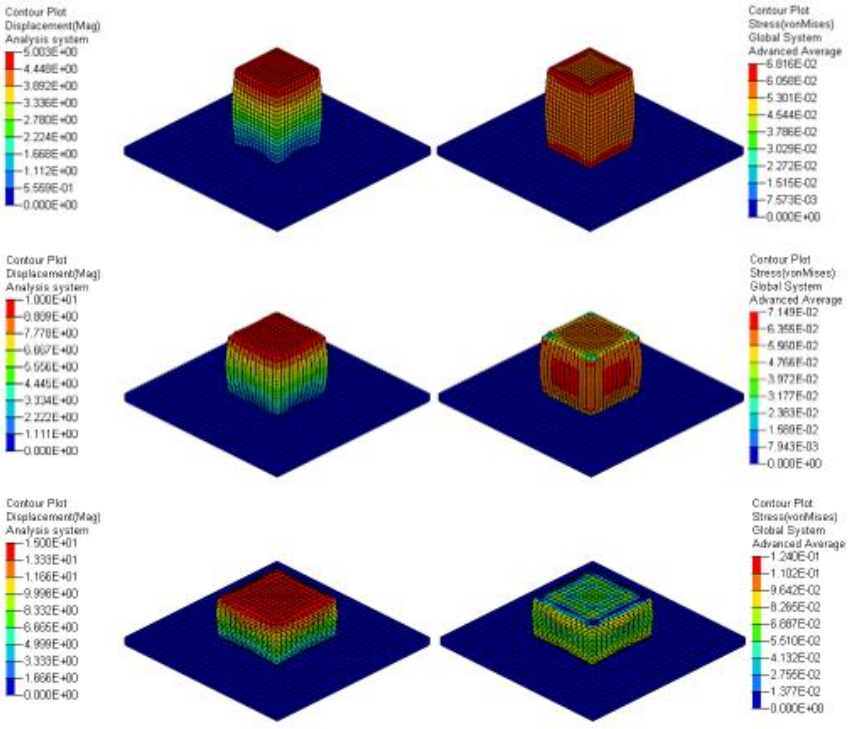

Fig 5.16. Displacement (mm) and corresponding Von-Misses Stress (GPa) contours of compresssed ABS specimen under 10 (mm/s) compressive rate.

5.3 3-Point Bending

The used experimental data in the numerical simulations of 3-point bending test is indicated in Fig 5.17. Five various tension test data as a function of strain rate , one quasi- static compression test data and one quasi-static shear test data were assigned for the material charazterization of ABS to our material model Mat-SAMP-1. The exact test speeds attained in 3-point bending tests were directly dictated to finite element modelling of the loading nose, as a result of distinct speeds of loading nose, different strain rate deformations were accomplished. Based on the resulting strain rate during deformation, the material model mat-SAMP-1 takes the appropriate tension test data given as a function of strain rate into account. This material model considers the tension test data with lowest strain rate as quasi static and assumes that compression and shear test data are obtained under the same rate deformation of tension test data with the lowest strain rate provided to the material model. Hence, the Mat SAMP-1 linearly increases the compressive and shear yield surfaces based on produced strain rate during deformation. In other words, whatever the ratio between quasi static tension true yield stress and the corresponding yield stress based on the strain rate obtained during deformation, the compressive and shear yield surface is increased with the same ratio. If the resulting strain rate is between two given tension test data as a function of strain rates , the model uses linear interpolation to derive the tensile true plastic stress-true plastic strain curve. The generated effective strain rates in the numerical simulations of 3-point bending tests were numerically obtained where the maximum effective strains were observed and documented. To observe closely the effect of shear test data and particularly compression test data on the mecahnical response of ABS under 3-point bending, compression and shear test data were removed from the material model and the same simulations were run again for each deformation rate. If there is no compression and shear test data utilized as an input in Mat SAMP-1, it predicts

the response depending on Von-Misses plasticty assuming that the material behavior under tension is analogoue under compression but this is not true for amorphous thermoplastics. Therefore, the predicted results from the Mat SAMP-1 and Von-Misses plasticy were compared to each other for each deformation rate and documented in the following figures.

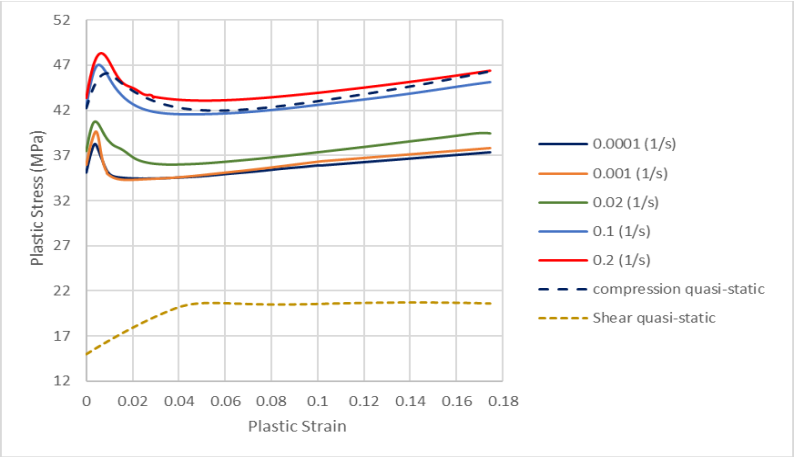

Fig 5.17. The used experimental data in SAMP-1 in the numerical implementations of 3-point bendind tests

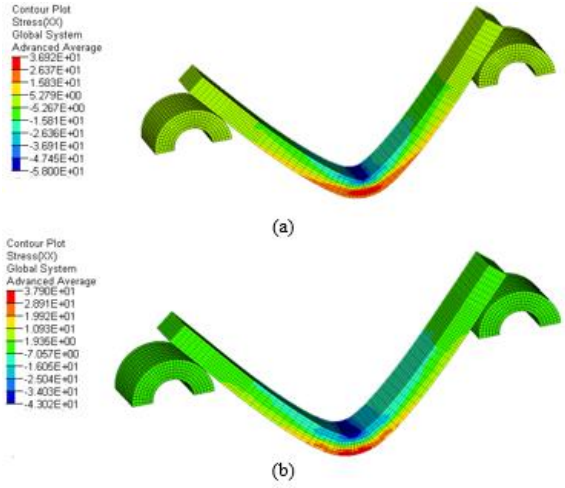

Fig 5.18. Stress(XX) Contour (a) SAMP-1 (b) Von-Misses, at deformation rate 0.005(mm/s)

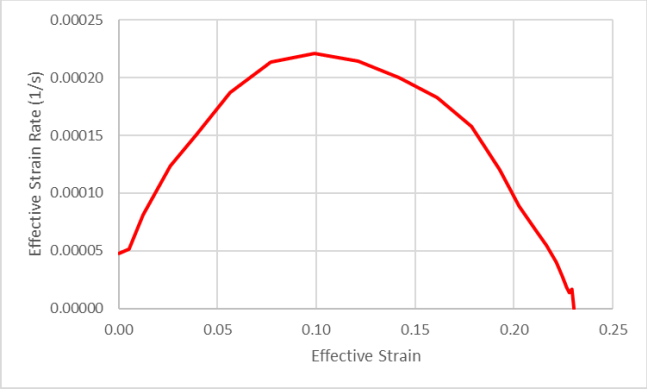

Fig 5.19. Numerically obtained effective plastic strain-effective plastic strain rate under deformation rate of 0.005(mm/s)

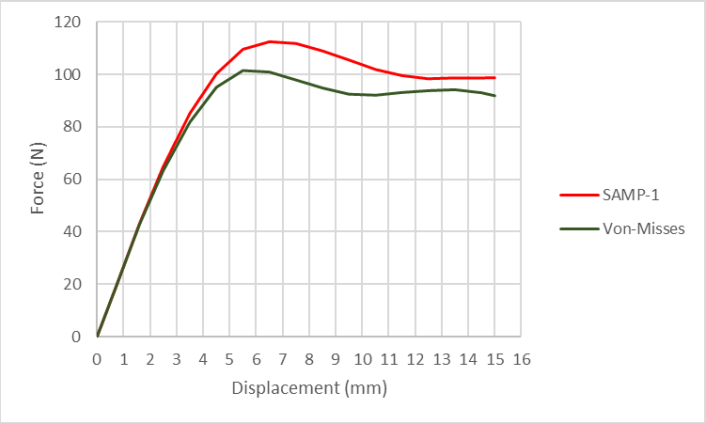

Fig 5.20. SAMP-1 vs. Von-Misses, 3 -point bending force -displacement under deformation rate of 0.005(mm/s)

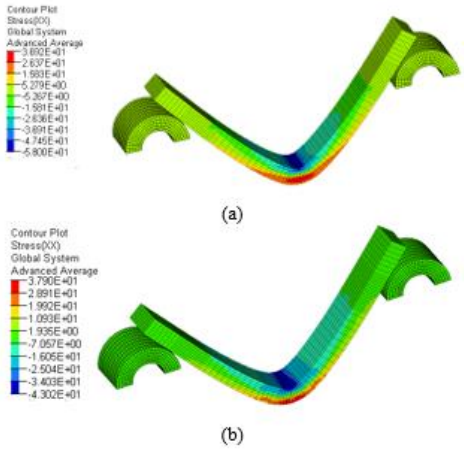

Fig 5.21. Stress(XX) Contour (a) SAMP-1 (b) Von-Misses, at deformation rate 0.05(mm/s)

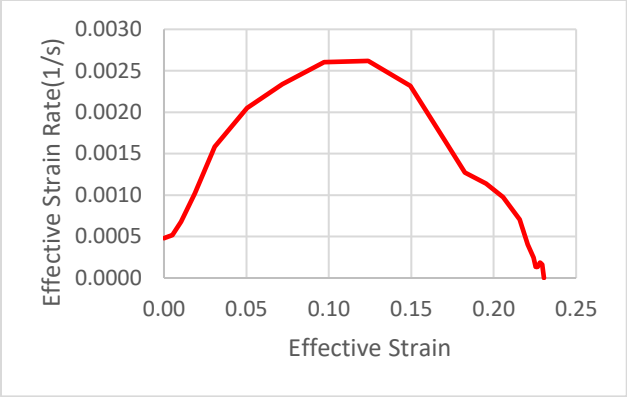

Fig 5.22. Numerically obtained effective plastic strain-effective plastic strain rate under deformation rate of 0.05(mm/s)

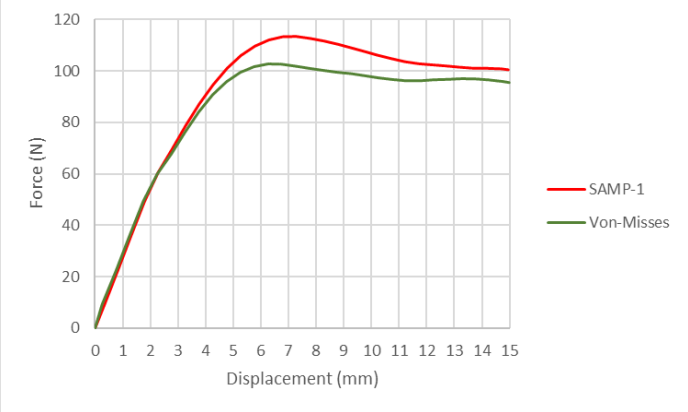

Fig 5.23. SAMP-1 vs. Von-Misses, 3 -point bending force -displacement under deformation rate of 0.05(mm/s)

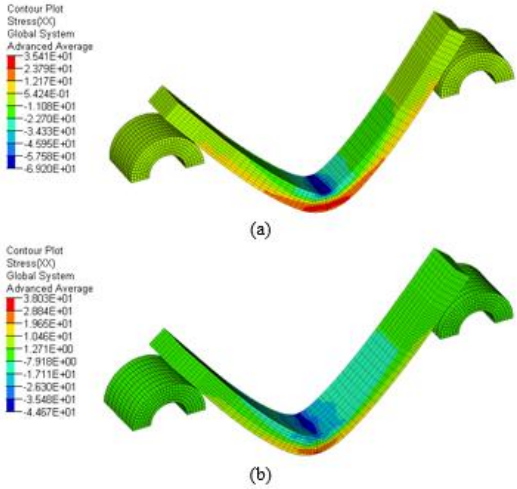

Fig 5.24. Stress(XX) Contour (a) Samp-1 (b) Von-Misses, at deformation rate 1(mm/s)

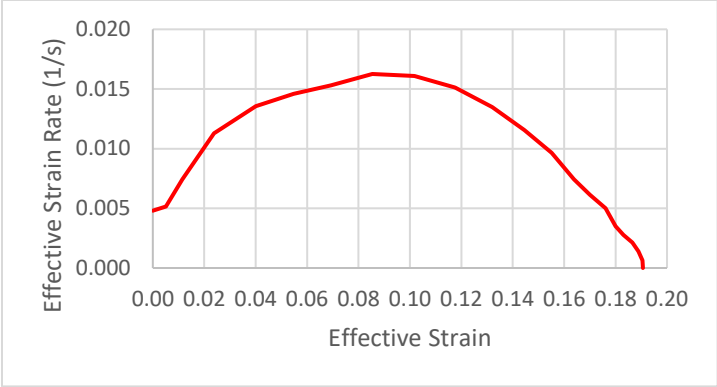

Fig 5.25. Numerically obtained effective plastic strain-effective plastic strain rate under deformation rate of 1(mm/s)

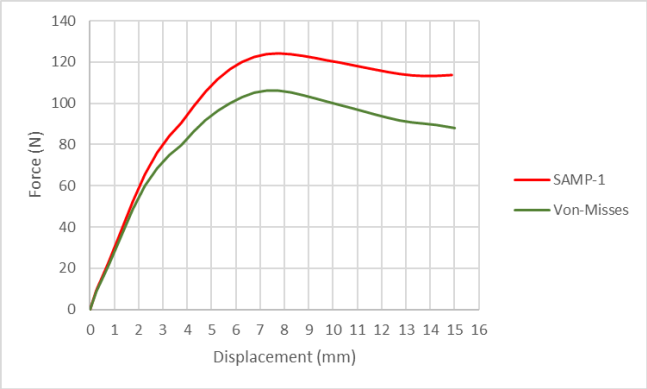

Fig 5.26. SAMP-1 vs. Von-Misses, 3 -point bending force -displacement under deformation rate of 1(mm/s)

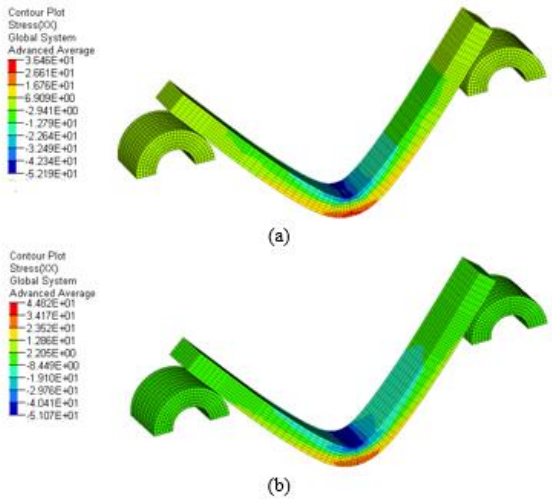

Fig 5.27. Stress(XX) Contour (a) SAMP-1 (b) Von-Misses, at deformation rate 5 (mm/s)

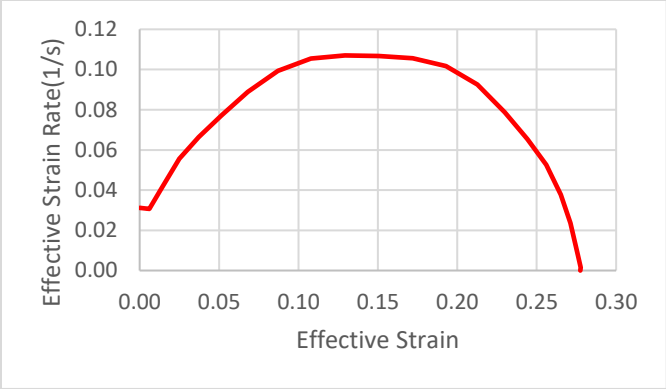

Fig 5.28. Numerically obtained effective plastic strain-effective plastic strain rate under deformation rate of 5(mm/s)

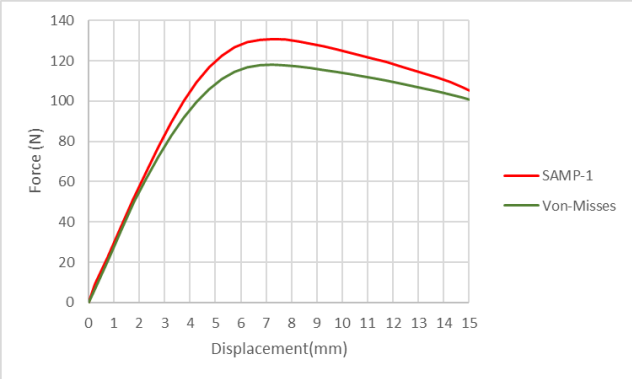

Fig 5.29. SAMP-1 vs. Von-Misses, 3 -point bending force-displacement under deformation rate of 5 (mm/s)

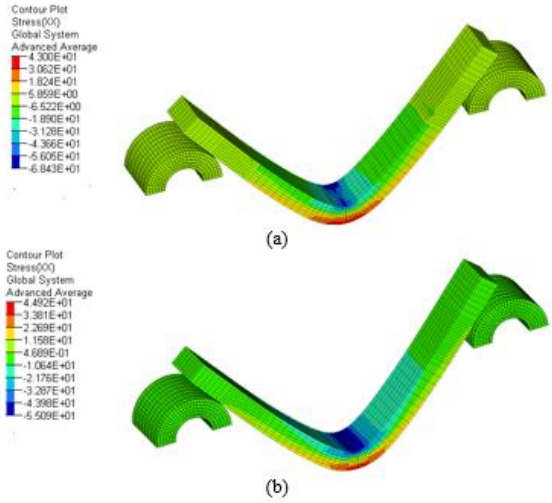

Fig 5.30. Stress(XX) Contour (a) Samp-1 (b) Von-Misses, at deformation rate 10 (mm/s)

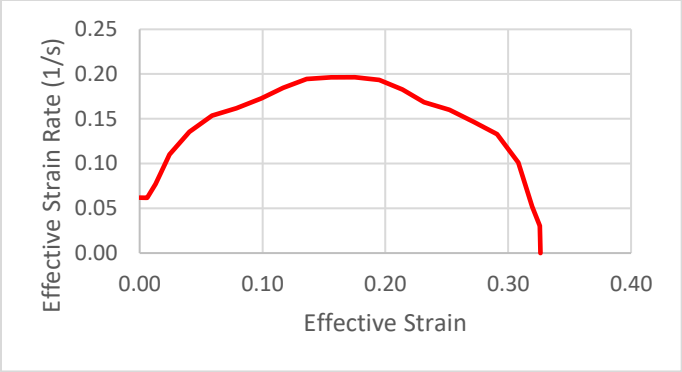

Fig 5.31. Numerically obtained effective strain-effective strain rate under deformation rate of 10 (mm/s)

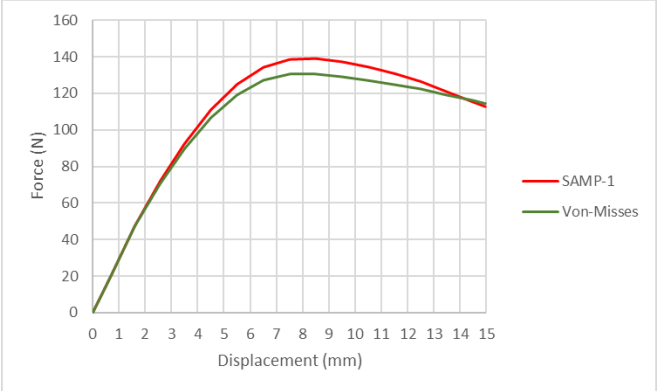

Fig 5.32. SAMP-1 vs. Von-Misses, 3 -point bending force-displacement under deformation rate of 10(mm/s)

5.4 Multiaxial Impact

The input data in SAMP-1 for impact simulations are shown in Fig 5.33. The strain rate dependency are defined through multiple true plastic stress-strain curves for ABS over a wide range of strain rates ranging from 0.0001 (s^{-1}) to 45 (s^{-1}) .Displacement contours during impact and equivalent plastic strains after impact are depicted for each impact velocity in the following figures.

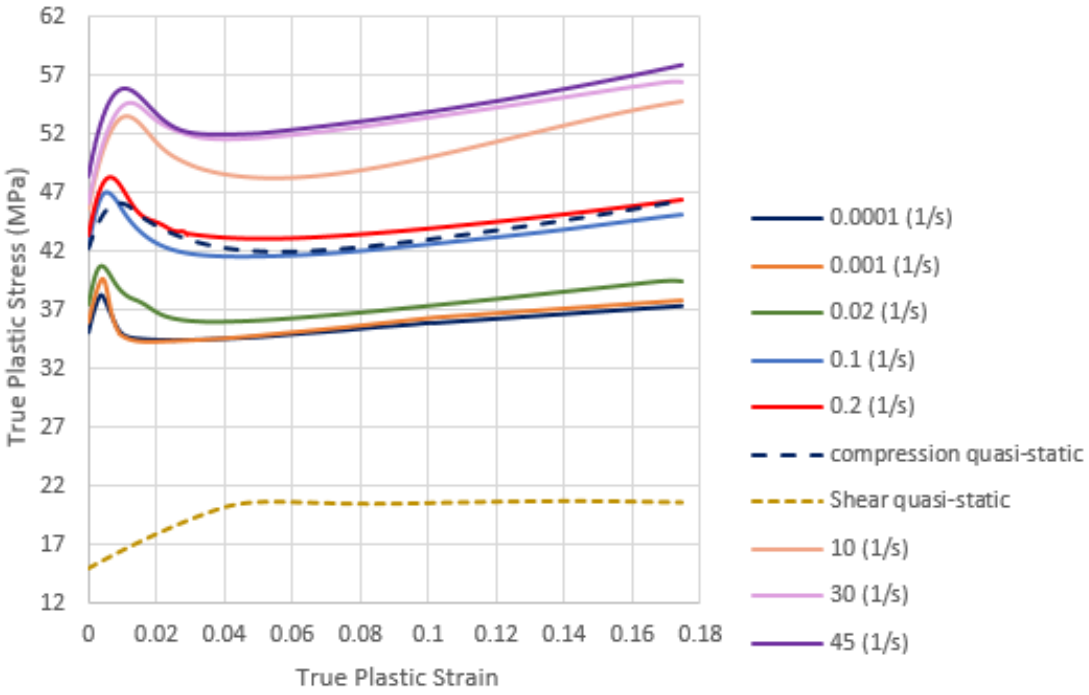

Fig 5.33. The used experimental data in SAMP-1 for impact simulations

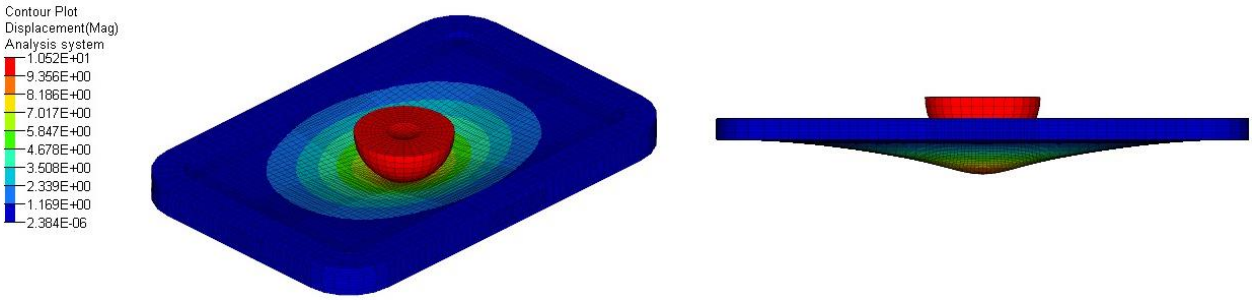

(a) Displacement (10.52 mm) at 2 ms

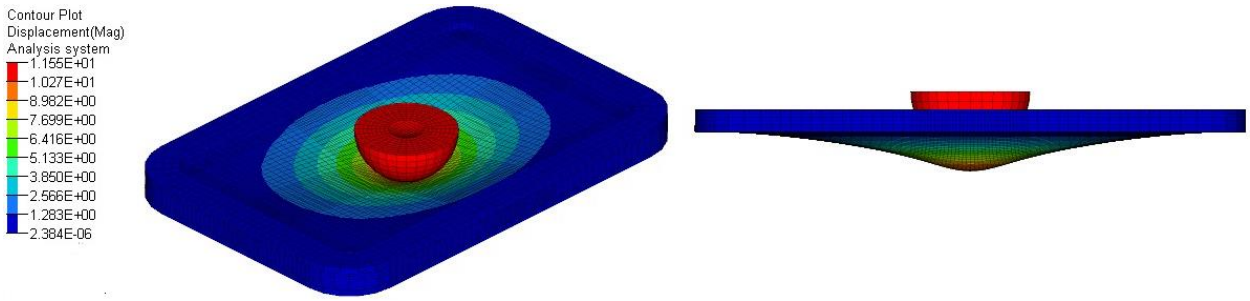

(b) Max displacement (11.55 mm) at 2.92 ms

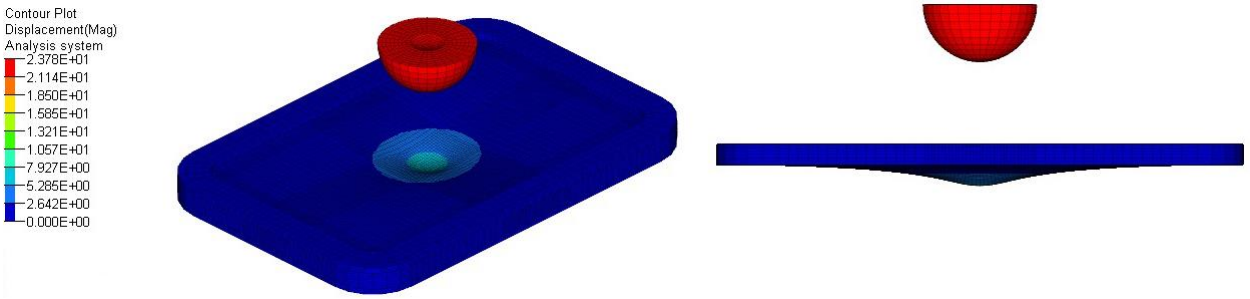

(c) Rebound of the projectile at 12 ms

Fig 5.34. Displacement contour of impacted ABS specimen under 4.43 (m/s) impact velocity

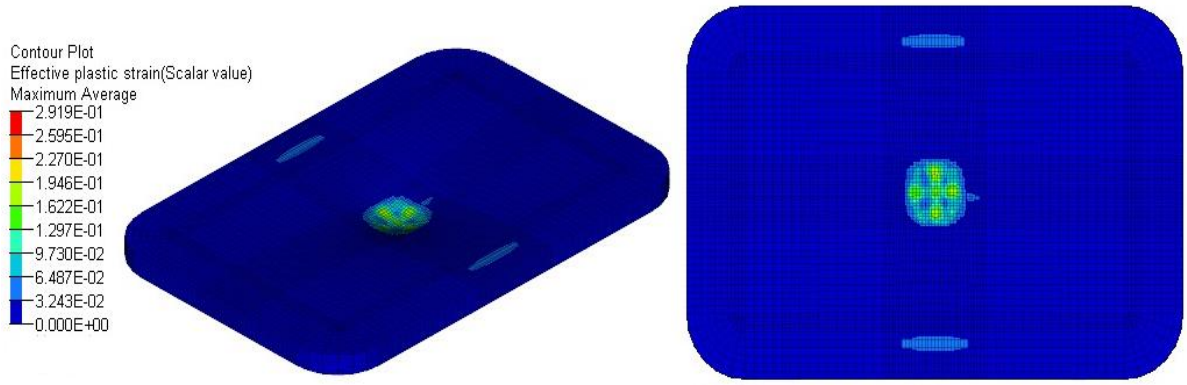

(a)

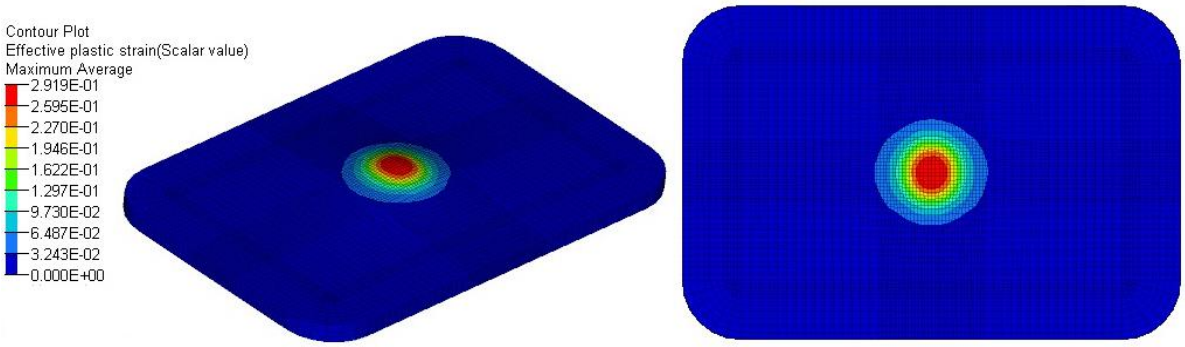

(b)

Fig 5.35. Effective plastic strain under 4.43 (m/s) impact velocity (a) front surface, (b) back surface

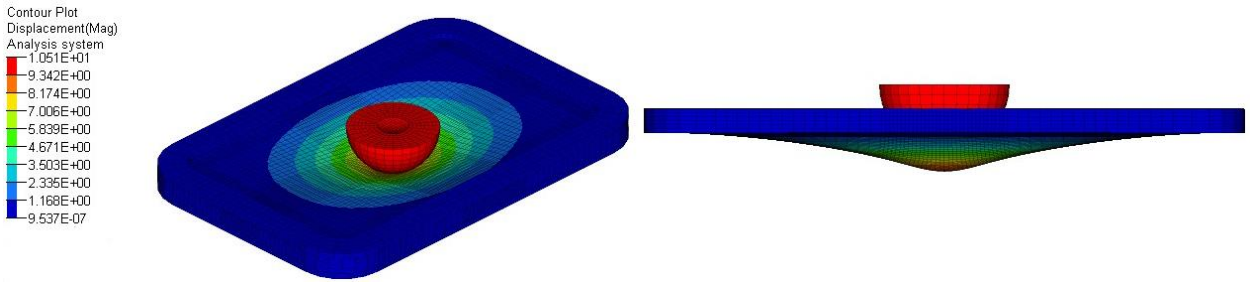

(a) Displacement (10.51 mm) at 2 ms

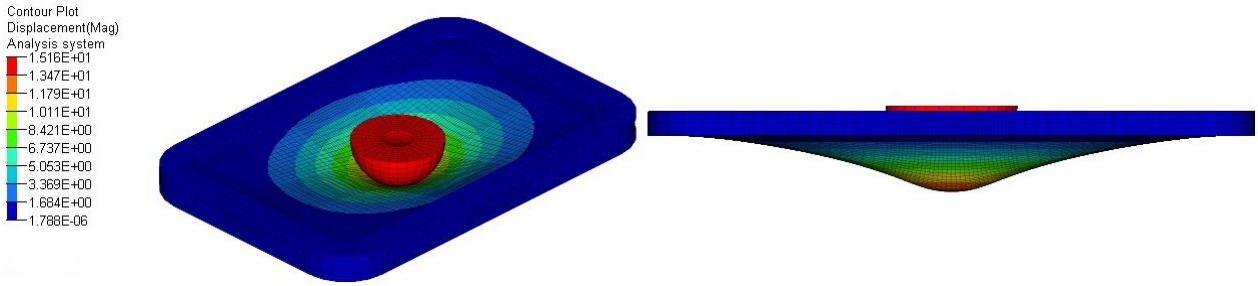

(b) Maximum displacement (15.16 mm) at 4.12 ms

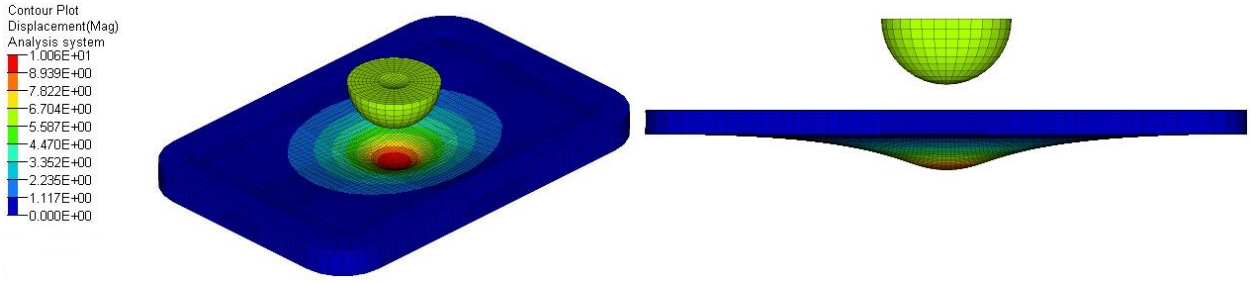

(c) Rebound of the projectile at 12 ms

Fig 5.36. Displacement contour of impacted ABS specimen under 5.775 (m/s) impact velocity

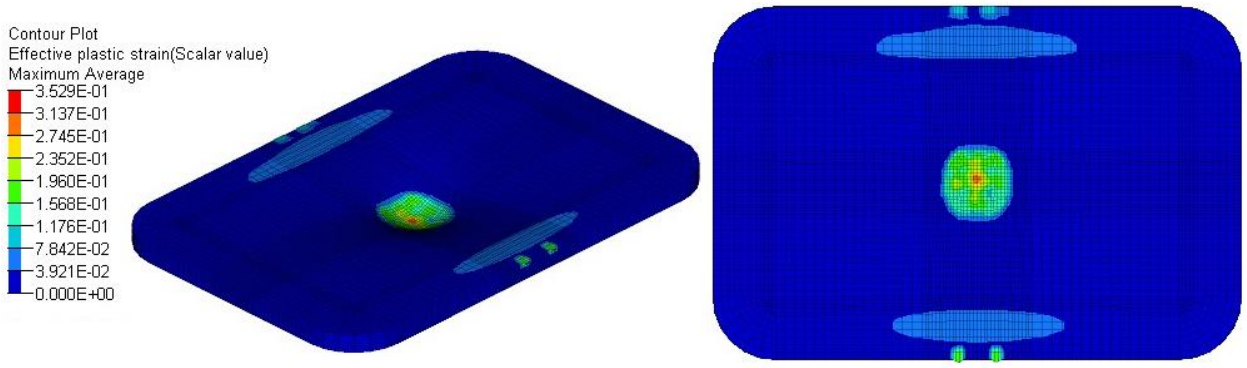

(a)

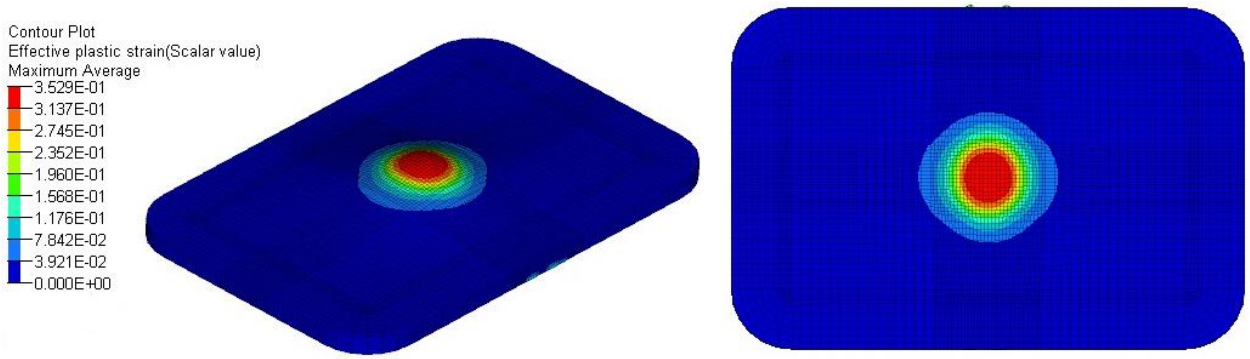

(b)

Fig 5.37. Effective plastic strain under 5.775 (m/s) impact velocity (a) front surface, (b) back surface

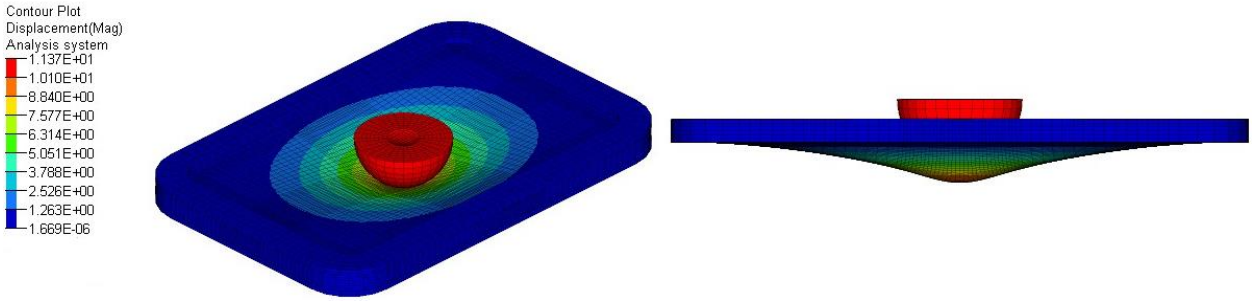

(a) Displacement (11.37 mm) at 2 ms

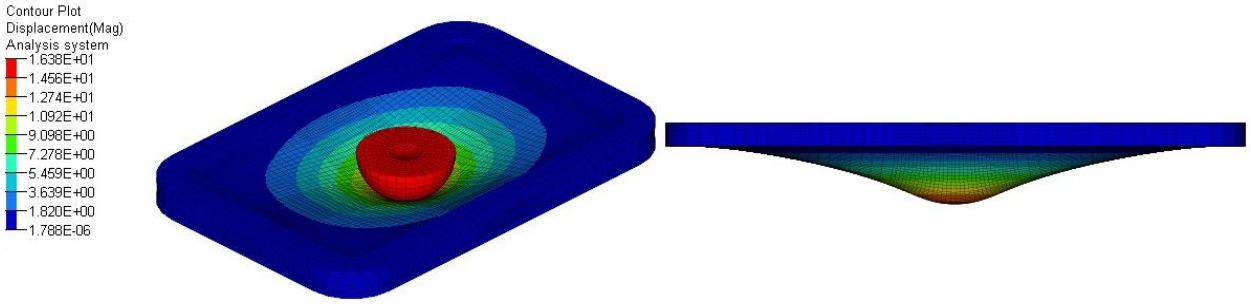

(b) Maximum displacement (16.38 mm) at 4.14 ms

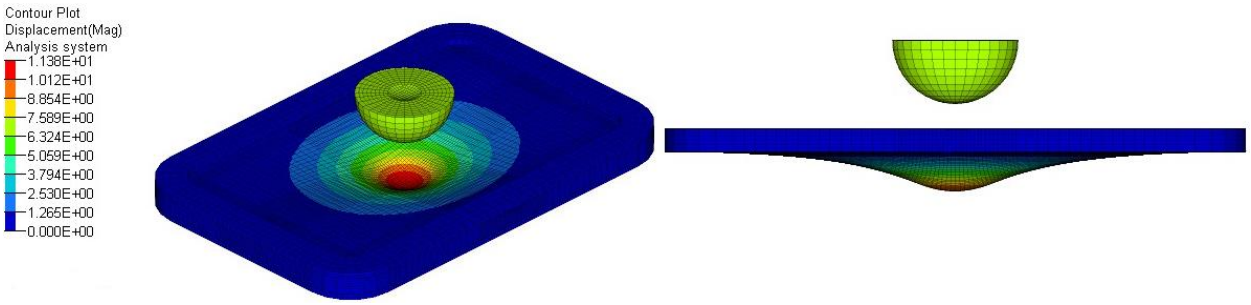

(c) Rebound of the projectile at 12 ms

Fig 5.38. Displacement contour of impacted ABS specimen under 6.264 (m/s) impact velocity

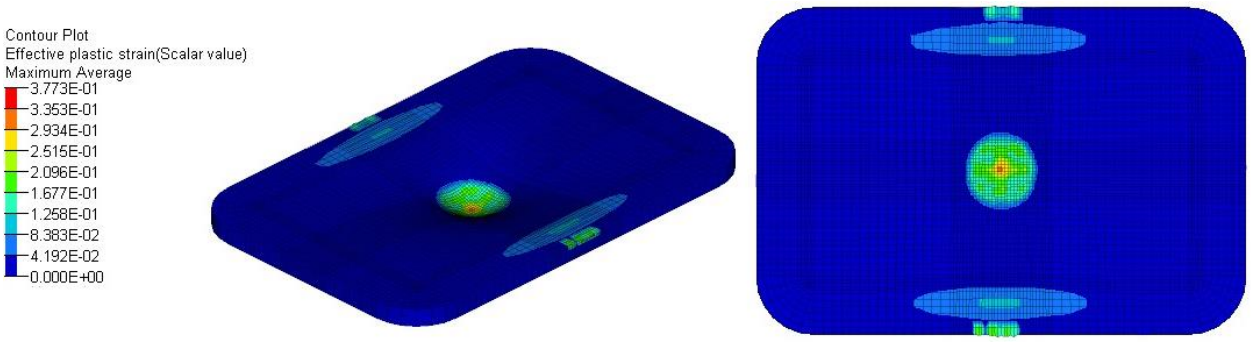

(a)

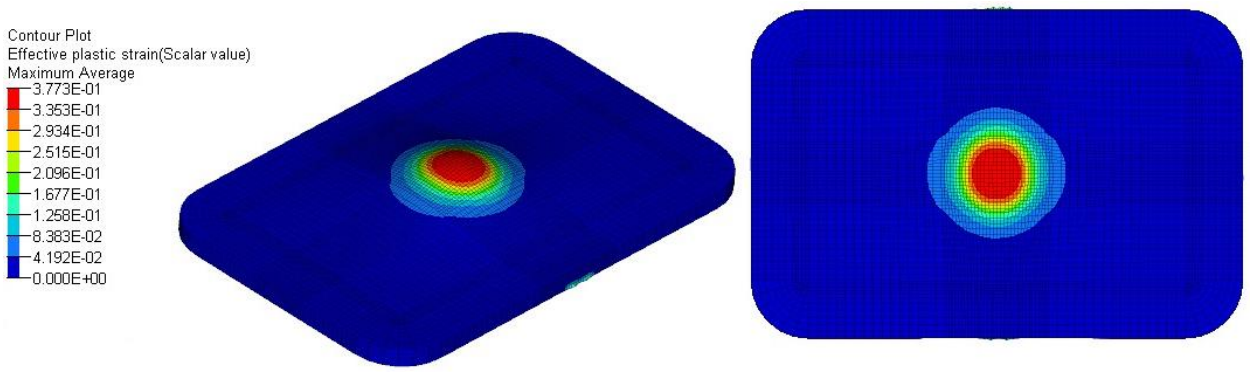

(b)

Fig 5.39. Effective plastic strain after 6.264 (m/s) impact, (a) front surface, (b) back surface

CHAPTER 6 NON-DESTRUCTIVE EVALUATION

6.1 Ultrasonic C-Scan

Ultrasonic inspection that can be performed on a large variety of materials is considered as the most effective NDE method for structural integrity examination. The principle of ultrasonic inspection is based on the reflected ultrasonic pulse generated by imperfections and discontinuities of test specimens. Ultrasonic C-Scan assists in evaluating the structural quality of materials providing two dimensional graphical representations. Therefore, after the impact tests, ABS specimens were C-Scanned utilizing an UltraPac II ultrasonic system (Mistras, Inc.) in our NDE laboratory. Two-dimensional time-of-flights (TOF) representation of damaged areas for the impacted ABS specimens were obtained from both impacted and non-impacted sides of the specimen by the use of ultrasonic C-Scan tool in our NDE laboratory shown in Fig 6.1.

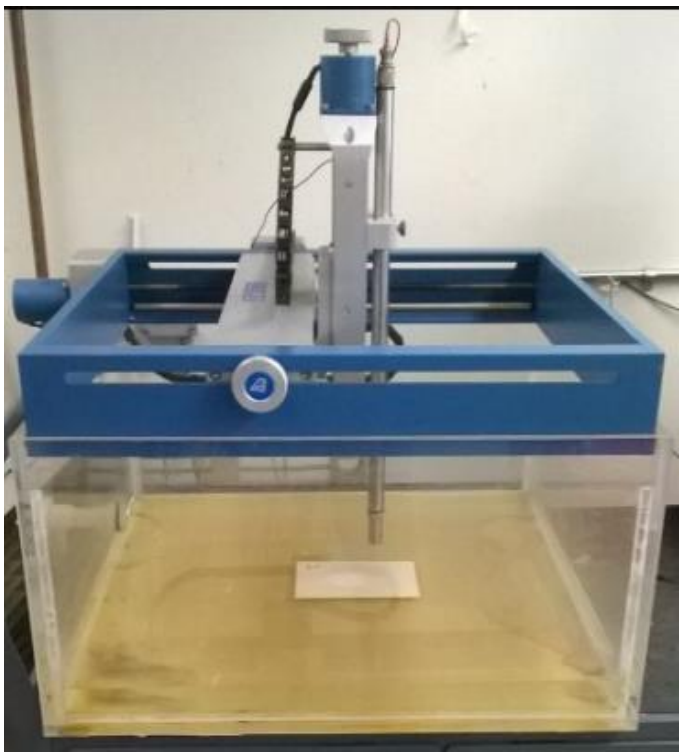

Fig 6.1. Ultrasonic C-Scan immersion tank

The detected damage areas in impacted ABS specimen at different impact energies are illustrated in the following figures.

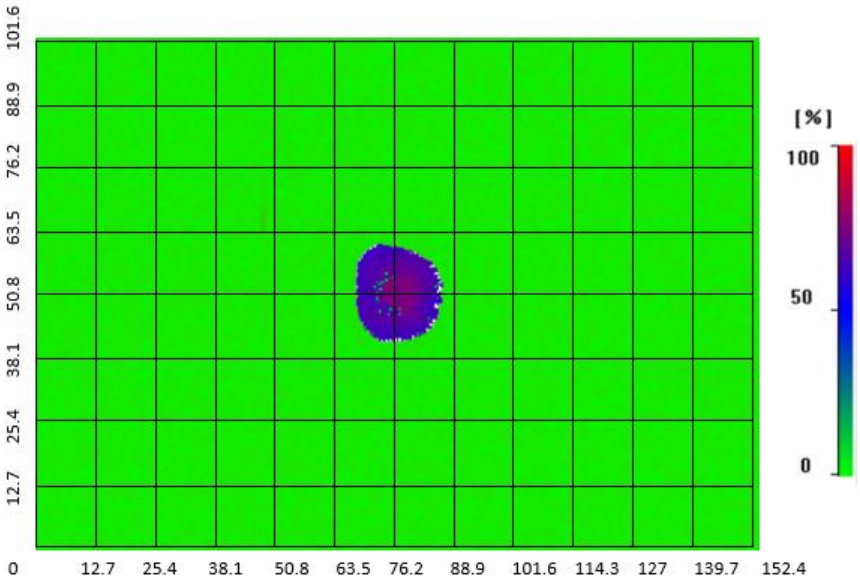

(a)

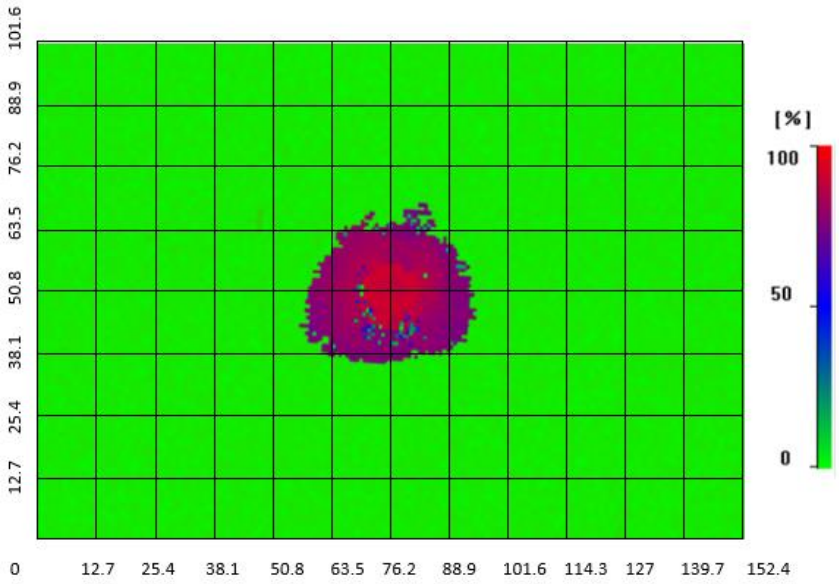

(b)

Fig 6.2. Detected damage area in ABS after impact (vel=4.43 m/s) , (a) Front surface ,(b) Back Surface

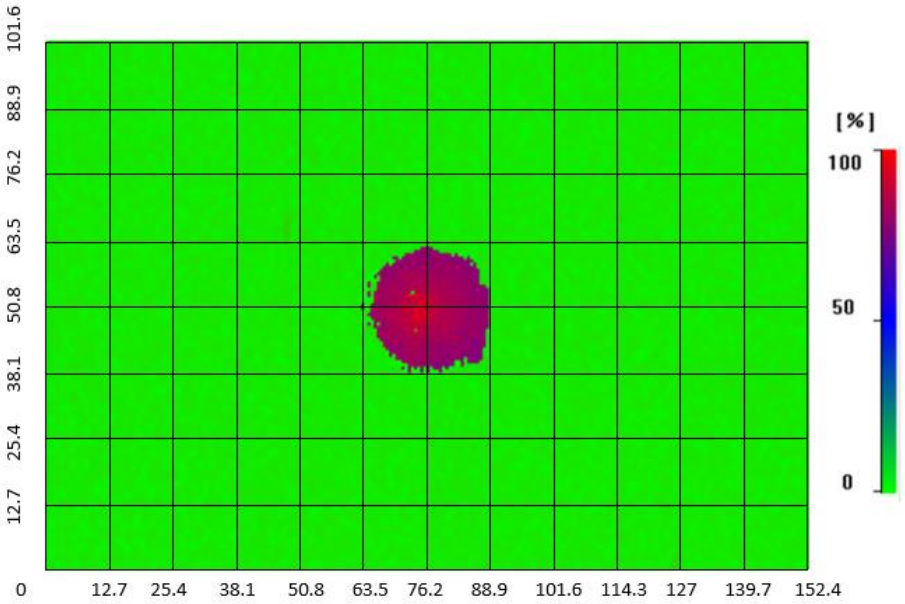

(a)

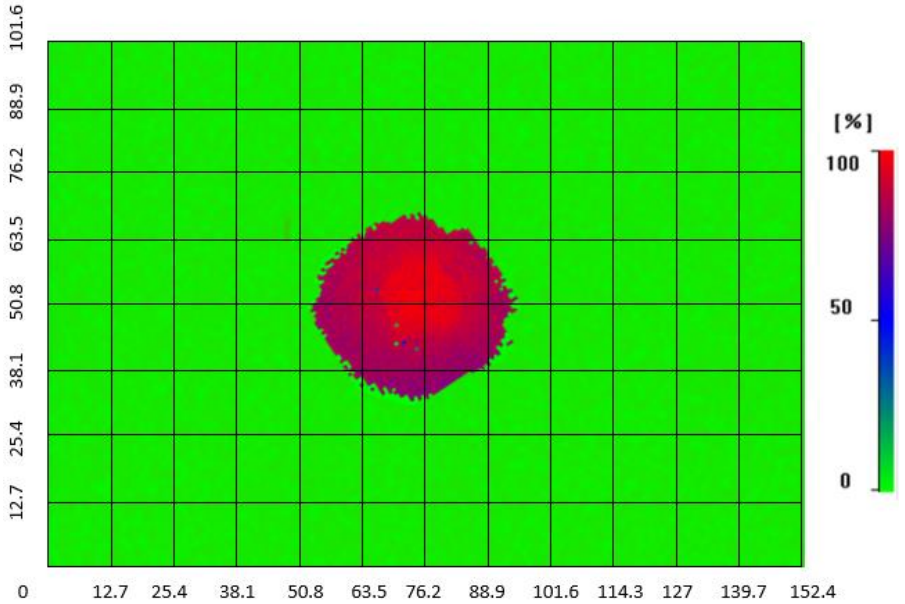

(b)

Fig 6.3. Detected damage area in ABS after impact (vel=5.775 m/s) , (a) Front surface ,(b) Back Surface

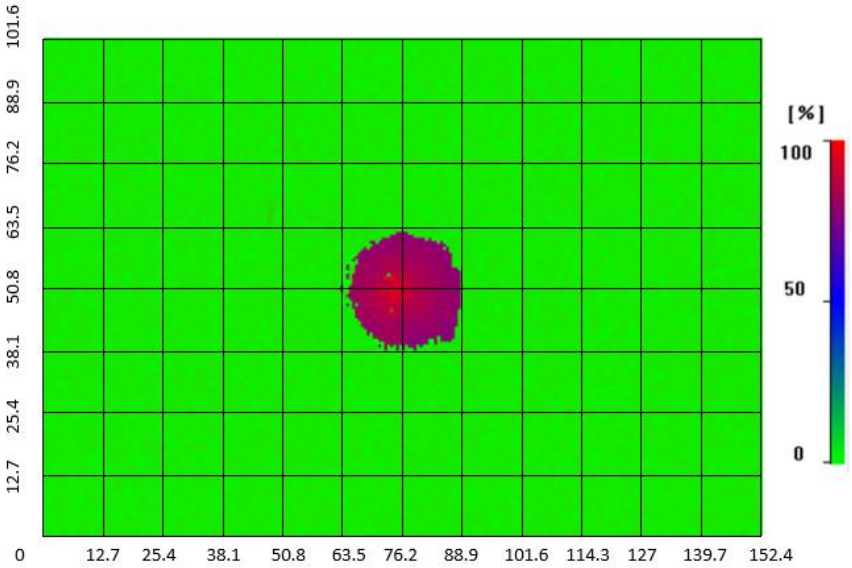

(a)

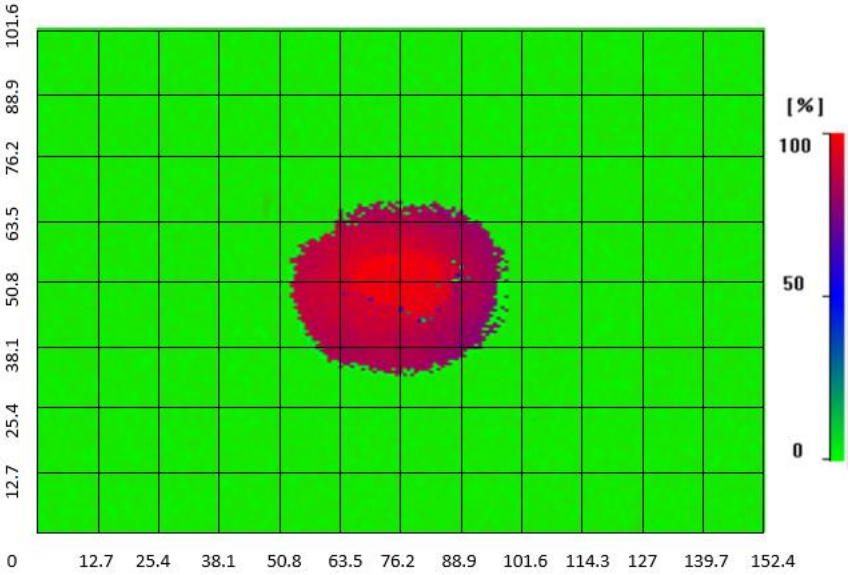

(b)

Fig 6.4. Detected damage area in ABS after impact (vel=6.264 m/s) , (a) Front surface ,(b) Back Surface

The measured damage areas are tabulated in Table 6.1 and compared to each other in Fig 6.5.

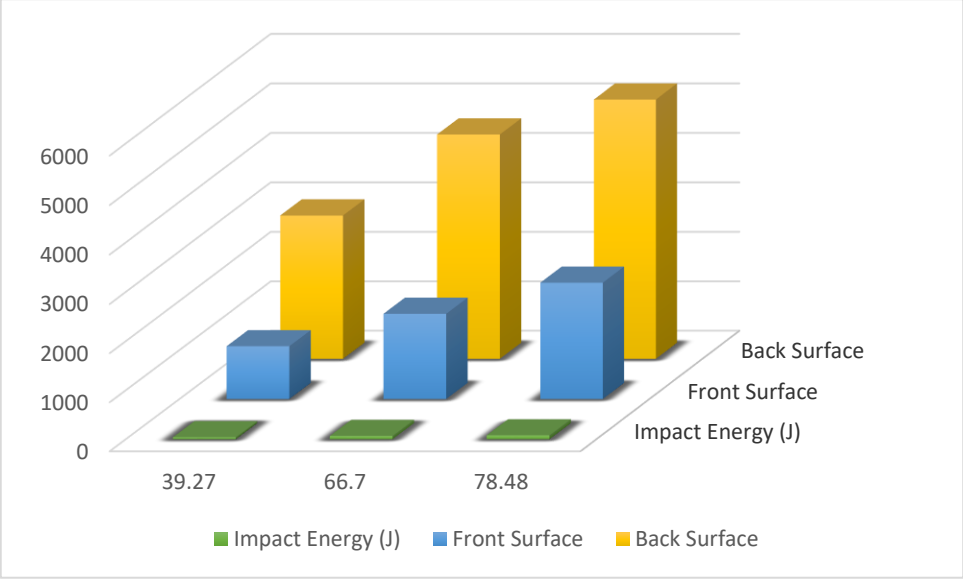

Fig 6.5. Comparisons of the damage areas detected by Ultrasonic C-Scan after impacts

Table 6.1. The measured damage areas from ultrasonic C-Scan after impact

	Damage Area (mm^2)	
Impact Velocity (m/s)	Front Surface	Back Surface
4.43	1076.42	2903.244
5.775	1735.7	4540.44
6.264	2364.58	5245.68

The following conclusions can be made based on the findings from ultrasonic C-Scan non-destructive evaluation method.

Increased impact energy produces a bigger damage area in both front and back surface of ABS. The damage area at the back surface is always much bigger in each impact energy level in comparison to front surface. As reported before, the compressive strength of ABS is always

higher than its tensile strength. During impact, while the front surface is under compression, the back surface is under tension. Due to the relatively lower strength of ABS in tension, its back surface under impact experiences much more severe damage and much bigger damage area. This finding agrees well with the prediction of numerical modelling of impact tests in regards to equivalent plastic strain in the back surface and front surface of ABS after impact.

Ultrasonic C-Scan detected localized damage at the back surface of ABS in each impact energy and this localized damage increases with an increase impact energy. After impact tests,color change at the back surface of ABS was observed in all impact energy levels that is the indication of localized material change produced by microvoids formation in amorphous thermoplastics. However,for more detailed evaluation,impacted and unimpacted surfaces of ABS needs to examined other NDE methods such as laser scanning microscopy. In the following section, the inspected surfaces of ABS by laser scanning microscopy will be presented.

6.2 Laser Scanning Microscopy

Laser scanning microscopy (LSM) has been widely used in an extensive range of applications because it possesses several advantages compared to other conventional microscopes. The major advantages of laser scanning microscopy are the capabilities to acquire serial parts from thick specimens and to control depth of field. In this work, a violet laser confocal microscope was utilized to scan specimen. Both the front and back surfaces of impacted ABS specimens were also examined with the confocal laser scanning microscope (Keyence, Inc.). Two-dimensional and three-dimensional surface representations of images were illustrated. Especially, three-dimensional images aided in examining the ABS surfaces thoroughly.

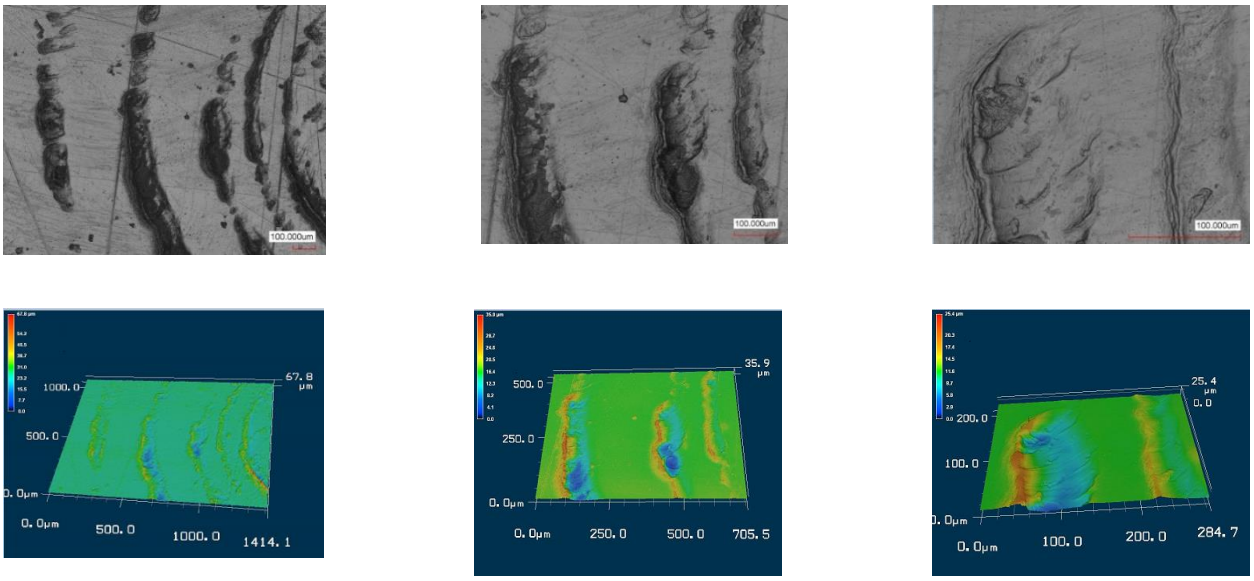

(a) (b) (c)

Fig 6.6. LSM examination of front surface of ABS after impact (vel=4.43 m/s), (a) magnification factor of 10, (b) magnification factor of 20, (c) magnification factor of 50

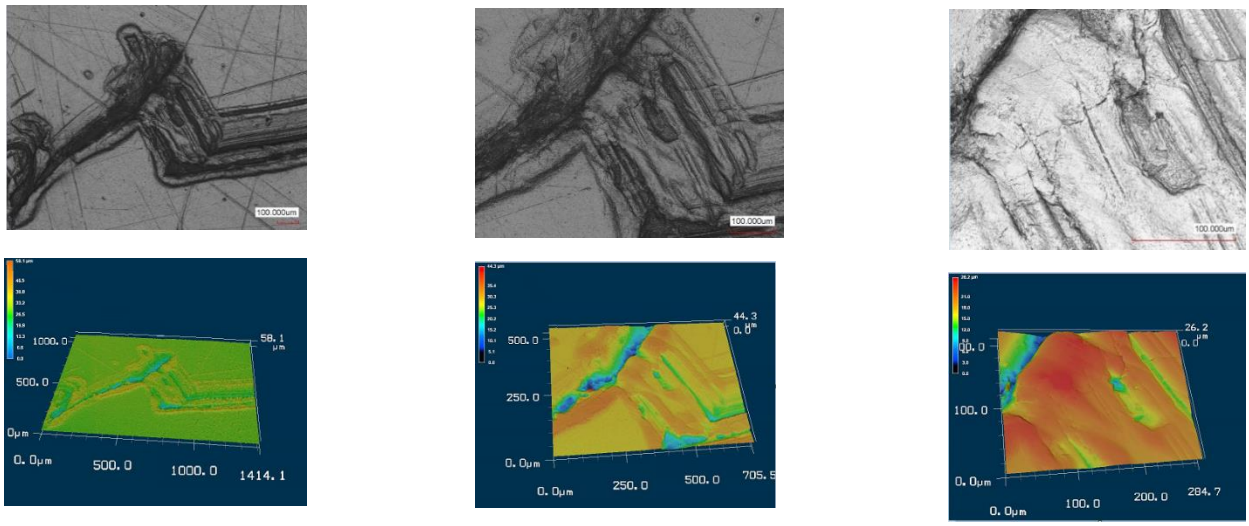

Fig 6.7. LSM examination of back surface of ABS after impact (vel=4.43 m/s), (a) magnification factor of 10, (b) magnification factor of 20, (c) magnification factor of 50

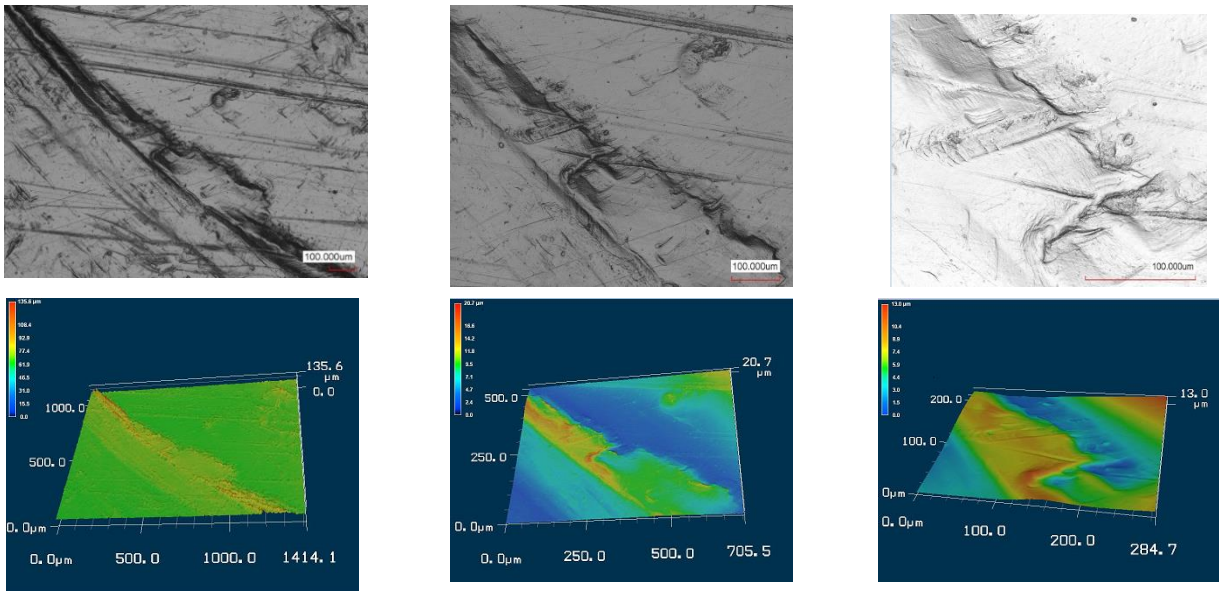

(a) (b) (c)

Fig 6.8. LSM examination of front surface of ABS after impact (vel=5.775 m/s), (a) magnification factor of 10, (b) magnification factor of 20, (c) magnification factor of 50

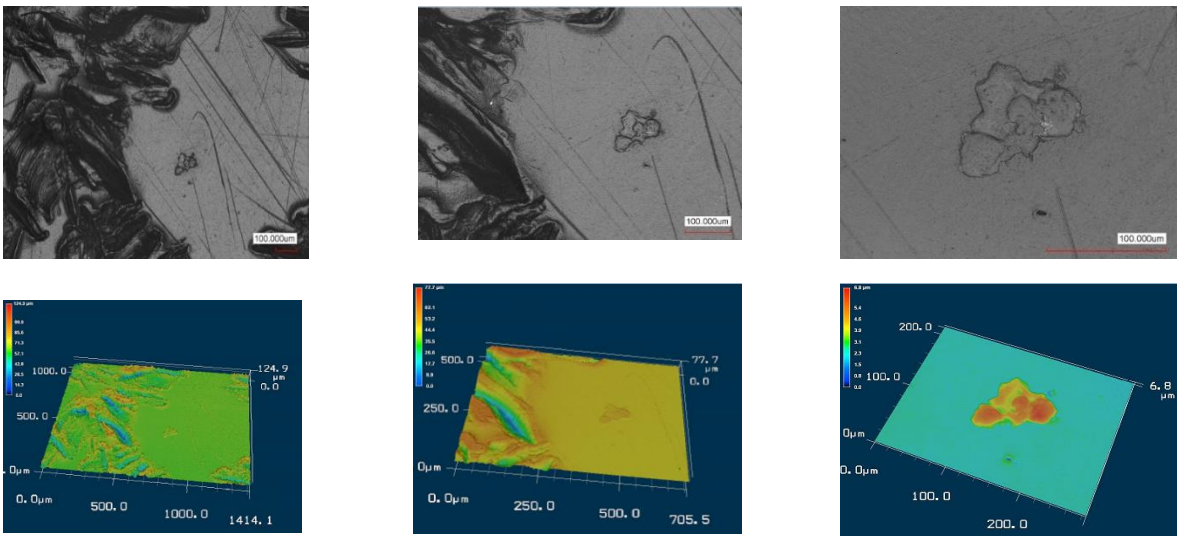

(a) (b) (c)

Fig 6.9. LSM examination of back surface of ABS after impact (vel=5.775 m/s), (a) magnification factor of 10, (b) magnification factor of 20, (c) magnification factor of 50

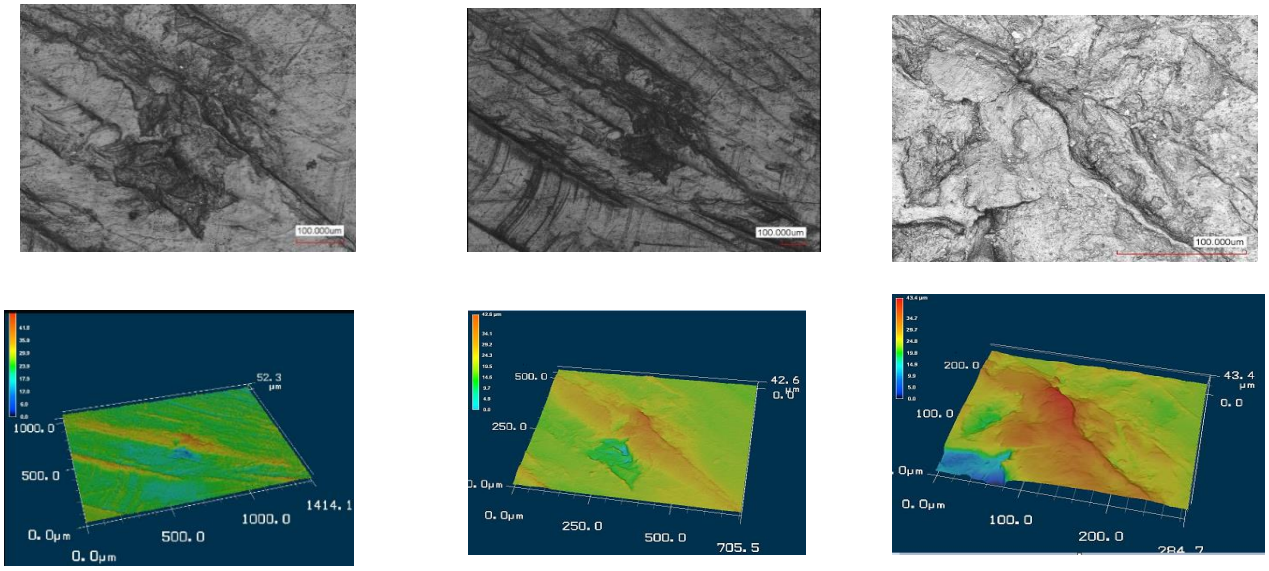

(a) (b) (c)

Fig 6.10. LSM examination of front surface of ABS after impact (vel=6.264 m/s),(a) magnification factor of 10, (b) magnification factor of 20, (c) magnification factor of 50

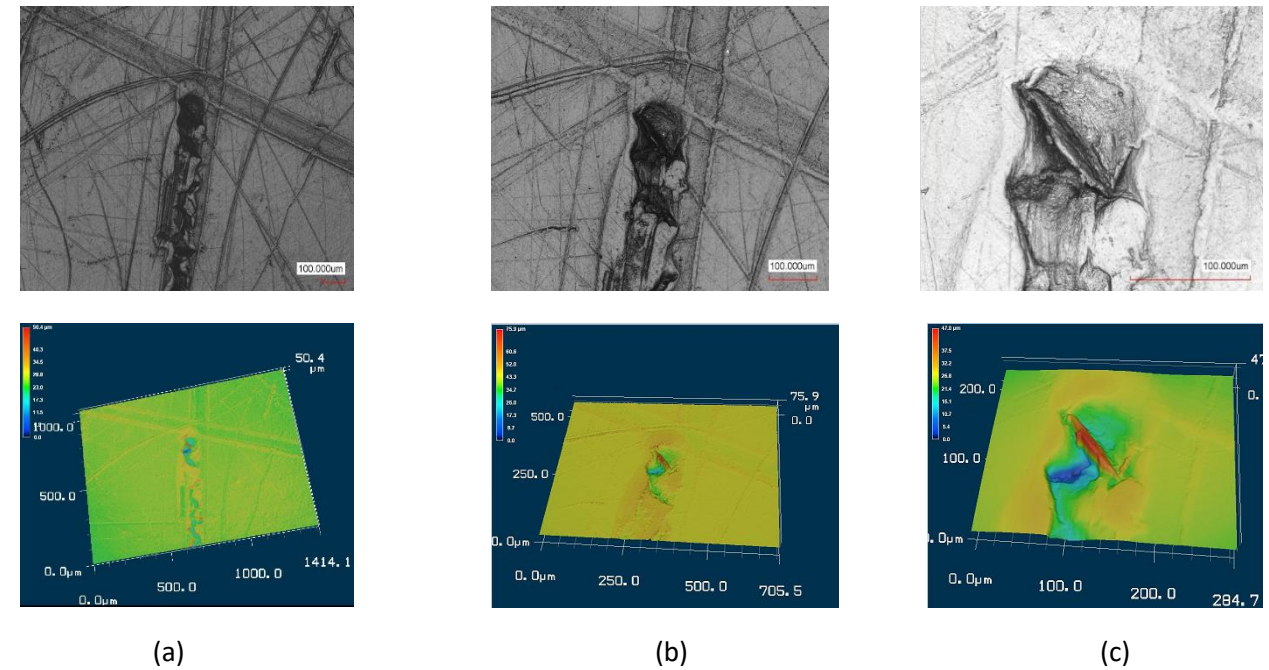

(a) (b) (c)

Fig 6.11. LSM examination of back surface of ABS after impact (vel=6.264 m/s), (a) magnification factor of 10, (b) magnification factor of 20, (c) magnification factor of 50

Both front and back surfaces of ABS after being subjected to three different impact energy were evaluated by the use of laser scanning microscopy with three various magnification

factors and the findings were displayed as two dimensional graphical representation and their corresponding 3 dimensional illustrations.

There was no severe damage sign such as surface crack, craze and microvoids observed at the impacted surfaces of ABS under all impact velocity levels. Nevertheless, a plastic deformation at the front surface of ABS caused by each impact energy was clearly detected by LSM but plastic deformation did not propogate to its further stage to result severe damage.

At the back surface of ABS subjected to impact velocity of 4.43 (m/s), craze formation was recognized as shown in Fig 6.7 and craze formation is the actual reason for damage in amorphous thermoplastics. The propagated damage state of crazes is microvoids formation but there was no microvoid detected for this impact energy level.

At the back surfaces of ABS subjected to 5.775 (m/s) and 6.264 (m/s) impact velocities, both crazes and microvoids were discovered as shown in Fig 6.9 and Fig 6.11, respectively. In contrast to impact velocity of 4.43 (m/s), crazes forced chain macromolecules to move their new positions and when they travel their new locations, microvoids were formed near rubber particles during travel.

The outcomes provided by laser scanning microscopy are in a good correlation with the findings obtained from ultrasonic inspection.

CHAPTER 7 EXPERIMENT vs. NUMERICAL RESULTS

7.1 Uniaxial Tension

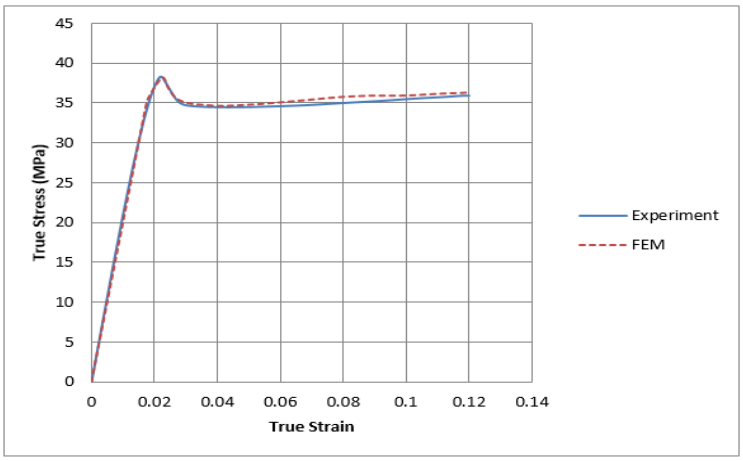

Fig 7.1. FEM vs Experiment, tensile true stress- strain curve of ABS at 0.0001 s^{-1}

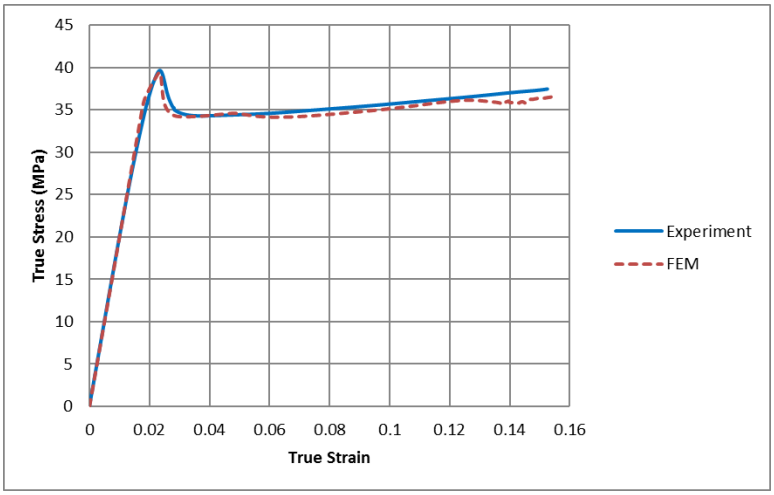

Fig 7.2. FEM vs Experiment, tensile true stress- strain curve of ABS at 0.001 s^{-1}

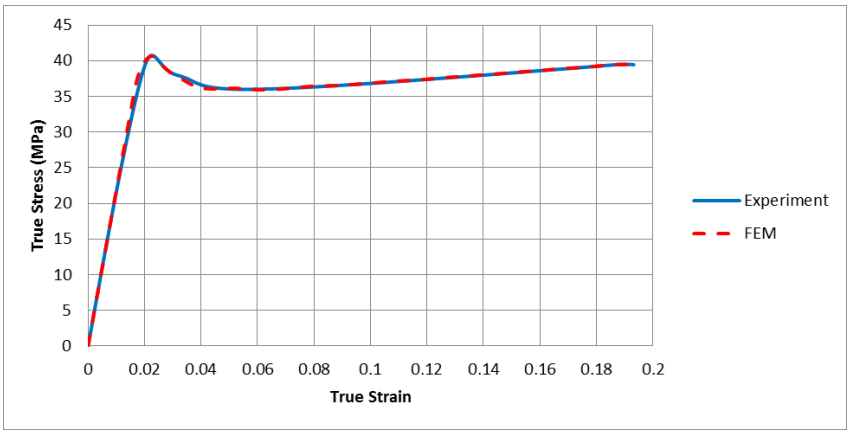

Fig 7.3. FEM vs Experiment, tensile true stress- strain curve of ABS at 0.02 s^{-1}

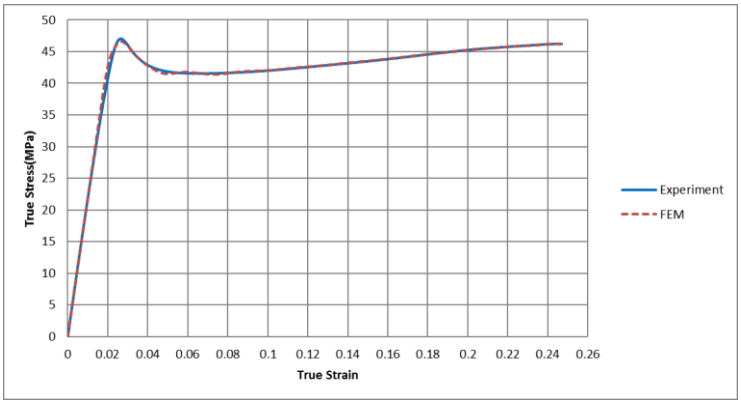

Fig 7.4. FEM vs Experiment, tensile true stress- strain curve of ABS at 0.1 s^{-1}

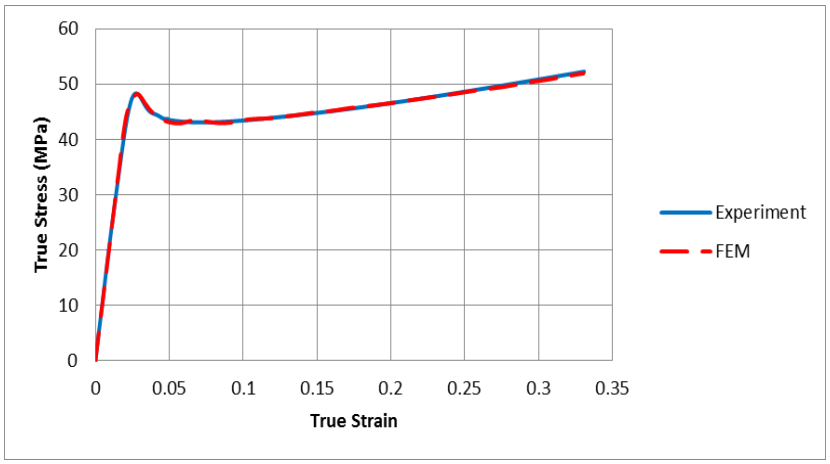

Fig 7.5. FEM vs Experiment, tensile true stress- strain curve of ABS at 0.2 s^{-1}

7.2 Uniaxial Compression

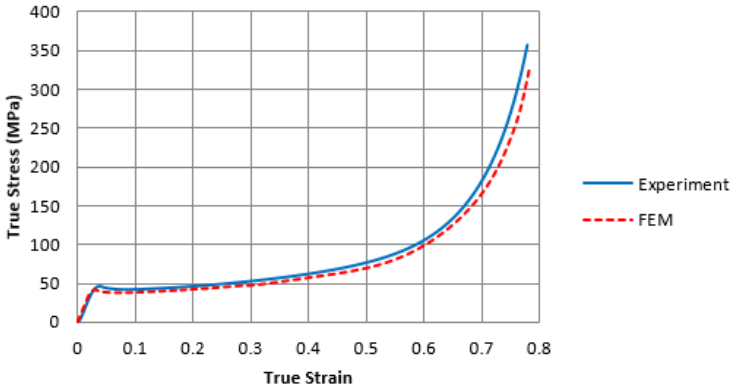

Fig 7.6. FEM vs Experiment, compressive true stress- strain curve of ABS at 0.0002 s^{-1}

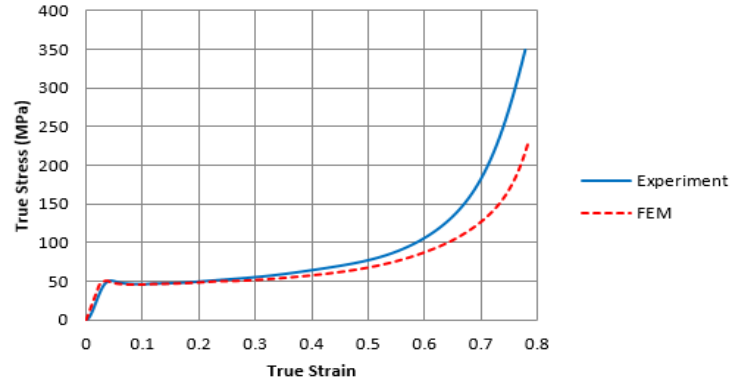

Fig 7.7. FEM vs Experiment, compressive true stress- strain curve of ABS at 0.002 s^{-1}

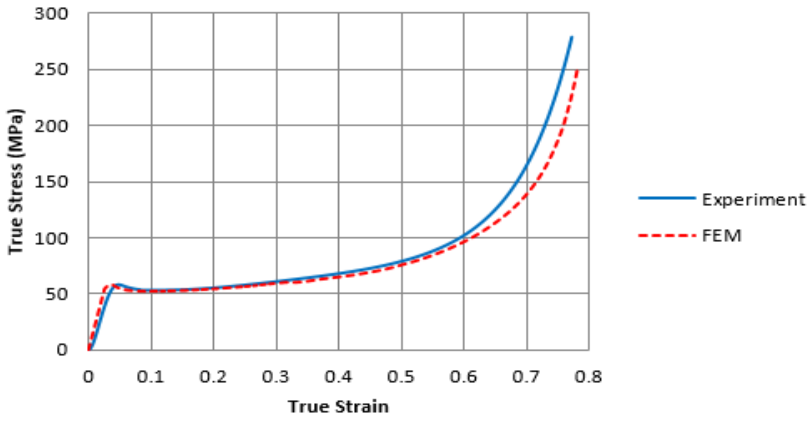

Fig 7.8. FEM vs Experiment, compressive true stress- strain curve of ABS at 0.04 s^{-1}

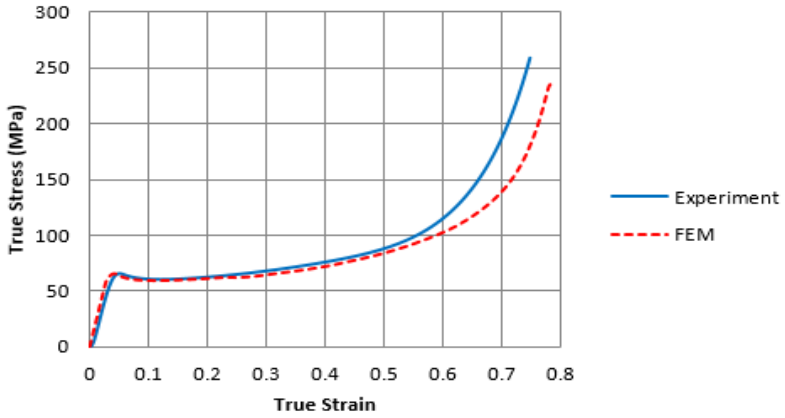

Fig 7.9. FEM vs Experiment, compressive true stress- strain curve of ABS at 0.2 s^{-1}

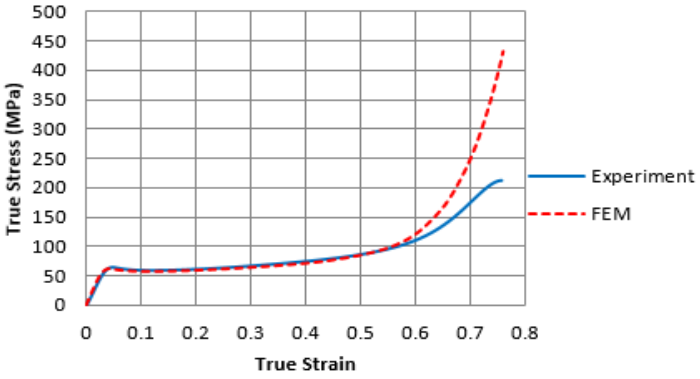

Fig 7.10. FEM vs Experiment, compressive true stress- strain curve of ABS at 0.4 s^{-1}

7.3 Three-Point Bending

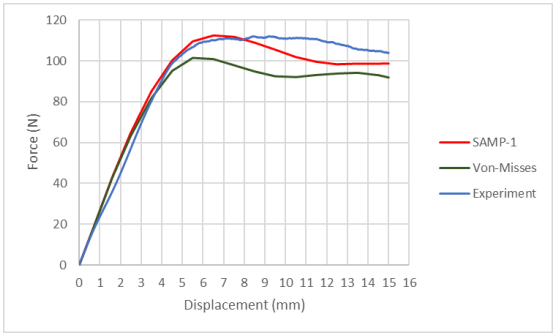

Fig 7.11. FEM vs Experiment, 3-point load-displacement curve at deformation rate of 0.005 (mm/s)

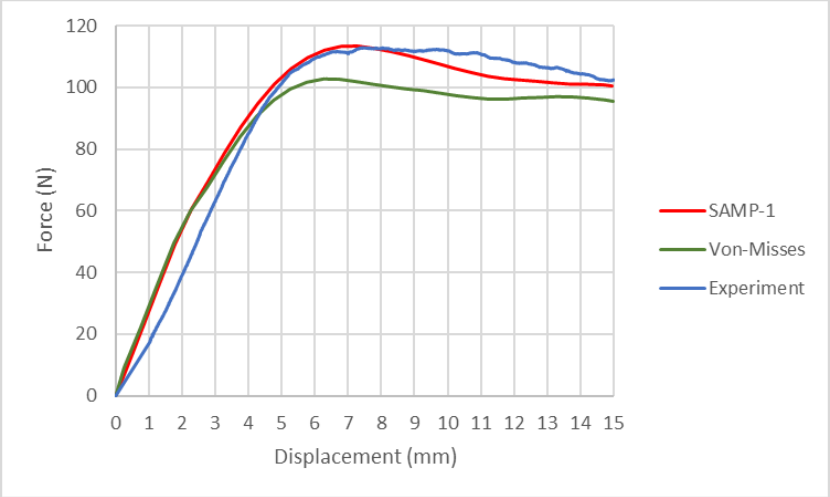

Fig 7.12. FEM vs Experiment, 3-point load-displacement curve at deformation rate of 0.05 (mm/s)

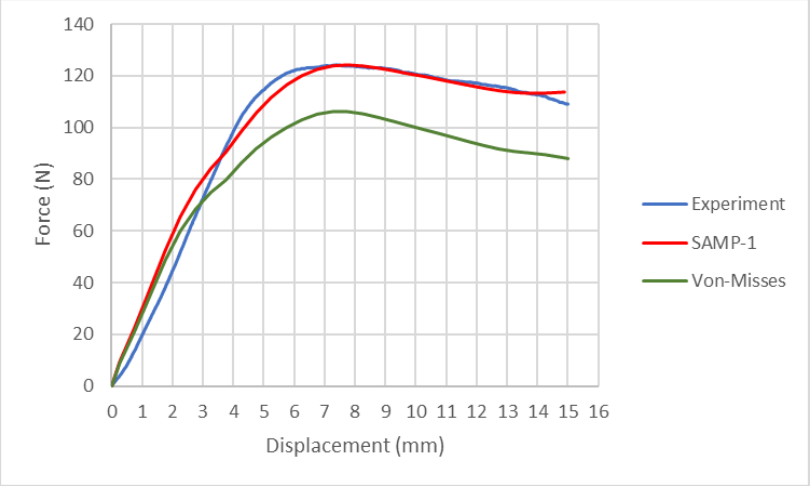

Fig 7.13. FEM vs Experiment, 3-point load-displacement curve at deformation rate of 1 (mm/s)

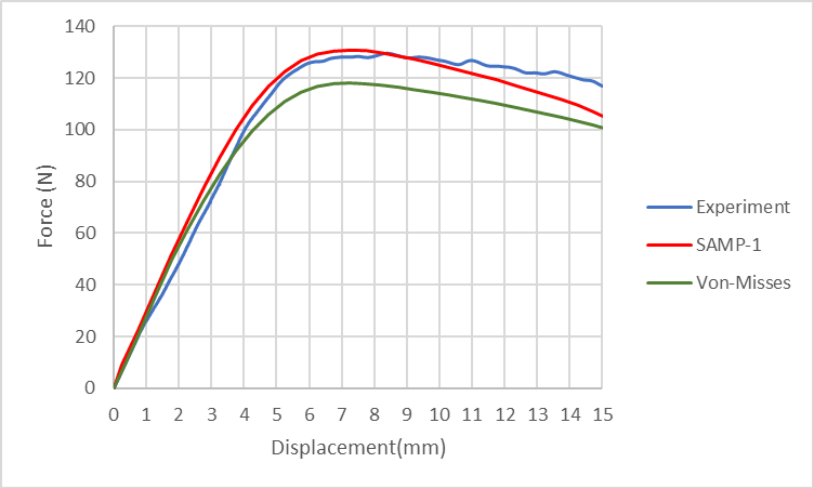

Fig 7.14. FEM vs Experiment, 3-point load-displacement curve at deformation rate of 5 (mm/s)

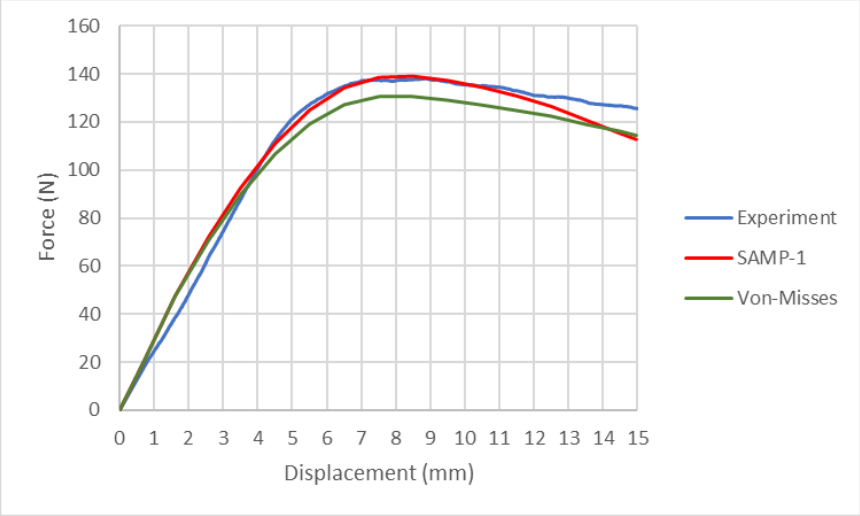

Fig 7.15. FEM vs Experiment, 3-point load-displacement curve at deformation rate of 10 (mm/s)

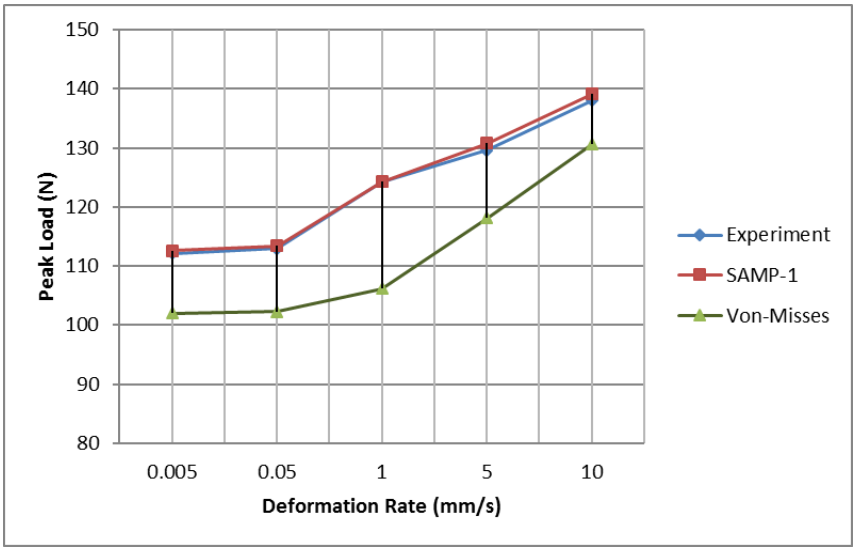

Fig 7.16. SAMP-1 vs Von-Misses in terms of Peak Loads under 3-point bending

7.4 Multiaxial Impact

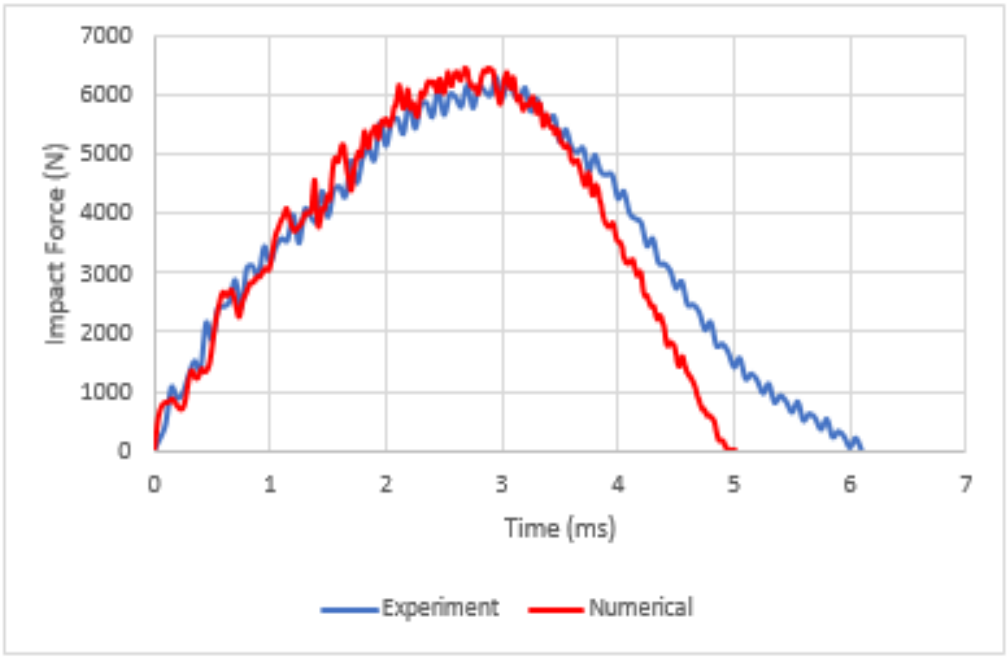

Fig 7.17. Comparisons of impact forces for impact velocity of 4.43 (m/s)

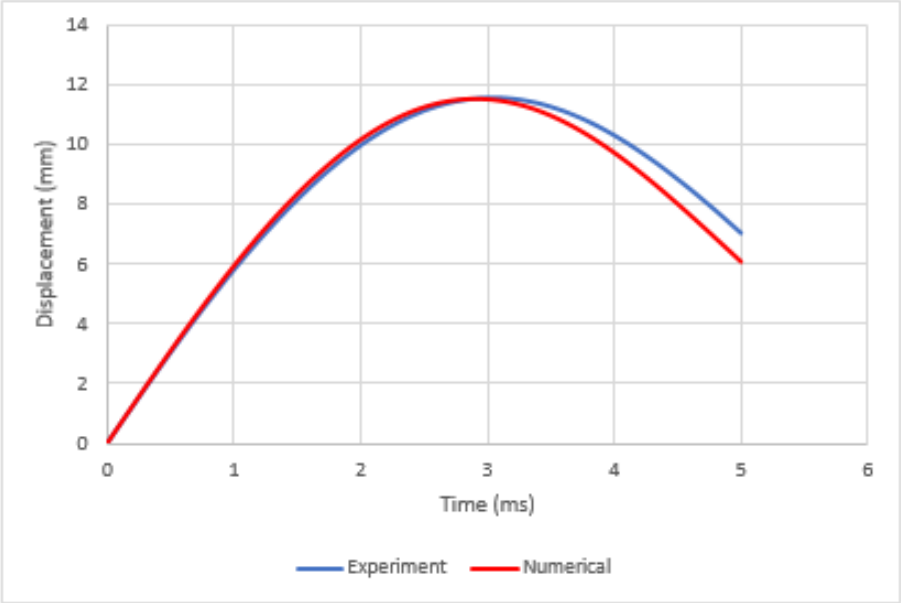

Fig 7.18. Comparisons of displacements for impact velocity of 4.43 (m/s)

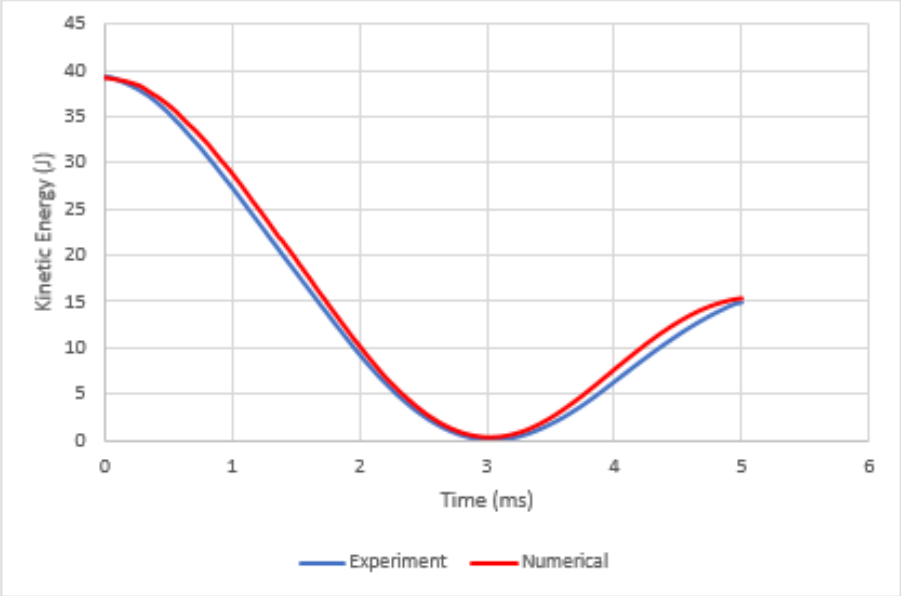

Fig 7.19. Comparisons of kinetic energies for impact velocity of 4.43 (m/s)

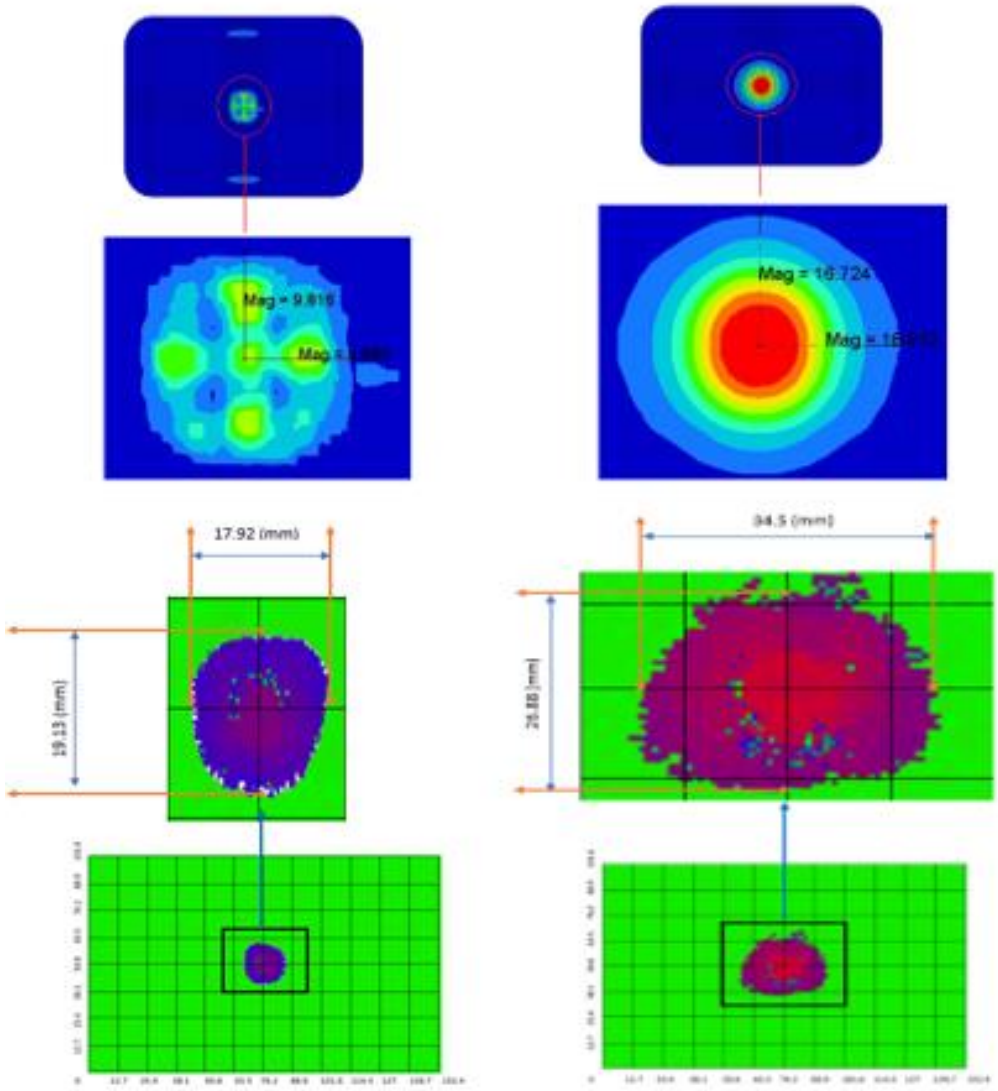

(a) (b)

Fig 7.20. Comparisons of damaged areas for impact velocity of 4.43 m/s ,(a) Front surface , (b) Back Surface

Table 7.1. Damaged area comparison for impact velocity of 4.43 (m/s)

	Damage Area (mm^2)	
	Front Surface	Back Surface
Ultrasonic C-Scan	1076.42	2903.244
FEM	304.67	888.55

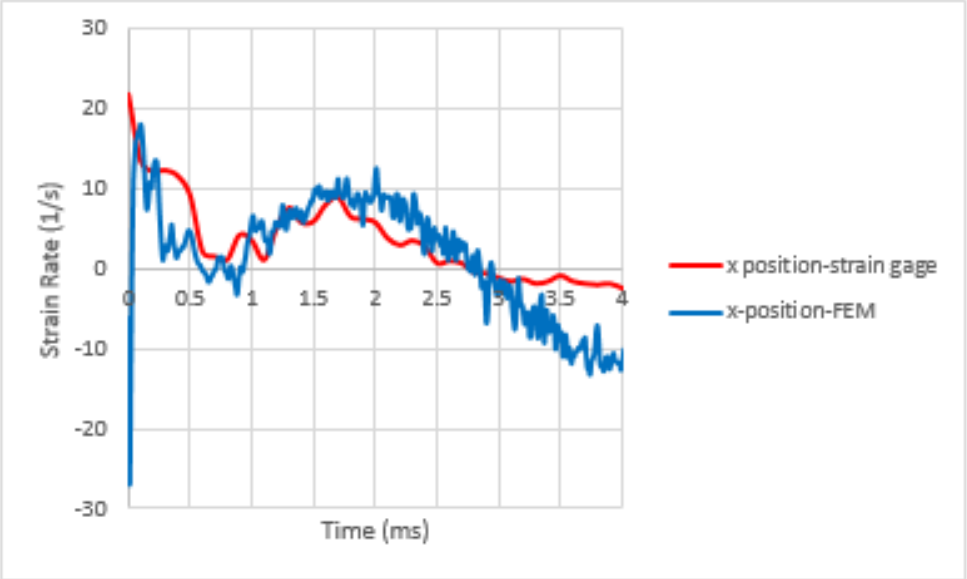

Fig 7.21. Comparisons of strain rates for impact velocity of 4.43 m/s

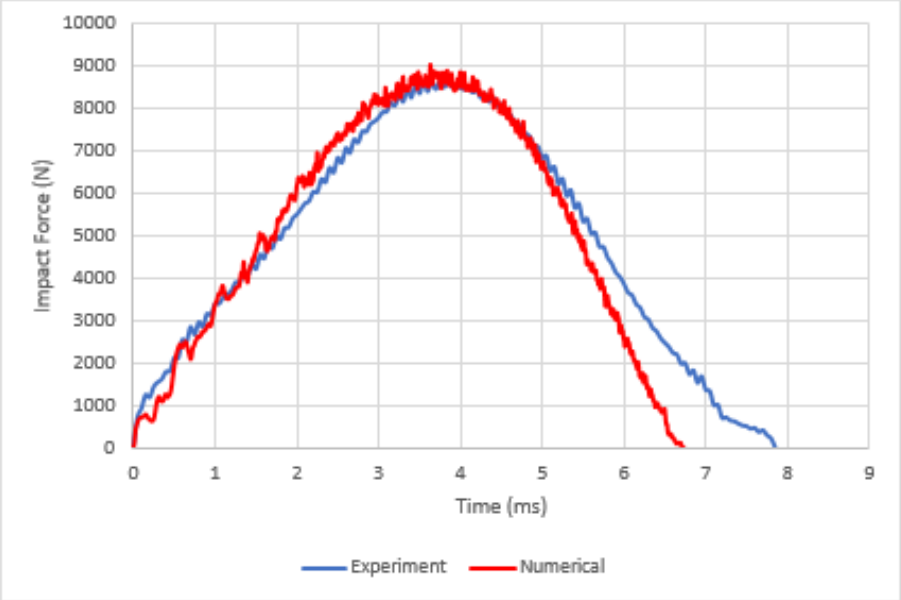

Fig 7.22. Comparisons of impact forces for impact velocity of 5.775 (m/s)

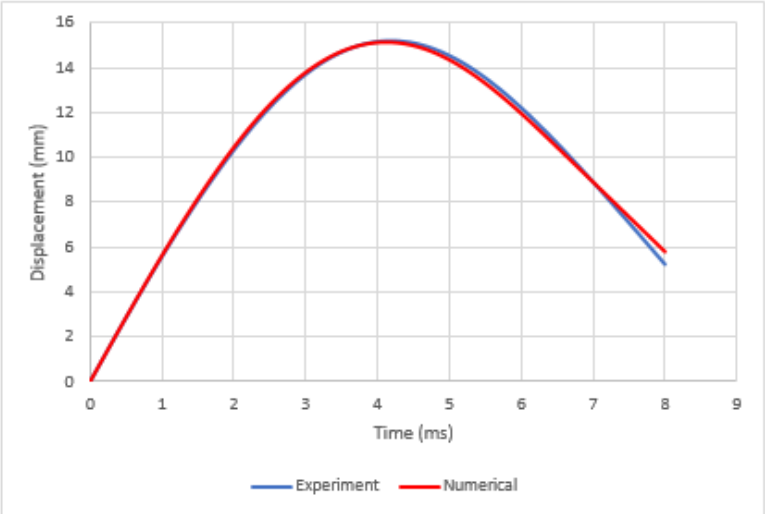

Fig 7.23. Comparisons of displacements for impact velocity of 5.775 (m/s)

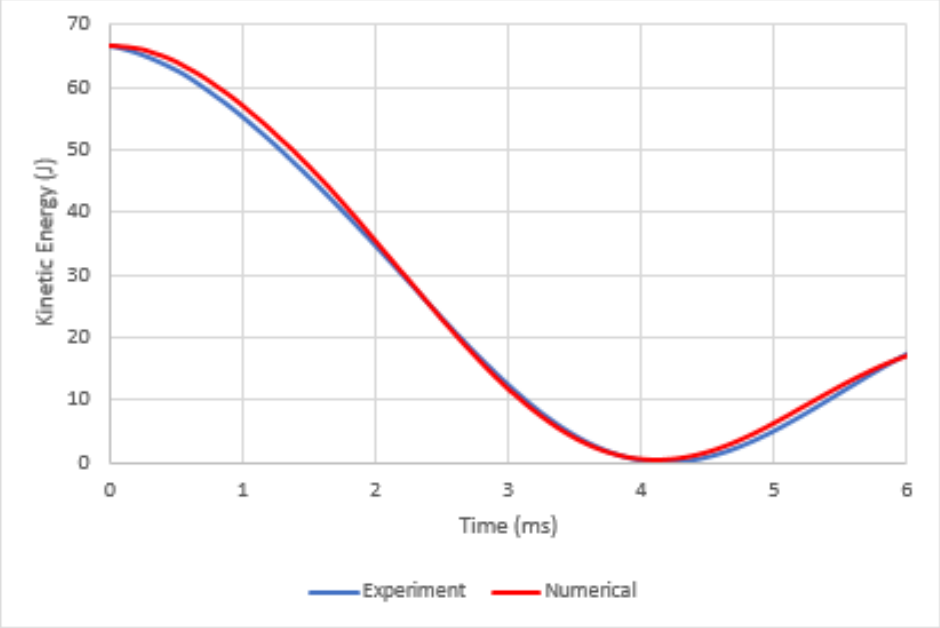

Fig 7.24. Comparisons of kinetic energies for impact velocity of 5.775 (m/s)

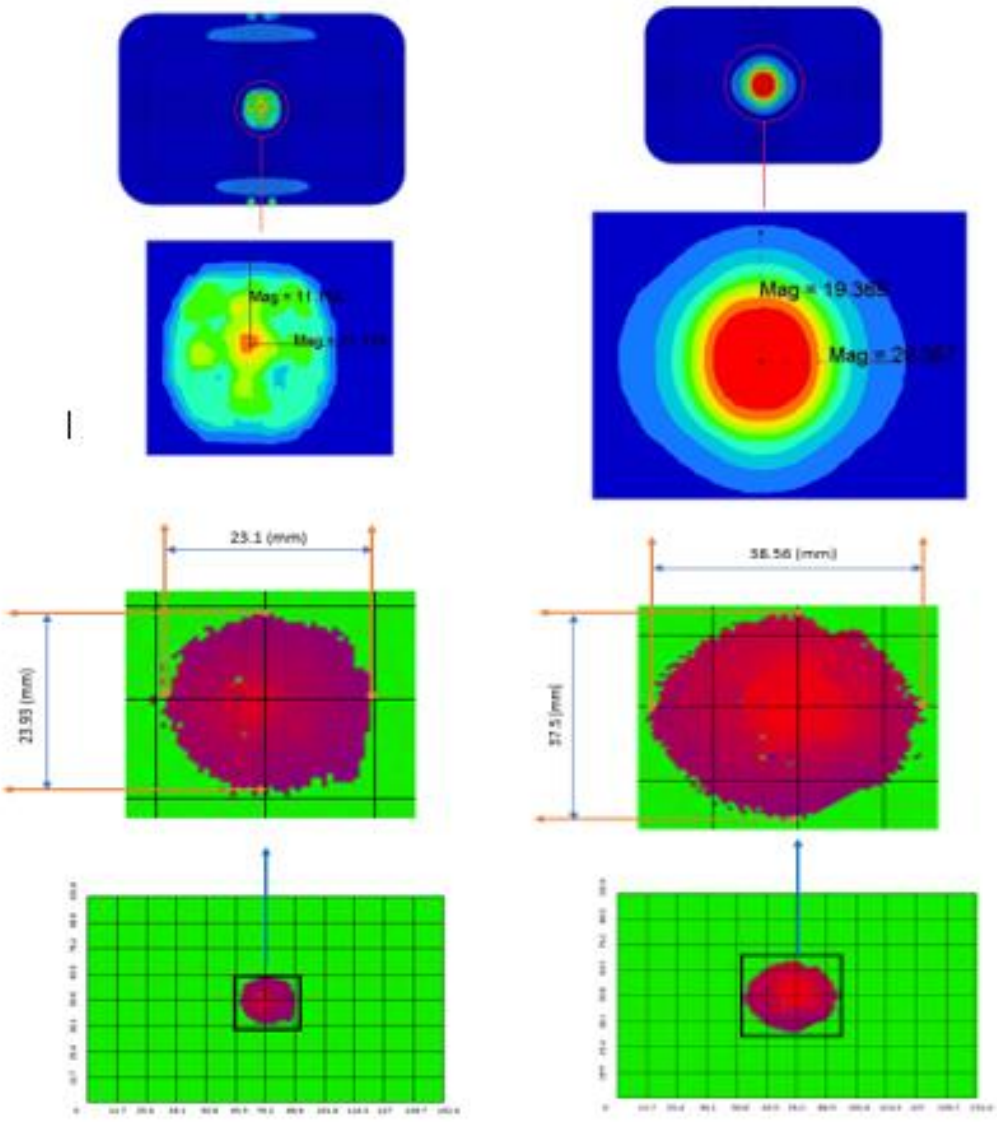

(a) (b)

Fig 7.25. Comparisons of damaged areas for impact velocity of 5.775 m/s ,(a) Front surface , (b) Back Surface

Table 7.2 Damage area comparison for impact velocity of 5.775 m/s

	Damage Area (mm^2)	
	Front Surface	Back Surface
Ultrasonic C-Scan	1735.7	4540.44
FEM	390.18	1238.71

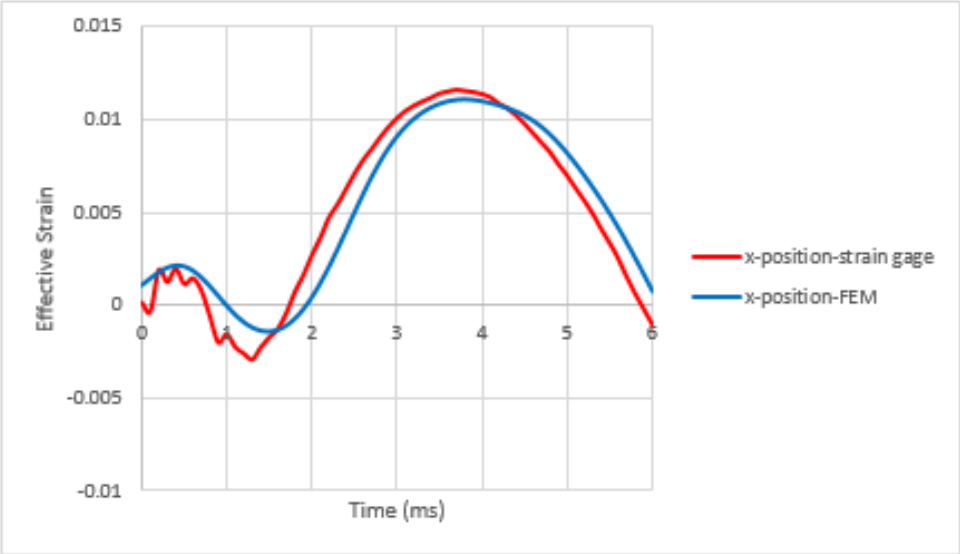

Fig 7.26. Comparisons of strains near impact area for impact velocity of 5.775 m/s ,(a) Front surface , (b) Back Surface

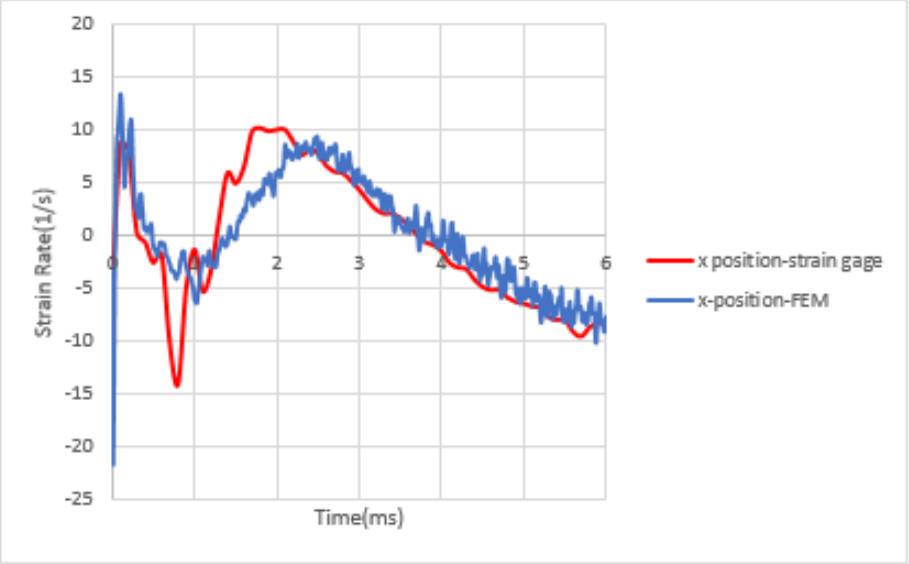

Fig 7.27. Comparisons of strain rates near impact area for impact velocity of 5.775 m/s ,(a) Front surface , (b) Back Surface

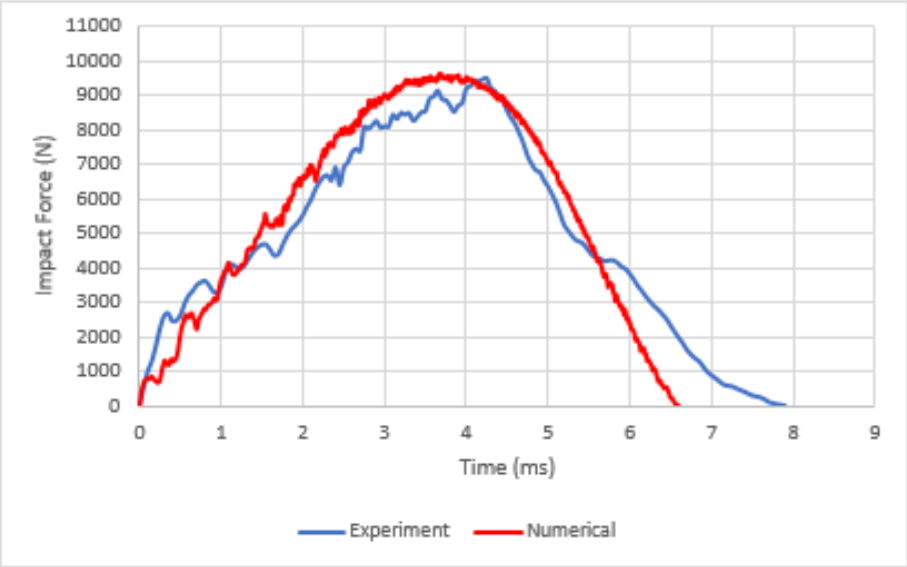

Fig 7.28. Comparisons of impact forces for impact velocity of 6.264 (m/s)

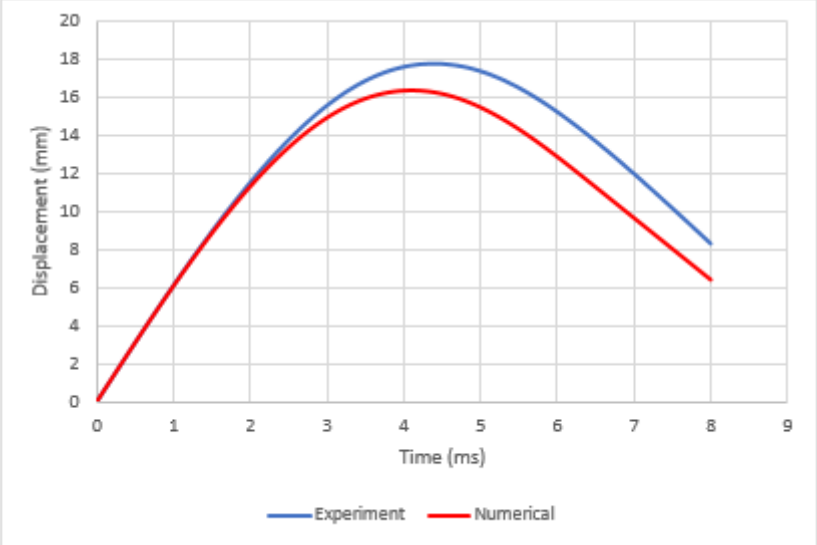

Fig 7.29. Comparisons of displacements for impact velocity of 6.264 (m/s)

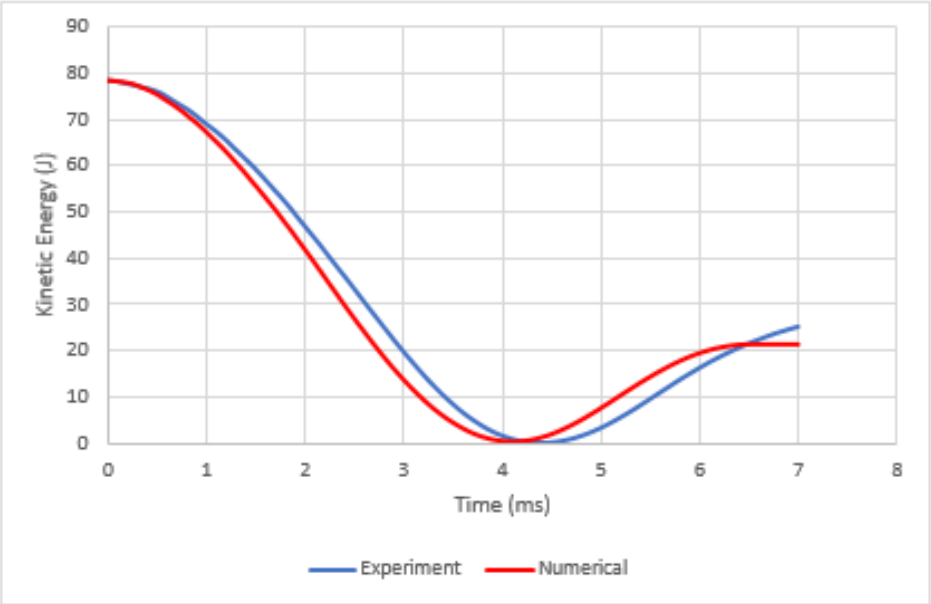

Fig 7.30. Comparisons of kinetic energies for impact velocity of 6.264 (m/s)

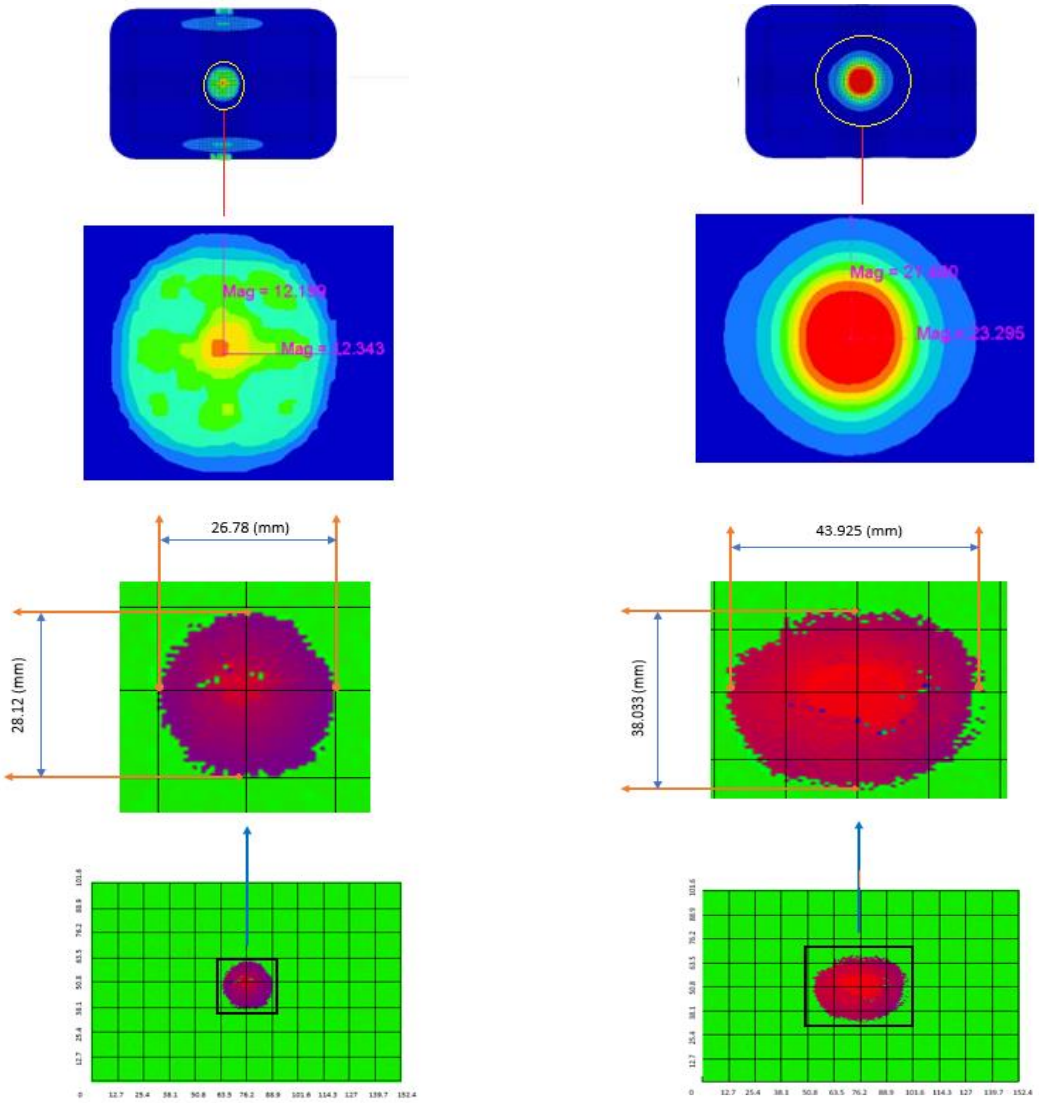

(a) (b)

Fig 7.31. Comparisons of damaged areas for impact velocity of 6.264 (m/s) ,(a) Front surface , (b) Back Surface

Table 7.3 Damage area comparison for impact velocity of 6.264 (m/s)

	Damage Area (mm^2)	
	Front Surface	Back Surface
Ultrasonic C-Scan	2364.58	5245.68
FEM	431.792	1571.97

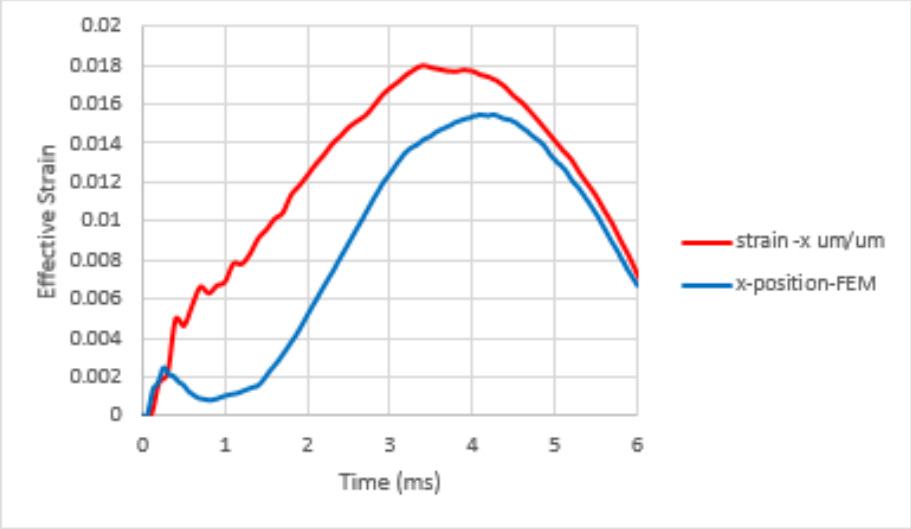

Fig 7.32. Comparisons of strains near impact area for impact velocity of 6.264 m/s ,(a) Front surface , (b) Back Surface

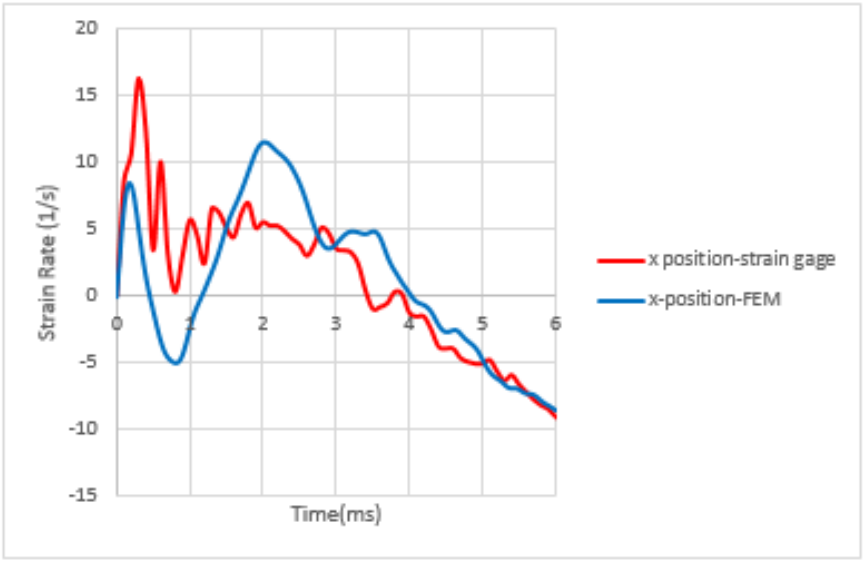

Fig 7.33. Comparisons of strain rates near impact area for impact velocity of 6.264 m/s ,(a) Front surface , (b) Back Surface

CHAPTER 8 IDENDIFICATION OF MATERIAL PARAMETERS OF ABS FOR CONSTITUTIVE MODEL

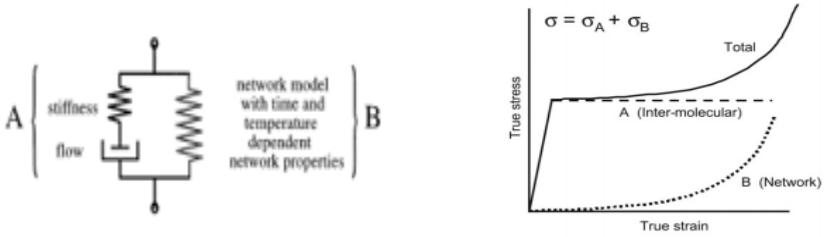

Fig 8.1. Boyce's Constitutive Model for Polymers[114]

As documented in literature review, Boyce decomposed the deformation mechanism of amorphous thermoplastics into two stages as intermolecular (Part A) and network resistance (Part B) shown in Fig 8.1. Her constitutive material model uses 9 distinct coefficients, if the bulk modulus (κ) in eq (1.13) is neglected. While 7 coefficients are related to Part A, the remaining two is associated with Part B. Our purpose here is to define all coefficients for ABS.

Part A uses two elastic parameters, including initial elastic moduli (E) and Poisson's ratio (υ_0) see eq.1.12 and three plastic parameters, such as uniaxial tensile strength (σ_T), uniaxial compressive strength (σ_C) and β isochoric plastic flow (constant volume) or non-isochoric flow (volume change) see eq (1.9). The relationship between σ_T and σ_C can be expressed as $\alpha = \sigma_C / \sigma_T$ that represents the pressure sensitivity factor for yield surface. Two rate sensitivity parameters $\dot{\gamma}_A^p \; and \; \dot{\gamma}_0^A$ can be obtained from eq (1.1).

Elastic moduli (E) and Poisson's ratio for ABS can readily be specified from uniaxial true stress-strain curve for the lowest strain rate of 0.0001 s^{-1} from Fig 4.3 and reported as E=1826 MPa and υ_0=0.38, respectively.

Pressure sensitivity factor ($\alpha = \sigma_C / \sigma_T$) for ABS was provided as 1.204 and 1.315 for two identical strain rates of quasi-static and 0.2 s^{-1}, respectively. If these two ratios are averaged, the pressure sensitivity factor(α) for ABS is calculated as 1.255.

Identification of Strain Rate Sensitive Parameter (C):

In the actual constitutive model, strain rate sensitivity factor is defined based on Argon's thermally activated process approach in terms of shear yield stress as a function of shear strain rate ($\dot{\gamma}_A^p$) and pre-exponential factor($\dot{\gamma}_0^A$) as expressed in eq (4.1) [114, 115]. For the definitions of other parameters in the eq (4.1), see eq (1.1), eq (1.3) and eq (1.11).

$$\dot{\gamma}_A^p = \dot{\gamma}_0^A \, exp\left[-\frac{\Delta G(1-\tau A/s)}{k\theta}\right] \tag{8.1}$$

Rather than defining strain rate sensitive parameter for ABS in terms of shear strain rate, we will characterize it in terms of equivalent plastic strain rate ($\dot{\bar{\varepsilon}}^p$) and reference strain rate ($\dot{\varepsilon}_{O_A}$) under tension incorporating the well known Raghava's pressure dependent yield surface definition for polymers[116, 117]. Raghava's pressure dependent yield surface definition can be expressed as:

$$\bar{\sigma}_A = \frac{(\alpha-1)I_{1A} + \sqrt{(\alpha-1)^2 I_{1A}^2 + 12\alpha J_{2A}}}{2\alpha} \tag{8.2}$$

where $\tilde{\sigma}_A$ is the equivalent yield stress, I_{1A} and J_{2A} are stress invariants and $\alpha = \sigma_C / \sigma_T = 1.255$ for ABS.

In terms of principle stresses, the stress invariants (I_{1A} and J_{2A}) can also be written as shown below:

$$I_{1A} = \sigma_1 + \sigma_2 + \sigma_3 \tag{8.3}$$

and

$$J_{2A} = \frac{1}{6}((\sigma_1 - \sigma_2)^2 + (\sigma_1 - \sigma_3)^2 + (\sigma_2 - \sigma_3)^2) \tag{8.4}$$

If we consider the Raghava's definition for only uniaxial tension case, both σ_2 and σ_3 are equal to 0 and $\sigma_1 = \sigma_x$. Based on this, when the stress invariants are calculated and substituted in eq (8.2), we will see that $\tilde{\sigma}_A$ gives whatever yield stress under tension; therefore, the yield surface expression can simply be written as below:

$$f_A = \tilde{\sigma}_A - \sigma_T = 0 \tag{8.5}$$

where σ_T is yield stress under tension.

Furthermore, eq (8.1) can be written in terms of $\tilde{\sigma}_A$, $\dot{\bar{\varepsilon}}^p$ and $\dot{\varepsilon}_{O_A}$ with the following expression.

$$\dot{\bar{\varepsilon}}^p = \dot{\varepsilon}_{O_A} \, exp\left[\frac{1}{C(\theta)}\left(\frac{\tilde{\sigma}_A}{\sigma_T} - 1\right)\right] \tag{8.6}$$

Moreover, after simple re-arrangement of the eq (8.6), the same expression can also be formulated as:

$$\frac{\tilde{\sigma}_A}{\sigma_T} = 1 + C \, ln\left(\frac{\dot{\bar{\varepsilon}}^p}{\dot{\varepsilon}_{O_A}}\right) \tag{8.7}$$

Here, C represents the strain rate sensitivity parameter and as documented earlier, $\dot{\bar{\varepsilon}}^p$ is the tensile plastic strain rate and $\dot{\varepsilon}_{O_A}$ is the reference strain rate (generally lowest strain rate or quasi static).

We will obtain the strain rate sensitivity parameter (C) for ABS depending on our tension test data as a function of strain rates. In our calculations, we are going to use nominal tensile yield stresses of ABS as a function of strain rates as indicated in Fig 8.2.

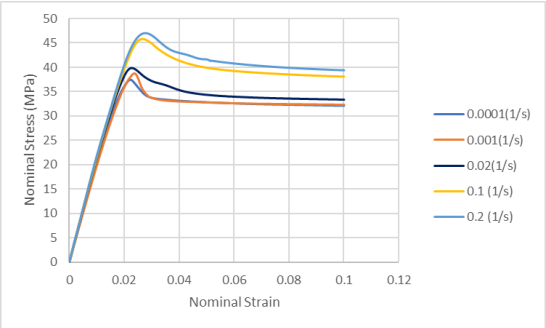

Fig 8.2. Nominal tensile stress-strain curves for ABS under different strain rates

Among the attained strain rates during uniaxial tension tests, the lowest one is 0.0001 s^{-1} that is taken as our reference strain rate ($\dot{\varepsilon}_{O_A}$=0.0001 s^{-1}) and corresponding tensile nominal upper yield stress of ABS for this strain rate is 34.72 MPa considered as σ_T=34.72 MPa. We preferred to use tensile nominal upper yield stresses of ABS under different strain rates. Note that σT is also our reference tensile nominal upper yield stress of ABS only used in the calculations of C. After calculations, the initial strain rate sensitivity parameter (C) for ABS was derived as 0.0361 as shown in Fig 8.3.

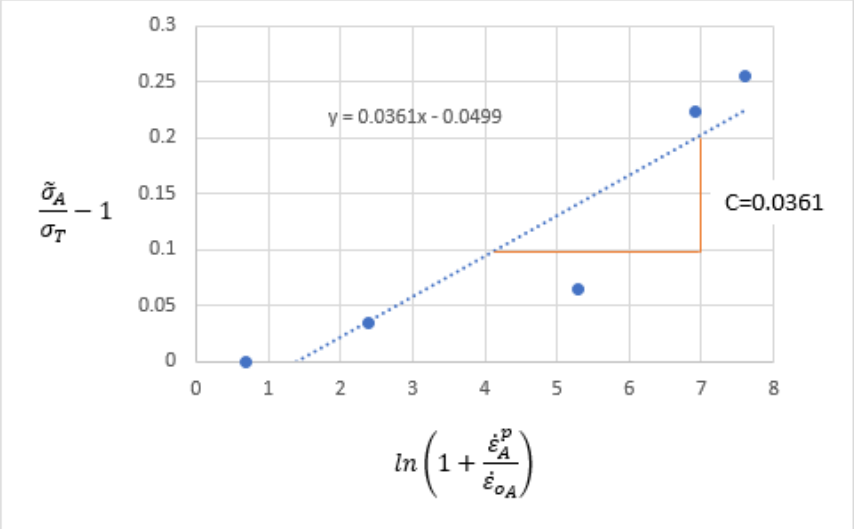

Fig 8.3. Strain rate sensitivity factor (C) for ABS

In the calculation of C parameter for ABS, we used tensile nominal yield stresses; however, Raghava's yield surface definition uses true stresses. Therefore, the obtained C value of 0.0361 was taken as our initial value and used for iterative solutions. After several iterations, the optimum value of C for ABS was derived as equal to 0.0359. Hence, the complete and final definition for strain rate dependent true upper yield stress of ABS under uniaxial tension as a function of strain rate can be given as:

$$\tilde{\sigma}_A = 38.273\left(1 + 0.0359\, ln\left(\frac{\dot{\varepsilon}^p}{0.0001}\right)\right) \tag{8.8}$$

Thus, based on only uniaxial tension test data under different strain rates, $\tilde{\sigma}_A$ is calculated to obtain C parameter for ABS certainly implying that $\tilde{\sigma}_A$ predicts the tensile true upper yield stress of ABS as a function of strain rate. Therefore, we firstly are going to compare the prediction with our experimental results for uniaxial tension.

Table 8.1. Experiment vs Material Model for Tensile True Upper Yield Stresses of ABS as a function of Strain Rates.

Log Strain Rate (s^{-1})	**Upper Yield Stress(MPa)-Experiment**	**Upper Yield Stress(MPa)-Material Model**
-4	38.273	38.273
-3	39.658	41.43675353
-1.698970004	40.76	45.55289177
-1	47.046	47.76426059
-0.698970004	48.322	48.7166453
1	53.51	54.09176765
1.477121255	54.62	55.6012617
1.653212514	55.93	56.15837104

The comparison of experimental tensile true upper yield stresses of ABS as a function of strain rates with the material model predictions are documented in Table 8.1 and plotted in Fig 8.4.

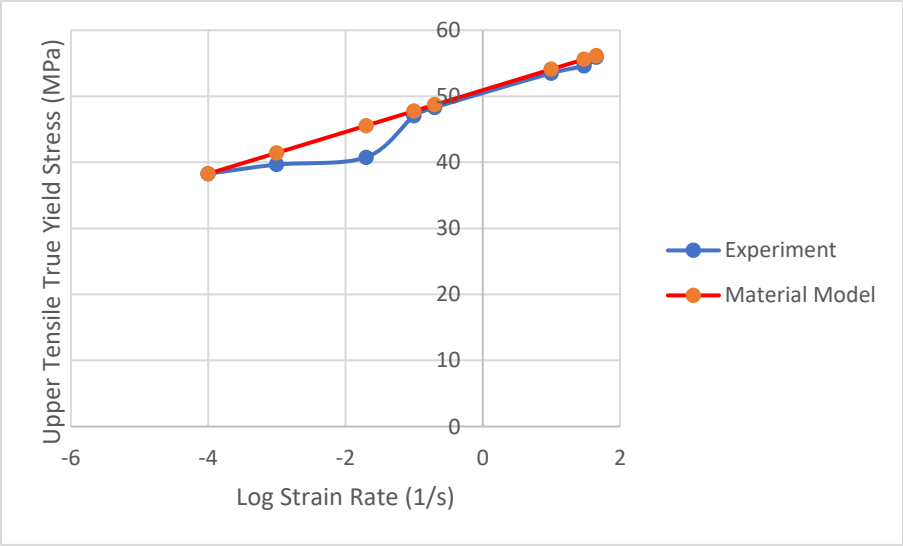

Fig 8.4. Experiment vs Material Model for Tensile True Upper Yield Stresses of ABS as a function of Strain Rates

Moreover, through the relationship ($\alpha = \sigma_C / \sigma_T = 1.255$), compressive true upper yield stresses of ABS for different strain rates attained in uniaxial compression tests were predicted and compared to experimental results as tabulated in Table 8.2 and plotted in Fig 8.5.

Table 8.2. Experiment vs Material Model for Compressive True Upper Yield Stresses of ABS as a function of Strain Rates.

Log Strain Rate (s^{-1})	**Upper Yield Stress(MPa)-Experiment**	**Upper Yield Stress(MPa)-Material Model**
-3.698970004	46.1	49.22785781
-2.698970004	50.83	53.19836849
-1.397940009	58.175	58.36412198
-0.698970004	63.56	61.13938985
-0.397940009	65.63	62.33463266

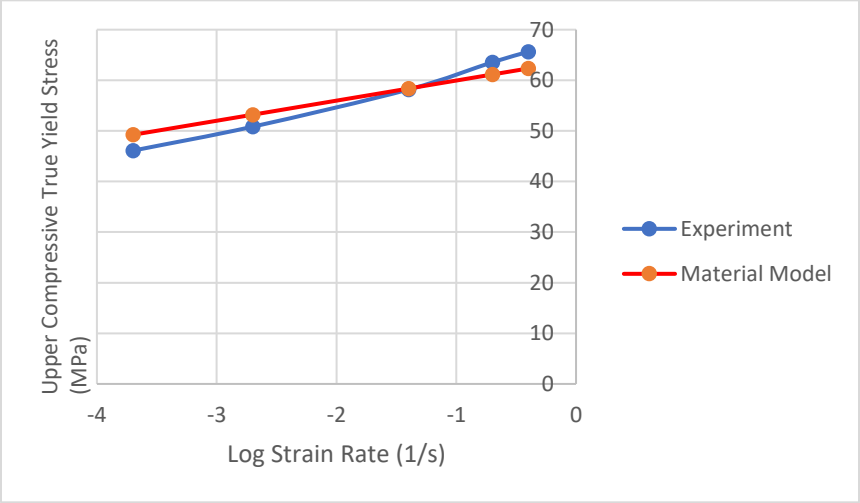

Fig 8.5. Experiment vs Material Model for Compressive True Upper Yield Stresses of ABS as a function of Strain Rates

From the comparisons above, the following conclusions can be made as put in order:

The determined strain rate sensitivity parameter (C) predicts the tensile upper yield stresses of ABS insignificantly higher than the actual ones for all strain rates.

In contrast to the predicted yield stresses under tension, the material model provided relatively low compressive true upper yield stresses for two strain rates including 0.2 s^{-1} and 0.4 s^{-1}. The reason, behind this, is obvious because we take the α=1.255 as constant for all strain rates; however, this is not quite true for ABS since α value for strain rate of 0.2 s^{-1} was already calculated as 1.315. Therefore, if α is less than its actual value for any strain rate, it will lead to an under estimation for compressive yield stresses. We also faced the same problem in the used material model (SAMP-1) used in numerical analysis that will be detailed later. However, the predicted compressive true upper yield stresses of ABS are in good agreements with the experimental findings.

As long as the feature of stress-strain curves stays generally identical regardless of strain rate and if there is no specific strain rate where the strain rate response of ABS becomes more sensitive since our approach gives linear relationship, the obtained strain rate parameter (C) for ABS will be well applicable to predict the yield stresses for high strain rates.

To make sure about our approach, we collected the yield stresses of ABS either under tension or compression for different strain rates from literature. Since different researchers provided dissimilar yield stresses of ABS for the analogue strain rates, we calculated the strain rate sensitivity parameter (C) for ABS based on provided data in literature.

Although Gean [118] did not provide any tabulated data for tensile yield stresses of ABS as a function of strain rate, the tensile upper-yield stresses were approximately taken from Fig 1.18. In the same fashion of the C calculation for our own ABS, the C value was calculated as 0.0635 from the tension test data provided by Gean.The lowest strain rate and corresponding tensile true upper yield stress were taken as 0.0006 s^{-1} and 30.5 MPa, respectively. Therefore, the yield stress expression as a function of strain rate was written as below:

$$\tilde{\sigma}_A = 30.5\left(1 + 0.0635\, ln\left(\frac{\dot{\varepsilon}^p}{0.0006}\right)\right) \tag{8.9}$$

The estimated results were favorably compared to experimental data and tabulated in Table 8.3 and graphically represented in Fig 8.6.

Table 8.3. Comparisons of tensile yield stresses of ABS with Gean's experimental data [118]

Strain Rate (1/s)	**Material Model Prediction**	**Experiment (Gean's Data)**
0.0006	30.5	30.5
0.0045	34.402	34
0.058	39.3534	37
0.22	41.935	41
2.3	46.48	45
33	51.639	49
104	53.862	55

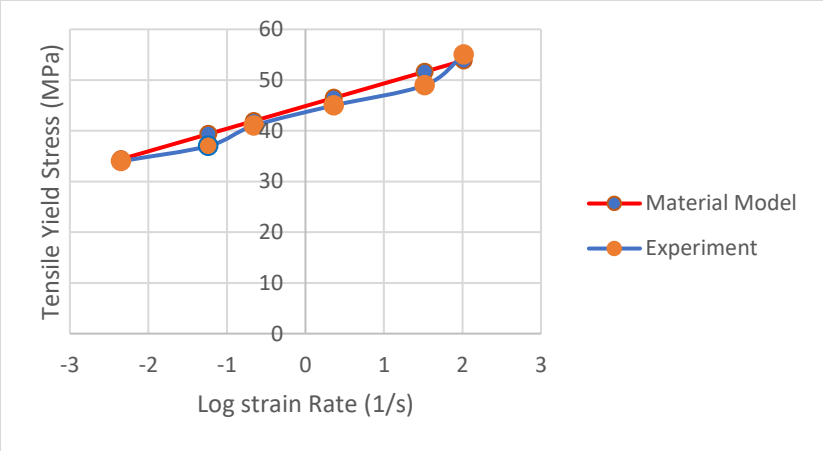

Fig 8.6. Material model prediction vs. Gean's experimental data

Gean provided the true stress-strain curves of ABS under tension for strain rates up to 104 s^{-1} and we successfully predicted the tensile true yield stress even for that high strain rate of 104 s^{-1} through our material model. The shape of tensile stress-strain curves of ABS reported by him do not change considerably with strain rates (see Fig 1.18).

Walley [119] provided the following compressive yield stress data for ABS as a function of strain rate.

Table 8.4. Compressive yield stress of ABS as a function of strain rate [119]

Polymer	0.006 (1/s)	0.68 (1/s)	17.1 (1/s)	1200 (1/s)	3340 (1/s)	11500 (1/s)
ABS	34.2±0.8	42.5±0.5	50±1	61±0.5	96±1.5	109±5

Since we do not have any tension test data, based on compressive data documented by him that is directly taken into calculations for the calculation of C parameter. Following the same procedure as previous, the strain rate sensitive parameter (C) was obtained as 0.0605. Again, the lowest strain rate of 0.006 s^{-1} and corresponding compressive yield stress of 34.2 MPa are taken as reference strain rate ($\dot{\varepsilon}_{O_A}$) and reference compressive yield stress(σ_C), respectively and substituted into eq (8.7) so we obtained the following expression.

$$\tilde{\sigma}_A = 34.2\left(1 + 0.0605\, ln\left(\frac{\dot{\varepsilon}^p}{0.006}\right)\right) \tag{8.10}$$

The comparison of calculated compressive yield stresses of ABS with his experimental data is tabulated in Table 8.5 and plotted in Fig 8.7.

Table 8.5. Comparisons of compressive yield stresses of ABS with Walley's experimental data[119]

Strain Rate (1/s)	Material Model Prediction	Experiment (Walley's Data)
0.68	43.7303	42.5
17.1	50.36359	50
1200	59.10789	61
3340	61.21345	96
11500	63.75676	109

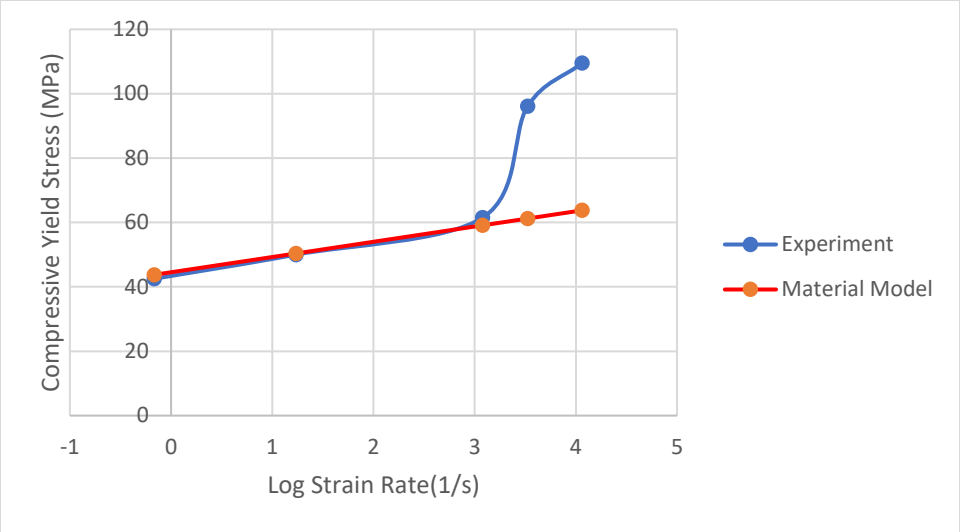

Fig 8.7. Material model prediction vs. Walley's experimental data

As seen in Table 8.5 and Fig 8.7, the obtained strain rate sensitivity parameter (C) for ABS successfully predicts the compressive yield stress of ABS for strain rates of 0.68 s^{-1}, 17.1 s^{-1} and 1200 s^{-1}; however, there is no good correlation found for very high strain rates of 3340 s^{-1} and 11400 s^{-1}. Walley claimed that compressive yield stresses of many polymers become more sensitive to strain rate with the strain rate of 1000 s^{-1}. It can be stated that the compressive yield stress of ABS can be well predicted up to strain rate of 1200 s^{-1} where its compressive yield stress starts to be more sensitive to strain rate.

As a summary;

- Using nominal tensile stress-strain curves at 5 distinct strain rates and Raghava's yield surface definition for tension case, initial value of strain rate sensitivity factor (C) for ABS was obtained as equal to 0.0361.
- The initial C value was used for iterative solutions to estimate true yield stresses of ABS as a function of strain rate and the optimum value for C was found as 0.0359.
- It is a fact that C value is generally small for polymers and not higher than 0.1 for most polymeric materials[4]

- We were successful to predict the yield stress of ABS as a function of strain rate for tension as well as, compression using the relationship $\alpha = \sigma_C / \sigma_T = 1.255$.
- Rather than our own ABS, we also defined the C values for ABS whose true stress-strain curves under tension and compression were provided by two different researchers in literature. The yield stresses of ABS under tension were successfully estimated including the high strain rate of 104 s^{-1}. Furthermore, the compressive yield stresses of ABS were estimated successfully up to high strain rate of 1200 s^{-1}. However, for strain rates larger than 1200 s^{-1} under compression, our C value failed to predict them well. Because , it was reported that mechanical response of many polymers become more sensitive to strain rate at a point where strain rate is about 1000s^{-1} and this strain rate can be given as 1200 s^{-1} for ABS based on Walley's experimental data[119]. Therefore, our approach to predict yield stresses of ABS under tension and compression is not applicable for strain rates that is higher than 1200 s^{-1}.
- Why we used Raghava's yield surface definition in our calculations is this his material model is capable of capturing the dissimilar material behaviors of polymers in tension and compression. Moreover, his yield surface definition is open to hydrostatic pressure. Assuming that $\alpha = \sigma_C = \sigma_T = 1$ and substituting it into eq (8.2), we derive $\tilde{\sigma}_A = \sqrt{3J_{2A}}$ that is the Von-Misses yield surface definition and this is not true for polymers.

Identification of Strain Softening/ Hardening Parameters

To capture the generally observed strain softening and following strain hardening behavior of amorphous thermoplastics ,Clausen [120] slightly modified the Boyce's material model adding one more term as shown in Fig 8.8.

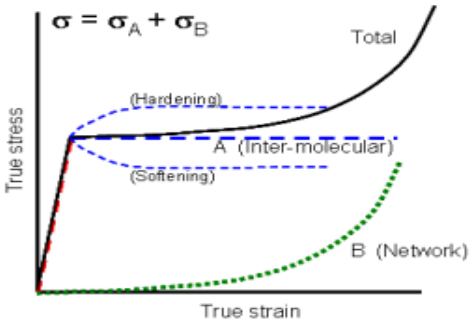

Fig 8.8. Constitutive model for strain softening and hardening

He assumed the yield surface definition as expressed below:

$$f_A = \tilde{\sigma}_A - \sigma_T - R\left(\varepsilon_A^p\right) \tag{8.11}$$

where $R\left(\varepsilon_A^p\right) = (\sigma_s - \sigma_T)\left(1 - exp\left(-H\varepsilon_A^p\right)\right)$ (8.12)

where σ_s and σ_T are saturated stress level and tensile yield stress, respectively and H is the exponential decay to capture strain softening or hardening feature in stress-strain curves of amorphous thermoplastics. If $(\sigma_s - \sigma_T) < 0$, it leads to strain softening and $(\sigma_s - \sigma_T) > 0$ provides strain hardening.

Different than his $R\left(\varepsilon_A^p\right)$ definition, we assumed the $R\left(\varepsilon_A^p\right)$ for ABS as indicated below:

$$R\left(\varepsilon_A^p\right) = (\sigma_s - \sigma_T)\frac{1-\left(exp\left(-H_1\varepsilon_A^p\right)\right)}{1+\left(exp\left(-H_2\varepsilon_A^p\right)\right)} \tag{8.13}$$

where H_1 and H_2 are exponential decay coefficients that help us to ideally fit the strain softening or hardening material behavior of ABS in its true stress-strain curves. The optimum values for σ_s, H_1 and H_2 will be obtained based on iteration process after defining the network resistance parameters (C_R and $\sqrt{N}$)

Identification of Network Resistance Parameters (C_r and $\sqrt{N}$)

Network resistance part defines the strain hardening based on hyperplastic material formulation and uses two coefficients such as C_r (initial elastic modulus of network resistance part)

and $\sqrt{N}$ (locking stretch). The mathematical expression for network resistance is depicted in eq (8.14) and definitions of other parameters in eq (8.12), see eq (1.13) in literature review part.

$$\sigma_B = \frac{1}{J_B}\frac{Cr}{3}\frac{\sqrt{N}}{\bar{\lambda}_N}\mathcal{L}^{-1}\left[\frac{\lambda_N}{\sqrt{N}}\right]\left[\tilde{B}^N - \left(\tilde{\lambda}_N\right)^2 I\right] \tag{8.14}$$

After many iterations, C_r and $\sqrt{N}$ values for ABS were found as 8.3 MPa and 1.13, respectively. Furthermore, σ_s, H_1 and H_2 parameters were calculated as 30.273 MPa, 200 and 60, respectively.

Initial elastic modulus of ABS can be calculated to be used in eq (1.12) as follows:

$$E_0 = E + C_r \tag{8.15}$$

and E_0=1834.3 MPa

Hence, all defined coefficients for ABS are documented in Table 8.6.

Table 8.6. Material parameters of ABS for constitutive model

E_0 (MPa)	**υ_0**	**σ_T**	**σ_s**	**H_1**	**H_2**	**α**	**$\dot{\varepsilon}_{o_A}$ (s^{-1})**	**C**	**C_r(MPa)**	**$\sqrt{N}$**
1834.3	0.38	38.273	30.273	200	60	1.255	0.0001	0.0359	8.3	1.15

Both intermolecular and network resistance contributions to total tensile true stresses of ABS are plotted against true strains as shown in Fig 8.9.

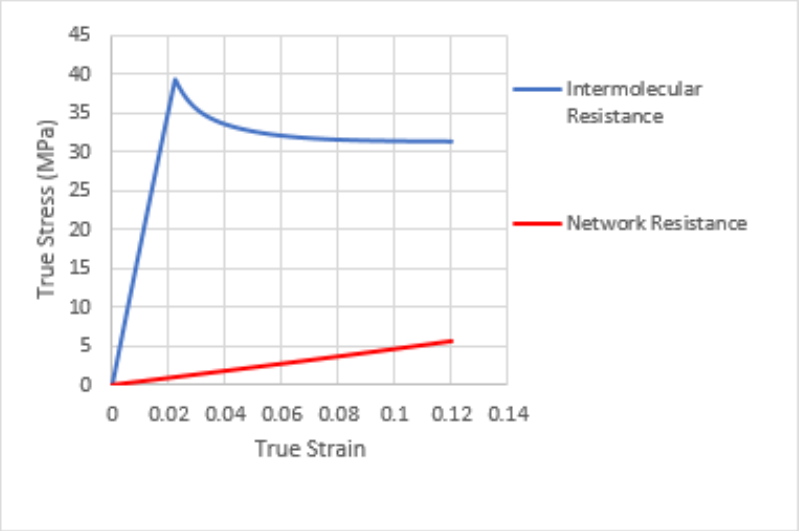

Fig 8.9. Intermolecular and network resistance contributions to material response of ABS under uniaxial tension at 0.0001 s^{-1}

When we sum these contributions, we obtain the strain rate response of ABS under uniaxial tension at 0.0001 s^{-1}. The comparison of material model prediction with experimental measurement is shown in Fig 8.10.

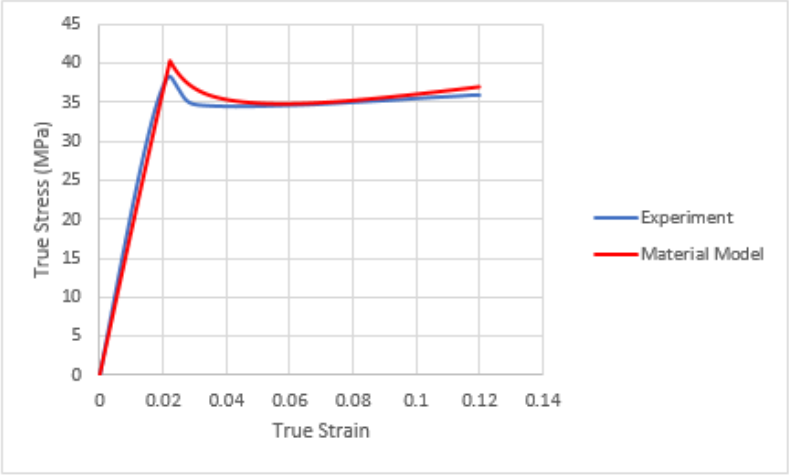

Fig 8.10. Material model vs. Experiment for ABS under uniaxial tension at 0.0001 (1/s)

Thus, the tensile strain rate response of ABS at 0.0001 s^{-1} was well predicted through using the all defined material parameters in constitutive model as seen in Fig 8.10. Strain softening and following strain hardening features in stress-strain curve of ABS was also successfully captured

by the material model. Our $R\left(\varepsilon_A^p\right)$ definition assisted us to capture those features. It is a fact that ABS experiences one more strain hardening stage before strain softening but that strain hardening part was neglected in our calculations. The material model provides slightly higher post-yield stress compared to experimental results because a summation of intermolecular (E) and network resistance (C_r) elastic modulus are taken into account as actual initial elastic modulus of ABS in the form of $E_0=E+C_r$ that leads to a slightly higher elastic modulus than the real elastic modulus of ABS and as a result of this, the material model gives post-yield stress slightly higher than the actual value.

This material model will increase the yield surface of ABS with keeping the shape of stress-strain curves of ABS same based on applied deformation or strain rates. With respect to dictated strain rate, the material model will calculate the post-yield stress of ABS depending on strain rate sensitivity parameter (C) and it will increase the post-yield stress up to the new post-yield stress level resulted by applied deformation rate.

In future, numerical implementations of ABS subjected to multiaxial loads, including 3-point bending and impact under different deformation rates and velocities that will be modelled through writing material subroutine for constitutive material model in finite element codes to find out accuracy of defined material parameters of ABS.

CHAPTER 9 DISCUSSIONS

The software based optical method of digital image correlation (DIC) was utilized to record strains for two lowest strain rates attained during uniaxial tension and shear tests. Depending on true longitudinal and transverse strains provided by DIC , tensile true stresses were calculated and they were compared to tensile true stress-true strain data calculated based on the extensometer data. After comparing the results, it was concluded that DIC and extensometer provide nearly similar results in terms of true strains and corressponding true stresses. Than, we relied upon the extensometer data for other strain rates under uniaxial tension. Nevertheless, the strain rate range for which we characterized the strain rate response of ABS is ranged from low to moderate and ABS does not include extremely large plastic deformation. Therefore, relying on extensometer data is somehow acceptable in this strain rate range but most probably ABS undergoes excessively large plastic strains at high deformation rates. Thus, the extensometer data will no longer be valid for high strain rate deformations because it will significantly overestimate the true stressess.

Although the used material model (Mat-SAMP-1) in the numerical simulations basically provided very good predictions compared to experimental results, this material model possesses some important limitations and drawbacks. Initially, a significant amount of mechanical test data including uniaxial tension,uniaxial compression and shear over a wide range of strain rates is required as an input to identify the real material behavior of ABS in this material model and it is not easy task to handle expreminal data in this model. Secondly, this material model considers the elastic modulus not dependent on strain rate but elastic material properties of ABS is affected by strain rate and it is increasing with strain rate.Thirdly, this material model assumes that compressive and tensile elastic modulus are identical to each other but the compressive elastic

modulus of ABS is always higher than the tensile one.Fourthly,this material model linearly increases the compressive and shear yield surface based on tension test data as a function of strain rate;however, ABS is more prone to strain rate under compression. Finally, when this material model increases the compressive and shear yield surface, it keeps the shape of curves same;nevertheless, the shear stress-strain curve changes with strain rate.

CHAPTER 10 CONCLUSIONS and RECOMMENDATIONS

10.1 Conclusions

The reseach findings from the combined experimental investigations and numerical validations, as weel as the non-destructive evaluation tools can be summarized as;

The fracture behavior of ABS was found as brittle; therefore, there was no distinguishable necking area observed in the ruptured ABS specimens under tension at any of the strain rates. It was noticed that the elastic region of ABS in its stress states under tension and compression was very small and it reached its limit immediately under all strain rates. Furthermore, the tensile and compressive elastic modulus of ABS were found to be strain rate dependent. Both compressive and tensile modulus of ABS increased with an increased strain rate and compressive modulus of ABS was always higher than its tensile modulus.

From the tensile true stress-strain curves of ABS, it was deduced that both intrinsic yield drop and neck stabilization took place immediately.Among the attained 8 different strain rates during tension tests, while the maximum intrinsic yield drop was measured as 5.446 MPa at the strain rate of 0.1 s^{-1}, the minumum one was concluded as 2.8 MPa for the strain rate of 30 s^{-1}. The avarage intrinsic yield drop can be given as 4.38 MPa.

The compressive strength of ABS was found always higher than its tensile strength under the same strain rates. The ratio of σ_C/σ_T was calculated as equal to 1.204 for the lowest strain rate, and the same ratio was obtained as 1.315 for the strain rate of 0.2 s^{-1} implying that ABS is more sensitive to strain rate under compression. After tension tests, it was noticed that along the entire gage length of ABS turned into light white color that was not observed after compression tests showing that micro voids formation occured in ABS under tension. Most probably, this is the primary reason for less tensile strength and tensile modulus compared to compressive strength and

elastic modulus since micro voids formation result a stiffness reduction in ABS under tension. The avarage ratio of of σ_C/σ_T was reported as 1.255 for ABS.

Generally, the shapes of tensile stress –strain curves of ABS do not considerably change with strain rates. The compressive stress-strain curves almost remained the same regardless of strain rate. Perhaps, stress-state under compression is more homogoneus than under tension that provides similar shapes.

There was no shear fracture observed in ABS during shear tests at different shear strain rates;although, the ABS shear specimens were forced to undergo large plastic strains about (0.35).

The strain rate sensitivity parameter (C) for ABS was calculated as equal to 0.0359 through using 5 distinct tensile nominal stress-strain curves of ABS under 5 lowest strain rates as well as, Raghava's yield formulation for polymers and upper yield stresses of ABS for the moderate strain rates of 10 s^{-1} , 30 s^{-1} and 45 s^{-1} were succesfully predicted by the derived strain rate sensitivite parameter. In general, strain rate sensitive parameter for polymers is not higher than 0.1.

The strain softening/hardening coefficients were obtained for ABS slightly modiyfying the existed constitutive material model to properly capture the strain softening and following strain hardening feature of ABS observed in its stress state under tension. The material model prediction for true stress-strain curve of ABS under tension at the lowest strain rate was compared to the experimental result and a very good correlation was established between them.

Since none of the reported information above in terms of material behavior of ABS under tension,compression and shear at various strain rates does not give any valid information regarding its actual material behavior under multiaxial loads,its actual material behavior was

measured by means of the conducted 3-point bending tests under different deformation rates. It was deduced that higher deformation rate resulted higher peak loads. This outcome is definetly logic because higher deformation rate generates a higher strain rate deformation and as reported, an increase in strain rate results an increase in tensile,compressive and shear strength of ABS.A color change (light white color) was observed only at the lower mid-span where subjected to tension. No damage indictaion was seen at the upper mid-span subjected to compression.

The impact peformance of ABS was investigated by means of conducting impact experiments at three different impact velocities. There was no penetration and extreme failure caused by any of the imposed impact velocities. The maximum impact energy that was attained in impact experiments was 78.48 J and the ABS enables to withstand the deformation caused by the maximum impact energy without showing any catashropic failure. Nevertheless, a cloudy and white color is physically noticed at the back surfaces of ABS after all impacts .Particularly, the region near impact point was dominated by white color for impact velocities of 5.775 m/s and 6.264 m/s. This color change is known as stress whitening in amorphous thermoplastics and that is the indication of localized material change caused by microvoids. Crazes or surface crack formation is primarily responsible for the onset of microvoids. Therefore, the impacted ABS specimens were evaluated by two powerfull non-destructive evaluation methods including ultrasonic C-Scan and laser scanning microscopy to detect damage areas and surface imperfactions, respectively. At the front surfaces of impacted ABS specimens, there is no localized damage reported as a two dimensional graphical respresentation by ultrasonic C-Scan for any impact energy level. Furthermore, no surface carck and microvoids on the front surfaces are detected by laser scanning microscopy rather than only plastic deformation. Nevertheless, extreme lozalized damage areas are detected at the back surfaces of ABS by ultrasonic C-Scan , especially

for impact velocities of 5.775 m/s and 6.264 m/s. After evaluating the back surfaces of impacted ABS specimens with laser scanning microscopy, it is found that there are only crazes at the back surface of ABS subjected to lowest impact energy of 39.24 J and no microvoids are discovered. Nevertheless, combinations of crazes and microvoids are seen at the back surfaces by laser scanning microscopy under impact velocities of 5.775 m/s J and 6.264 m/s explaining that crazes propagated their further dagame stage and microvoids are formed. Both findings coming from ultrasonic C-Scan and laser scanning microscopy are in a good agreement with each other.

An attempt to measure the strains near impact area was made by the use of three strain gages placed on the back surfaces of ABS during impacts. Radial strains near impact region were measured and strain rates were calculated for each impact velocity but an abnormal damage pattern was noticed near strain gages. Perhaps, a glue used in fixing the strain gages on the surfaces of ABS leads to an inconsistency in terms of stiffness. However, the measured strains and strain rates were compared to the numerically predicted results and acceptable agreements were obtained.

In terms of numerical implementations of uniaxial tension and compression tests, it was deduced that the utilized newly developed semi-empirical material model (SAMP-1) well predicted the stress-strain response of ABS in comparision to experimental results.

It is a fact that SAMP-1 material model can only be verified through the comparisions of numerically predicted load-displacement curves with experimentally measured curves under 3-point bending. Thus, the SAMP-1 was validated through the established very good agreements between the predicted and measured results in terms of load-displacement under 3-point bending.

In this study, our ultimate and actaul aim was to succesfully predict the impact behavior of ABS under various impact velocities using SAMP-1 material model in the explicit solver of LS-DYNA. Therefore, the necessary impact outcomes, including impact force, displacements and

kinetic energy variations with impact time was numerically obtained and compared to experimental results for each impact velocity. Thus, it was deduced that the impact behavior of ABS was predicted almost perfectly for impact velocities of 4.43 m/s and 5.775 m/s. There was also a very good correlation found between numerical and experimental results for impact velocity of 6.264 m/s. While the peak impact force was insignificantly over estimated for impact velocity of 6.264 m/s, the peak displacement was inconsiderably under estimated for the same impact velocity. It is hard to make a decision if the accuracy of SAMP-1 decreases with an increased impact velocity based on the currently measured impact test data. To make sure of the accuracy of SAMP-1 with impact velocity, several more impact tests need to be carried out on ABS under higher impact velocities.

With the consideration of effective plastic strains as a damage indication in the impact simulations, the estimated damaged areas were compared to the damage areas detected by ultrasonic C-Scan. There was a considerable discrepancy observed in the comparisons of predicted damaged areas with the detected damaged areas. SAMP-1 predicted the damaged areas much less than the detected ones for all impact velocities. As mentioned earlier, we considered effective plastic strains as damaged areas but in reality, the damage parameters for ABS should be measured from loading/unloading uniaxial tension tests and they need to be utilized as a material input in SAMP-1 for more accurate predictions.

Effective strains and strain rates near impact areas were numerically obtained from the numerical analyses of impact tests and compared to the registered results by strain gages. There was very good correlation found in terms of not only strains but also strain rates for all impact velocities.

10.2 Recommendations

The following future work recommendations may be put in order as:

The strain rate material response of ABS can be examined under high deformation rates to obtain more fundemental understanding of its strain rate dependent material behavior.

The temperature influnce on the material behavior of ABS can be investigated conducting the same mechanical tests over a wide range of temperature.

The temperature change generated by the interaction of chain macromolucules to one another during impact may be investigated to find out the temperature effect on the impact performance of ABS.

Damage parameters of ABS can be defined from loading-unloading uniaxial tension test and damage parameters may be included in numerical simulations.

REFERENCES

1. Van Krevelen, D.W. and K. Te Nijenhuis, *Properties of polymers: their correlation with chemical structure; their numerical estimation and prediction from additive group contributions*. 2009: Elsevier.
2. Mulliken, A.D., *Mechanics of amorphous polymers and polymer nanocomposites during high rate deformation*. 2006, Massachusetts Institute of Technology.
3. Amoedo, J. and D. Lee, *Modeling the uniaxial rate and temperature dependent behavior of amorphous and semicrystalline polymers.* Polymer Engineering & Science, 1992. **32**(16): p. 1055-1065.
4. Bauwens-Crowet, C., *The compression yield behaviour of polymethyl methacrylate over a wide range of temperatures and strain-rates.* Journal of Materials Science, 1973. **8**(7): p. 968-979.
5. Blumenthal, W. and C. Cady. *Influence of temperature and strain rate on the compressive behavior of PMMA and polycarbonate polymers*. in *APS Shock Compression of Condensed Matter Meeting Abstracts*. 2001.
6. Mulliken, A. and M. Boyce, *Mechanics of the rate-dependent elastic–plastic deformation of glassy polymers from low to high strain rates.* International journal of solids and structures, 2006. **43**(5): p. 1331-1356.
7. Ognedal, A.S., *Large-Deformation Behaviour of Thermoplastics at Various Stress States: An experimental and numerical study*. 2012.

8. Richeton, J., et al., *Influence of temperature and strain rate on the mechanical behavior of three amorphous polymers: characterization and modeling of the compressive yield stress.* International journal of solids and structures, 2006. **43**(7): p. 2318-2335.

9. Richeton, J., et al., *Modeling and validation of the large deformation inelastic response of amorphous polymers over a wide range of temperatures and strain rates.* International journal of solids and structures, 2007. **44**(24): p. 7938-7954.

10. Moy, P., et al. *Strain rate response of a polycarbonate under uniaxial compression*. in *Proceedings of the SEM conference on experimental mechanics*. 2003.

11. Xu, X. and X. Xu, *Mechanical properties and deformation behaviors of acrylonitrile-butadiene-styrene under Izod impact test and uniaxial tension at various strain rates.* Polymer Engineering & Science, 2011. **51**(5): p. 902-907.

12. Altenbach, H. and K. Tushtev, *A new static failure criterion for isotropic polymers.* Mechanics of Composite Materials, 2001. **37**(5): p. 475-482.

13. Galeski, A., *Strength and toughness of crystalline polymer systems.* Progress in Polymer Science, 2003. **28**(12): p. 1643-1699.

14. Imai, Y. and N. Brown, *The effect of strain rate on craze yielding, shear yielding, and brittle fracture of polymers at 77° K.* Journal of Polymer Science: Polymer Physics Edition, 1976. **14**(4): p. 723-739.

15. Davis, L. and C. Pampillo, *Deformation of polyethylene at high pressure.* Journal of Applied Physics, 1971. **42**(12): p. 4659-4666.

16. Lin, L. and A. Argon, *Structure and plastic deformation of polyethylene.* Journal of Materials Science, 1994. **29**(2): p. 294-323.

17. Rietsch, F. and B. Bouette, *The compression yield behaviour of polycarbonate over a wide range of strain rates and temperatures.* European Polymer Journal, 1990. **26**(10): p. 1071-1075.

18. Wu, W. and A. Turner, *Thermal activation parameters for large strain deformation of polyethylene and polycarbonate.* Journal of Polymer Science: Polymer Physics Edition, 1975. **13**(1): p. 19-34.

19. Schneider, K. and T. Seelig, *Numerical aspects of failure modeling of amorphous thermoplastics.* PAMM, 2014. **14**(1): p. 133-134.

20. Dean, G. and L. Wright, *An evaluation of the use of finite element analysis for predicting the deformation of plastics under impact loading.* Polymer testing, 2003. **22**(6): p. 625-631.

21. Rösler, J., H. Harders, and M. Baeker, *Mechanical behaviour of engineering materials: metals, ceramics, polymers, and composites*. 2007: Springer Science & Business Media.

22. G'sell, C., N. Aly-Helal, and J. Jonas, *Effect of stress triaxiality on neck propagation during the tensile stretching of solid polymers.* Journal of Materials Science, 1983. **18**(6): p. 1731-1742.

23. Vincent, P., *The necking and cold-drawing of rigid plastics.* Polymer, 1960. **1**: p. 7-19.

24. Meinel, G. and A. Peterlin, *Plastic deformation of polyethylene II. Change of mechanical properties during drawing.* Journal of Polymer Science Part A-2: Polymer Physics, 1971. **9**(1): p. 67-83.

25. Boyce, M.C., D.M. Parks, and A.S. Argon, *Large inelastic deformation of glassy polymers. Part I: rate dependent constitutive model.* Mechanics of Materials, 1988. **7**(1): p. 15-33.

26. Read, B. and G. Dean, *Modelling non-linear stress–strain behaviour of rubber toughened plastics.* Plastics, rubber and composites, 2001. **30**(7): p. 328-336.

27. Ward, I., *Mechanical Properties of Solid Polymers 2nd Edition John Wiley & Sons*. 1985, Ltd.

28. Rabinowitz, S., I. Ward, and J.S. Parry, *The effect of hydrostatic pressure on the shear yield behaviour of polymers.* Journal of materials Science, 1970. **5**(1): p. 29-39.

29. Spitzig, W. and O. Richmond, *Effect of hydrostatic pressure on the deformation behavior of polyethylene and polycarbonate in tension and in compression.* Polymer Engineering & Science, 1979. **19**(16): p. 1129-1139.

30. Chen, W., F. Lu, and M. Cheng, *Tension and compression tests of two polymers under quasi-static and dynamic loading.* Polymer testing, 2002. **21**(2): p. 113-121.

31. Stachurski, Z., *Deformation mechanisms and yield strength in amorphous polymers.* Progress in polymer science, 1997. **22**(3): p. 407-474.

32. Mears, D., K. Pae, and J. Sauer, *Effects of hydrostatic pressure on the mechanical behavior of polyethylene and polypropylene.* Journal of Applied Physics, 1969. **40**(11): p. 4229-4237.

33. Ward, I.M., *Review: The yield behaviour of polymers.* Journal of materials Science, 1971. **6**(11): p. 1397-1417.

34. Quinson, R., et al., *Yield criteria for amorphous glassy polymers.* Journal of Materials Science, 1997. **32**(5): p. 1371-1379.

35. Argon, A., *A theory for the low-temperature plastic deformation of glassy polymers.* Philosophical Magazine, 1973. **28**(4): p. 839-865.

36. Caddell, R.M. and J.W. Kim, *Influence of hydrostatic pressure on the yield strength of anisotropic polycarbonate.* International Journal of Mechanical Sciences, 1981. **23**(2): p. 99-104.

37. Chamis, C.C., *Analysis of three-point-bend test for materials with unequal tension and compression properties.* 1974.

38. Raghava, R., R.M. Caddell, and G.S. Yeh, *The macroscopic yield behaviour of polymers.* Journal of Materials Science, 1973. **8**(2): p. 225-232.

39. Caddell, R.M., R.S. Raghava, and A.G. Atkins, *Pressure dependent yield criteria for polymers.* Materials Science and Engineering, 1974. **13**(2): p. 113-120.

40. Whitney, W. and R. Andrews. *Yielding of glassy polymers: volume effects*. in *Journal of Polymer Science: Polymer Symposia*. 1967. Wiley Online Library.

41. Bouvard, J., et al., *A general inelastic internal state variable model for amorphous glassy polymers.* Acta mechanica, 2010. **213**(1-2): p. 71-96.

42. Kulich, D., et al., *Acrylonitrile–butadiene–styrene polymers*. 2002: Wiley Online Library.

43. Szeteiová, K., *Automotive materials plastics in automotive markets today.* Institute of Production Technologies, Machine Technologies and Materials, Faculty of Material Science and Technology in Trnava, Slovak University of Technology Bratislava, 2010.

44. Socrate, S., M. Boyce, and A. Lazzeri, *A micromechanical model for multiple crazing in high impact polystyrene.* Mechanics of Materials, 2001. **33**(3): p. 155-175.

45. Seelig, T. and E. Van der Giessen, *Localized plastic deformation in ternary polymer blends.* International journal of solids and structures, 2002. **39**(13): p. 3505-3522.

46. Ramsteiner, F., G. McKee, and M. Breulmann, *Influence of void formation on impact toughness in rubber modified styrenic-polymers.* Polymer, 2002. **43**(22): p. 5995-6003.

47. Donald, A.M. and E.J. Kramer, *Plastic deformation mechanisms in poly (acrylonitrile-butadiene styrene)[ABS].* Journal of Materials Science, 1982. **17**(6): p. 1765-1772.

48. Szeteiová, K., *Automotive materials plastics in automotive markets today.*

49. *<2016 Plastics and Polymer Composites in Light Vehicles Report.pdf>.*

50. Eyring, H., *Viscosity, plasticity, and diffusion as examples of absolute reaction rates.* The Journal of chemical physics, 1936. **4**(4): p. 283-291.

51. Spathis, G., *Theory for the plastic deformation of glassy polymers.* Journal of materials science, 1997. **32**(7): p. 1943-1950.

52. BAUWENSCROWET, C. and G. Homes, *La deformation plastique du polymethacrylate de methyle dans le domaine vitreux.* COMPTES RENDUS HEBDOMADAIRES DES SEANCES DE L ACADEMIE DES SCIENCES, 1964. **259**(20): p. 3434-&.

53. Roetling, J., *Yield stress behaviour of polymethylmethacrylate.* Polymer, 1965. **6**(6): p. 311-317.

54. Roetling, J., *Yield stress behaviour of poly (ethyl methacrylate) in the glass transition region.* Polymer, 1965. **6**(11): p. 615-619.

55. Bauwens, J., C. Bauwens-Crowet, and G. Homes, *Tensile yield-stress behavior of poly (vinyl chloride) and polycarbonate in the glass transition region.* Journal of Polymer Science Part A-2: Polymer Physics, 1969. **7**(10): p. 1745-1754.

56. Bauwens, J.C., *Relation between the compression yield stress and the mechanical loss peak of bisphenol-A-polycarbonate in the β transition range.* Journal of Materials Science, 1972. **7**(5): p. 577-584.

57. Bauwens-Crowet, C., J.-C. Bauwens, and G. Homes, *The temperature dependence of yield of polycarbonate in uniaxial compression and tensile tests.* Journal of Materials Science, 1972. **7**(2): p. 176-183.

58. Bauwens-Crowet, C., J. Bauwens, and G. Homes, *Tensile yield-stress behavior of glassy polymers.* Journal of Polymer Science Part A-2: Polymer Physics, 1969. **7**(4): p. 735-742.

59. Robertson, R.E., *Theory for the plasticity of glassy polymers.* The Journal of Chemical Physics, 1966. **44**(10): p. 3950-3956.

60. Haward, R. and G. Thackray. *The use of a mathematical model to describe isothermal stress-strain curves in glassy thermoplastics*. in *Proceedings of the Royal Society of London A: Mathematical, Physical and Engineering Sciences*. 1968. The Royal Society.

61. Duckett, R., S. Rabinowitz, and I. Ward, *The strain-rate, temperature and pressure dependence of yield of isotropic poly (methylmethacrylate) and poly (ethylene terephthalate).* Journal of Materials Science, 1970. **5**(10): p. 909-915.

62. Bowden, P. and S. Raha, *A molecular model for yield and flow in amorphous glassy polymers making use of a dislocation analogue.* Philosophical Magazine, 1974. **29**(1): p. 149-166.

63. Boyce, M.C., *Large inelastic deformation of glassy polymers*. 1986, Massachusetts Institute of Technology.

64. Arruda, E.M. and M.C. Boyce, *Evolution of plastic anisotropy in amorphous polymers during finite straining.* International Journal of Plasticity, 1993. **9**(6): p. 697-720.

65. Arruda, E.M., M.C. Boyce, and H. Quintus-Bosz, *Effects of initial anisotropy on the finite strain deformation behavior of glassy polymers.* International Journal of Plasticity, 1993. **9**(7): p. 783-811.

66. Arruda, E.M., M.C. Boyce, and R. Jayachandran, *Effects of strain rate, temperature and thermomechanical coupling on the finite strain deformation of glassy polymers.* Mechanics of Materials, 1995. **19**(2-3): p. 193-212.

67. Boyce, M., S. Socrate, and P. Llana, *Constitutive model for the finite deformation stress–strain behavior of poly (ethylene terephthalate) above the glass transition.* Polymer, 2000. **41**(6): p. 2183-2201.

68. Boyce, M.C., G. Weber, and D.M. Parks, *On the kinematics of finite strain plasticity.* Journal of the Mechanics and Physics of Solids, 1989. **37**(5): p. 647-665.

69. Polanco-Loria, M., et al., *Constitutive model for thermoplastics with structural applications.* International Journal of Impact Engineering, 2010. **37**(12): p. 1207-1219.

70. Ogden, R. and N.-L.E. Deformations, *Ellis Horwood Limited.* Chichester, UK, 1984.

71. Arruda, E.M. and M.C. Boyce, *A three-dimensional constitutive model for the large stretch behavior of rubber elastic materials.* Journal of the Mechanics and Physics of Solids, 1993. **41**(2): p. 389-412.

72. Anand, L. and M.E. Gurtin, *A theory of amorphous solids undergoing large deformations, with application to polymeric glasses.* International Journal of Solids and Structures, 2003. **40**(6): p. 1465-1487.

73. Richeton, J., et al. *Modeling of strain rates and temperature effects on the yield behavior of amorphous polymers*. in *Journal de Physique IV (Proceedings)*. 2003. EDP sciences.

74. *Standard Test Method for Tensile Properties of Plastics*. 2014, ASTM International.

75. G'sell, C., J. Hiver, and A. Dahoun, *Experimental characterization of deformation damage in solid polymers under tension, and its interrelation with necking.* International Journal of solids and structures, 2002. **39**(13): p. 3857-3872.

76. Louche, H., et al., *An experimental and modeling study of the thermomechanical behavior of an ABS polymer structural component during an impact test.* International Journal of Impact Engineering, 2009. **36**(6): p. 847-861.

77. Grytten, F., et al., *Use of digital image correlation to measure large-strain tensile properties of ductile thermoplastics.* Polymer Testing, 2009. **28**(6): p. 653-660.

78. Delhaye, V., et al., *Mechanical response and microstructure investigation of a mineral and rubber modified polypropylene.* Polymer Testing, 2010. **29**(7): p. 793-802.

79. Delhaye, V., et al., *Influence of stress state and strain rate on the behaviour of a rubber-particle reinforced polypropylene.* International Journal of Impact Engineering, 2011. **38**(4): p. 208-218.

80. Moura, R.T., et al., *Impact on HDPE and PVC plates–experimental tests and numerical simulations.* International Journal of Impact Engineering, 2010. **37**(6): p. 580-598.

81. Parsons, E., M.C. Boyce, and D.M. Parks, *An experimental investigation of the large-strain tensile behavior of neat and rubber-toughened polycarbonate.* Polymer, 2004. **45**(8): p. 2665-2684.

82. *Standard Test Method for Compressive Properties of Rigid Plastics*. 2015, ASTM International.

83. Xiang, C. and H.J. Sue, *Iosipescu shear deformation and fracture in model thermoplastic polyolefins.* Journal of applied polymer science, 2001. **82**(13): p. 3201-3214.

84. Liu, K. and M. Piggott, *Fracture failure processes in polymers. I: Mechanical tests and results.* Polymer Engineering & Science, 1998. **38**(1): p. 60-68.

85. Liu, K. and M. Piggott, *Fracture failure processes in polymers. II: Fractographic evidence.* Polymer Engineering & Science, 1998. **38**(1): p. 69-78.

86. Daiyan, H., et al., *Shear testing of polypropylene materials analysed by digital image correlation and numerical simulations.* Experimental mechanics, 2012. **52**(9): p. 1355-1369.

87. *Standard Test Method for Shear Properties of Composite Materials by the V-Notched Beam Method*. 2012, ASTM International.

88. *Standard Test Methods for Flexural Properties of Unreinforced and Reinforced Plastics and Electrical Insulating Materials*. 2015, ASTM International.

89. Du Bois, P., et al., *Material behaviour of polymers under impact loading.* International Journal of Impact Engineering, 2006. **32**(5): p. 725-740.

90. Duan, Y., et al., *Impact behavior and modeling of engineering polymers.* Polymer Engineering & Science, 2003. **43**(1): p. 112-124.

91. Dean, G. and L. Crocker, *Prediction of impact performance of plastics mouldings Part 1: Materials models and determination of properties.* Plastics, rubber and composites, 2007. **36**(1): p. 1-13.

92. Frank, T., et al. *Development and validation of numerical pedestrian impactor models*. in *4th European LS-DYNA Users Conference*. 2003.

93. Du Bois, P., et al. *Crashworthiness analysis of structures made from polymers*. in *3rd LS-DYNA Forum*. 2004.

94. Viana, J.C., A.M. Cunha, and N. Billon, *Experimental characterization and computational simulations of the impact behavior of injection-molded polymers.* Polymer Engineering & Science, 2007. **47**(4): p. 337-346.

95. Daiyan, H., *Experimental and Numerical Investigation of the Mechanical Response of Injection Moulded Polypropylene Materials.* PhD Dissertation, 2011.

96. Kolling, S., et al., *SAMP-1: a semi-analytical model for the simulation of polymers.* LS-DYNA Anwenderforum, 2005.

97. Haufe, A., *Validation and Material Modelling of Plastics.* LS-DYNA European Users Conference, Strasbourg, 2011.

98. LS-DYNA, *KEYWORD USER'S MANUAL VOLUME II.* May 19, 2014 (revision: 5442).

99. *<Aerospace_MGD_v12-1 (1).pdf>.*

100. Daiyan, H., et al., *Numerical simulation of low-velocity impact loading of a ductile polymer material.* Materials & Design, 2012. **42**: p. 450-458

101. Walley, S. and J. Field, *Strain rate sensitivity of polymers in compression from low to high rates.* DYMAT j, 1994. **1**(3): p. 211-227.

102. Duan, Y., et al., *Impact behavior and modeling of engineering polymers.* Polymer Engineering & Science, 2003. **43**(1): p. 112-124.

103. Owolabi, G., et al., *Dynamic response of acrylonitrile butadiene styrene under impact loading.* International Journal of Mechanical and Materials Engineering, 2016. **11**(1): p. 3.

104. Dean, G. and L. Wright, *An evaluation of the use of finite element analysis for predicting the deformation of plastics under impact loading.* Polymer testing, 2003. **22**(6): p. 625-631.

105. Yin, Z. and T. Wang, *Deformation response and constitutive modeling of PC, ABS and PC/ABS alloys under impact tensile loading.* Materials Science and Engineering: A, 2010. **527**(6): p. 1461-1468.

106. Schmailzl Anton, A.T., Glockner Markus, Fadanelli Martin, , *Finite element analysis of thermoplastic probes under tensile load using LS-DYNA compared to ANSYS WB 14 in correlation to experimental investigations* ANSYS Conference & 30th CADFEM Users' Meeting 2012 October 24-26 , 2012 – Kongress Palais Kassel

107. Louche, H., et al., *An experimental and modeling study of the thermomechanical behavior of an ABS polymer structural component during an impact test.* International Journal of Impact Engineering, 2009. **36**(6): p. 847-861.

108. Viana, J.C., A.M. Cunha, and N. Billon, *Experimental characterization and computational simulations of the impact behavior of injection-molded polymers.* Polymer Engineering & Science, 2007. **47**(4): p. 337-346.

109. Lobo, H. and B. Croop, *A robust methodology to calibrate crash material models for polymers.*

110. Frank, H., S. Hiermaier, and M. Neuman, *Material models for polymers under crash loads existing LS-DYNA models and perspective.* Ls-Dyna Anwenderforum, Bamberg, 2005.

111. Kolling, S., et al., *SAMP-1: a semi-analytical model for the simulation of polymers.* LS-DYNA Anwenderforum, 2005.

112. Daiyan, H., et al., *Numerical simulation of low-velocity impact loading of a ductile polymer material.* Materials & Design, 2012. **42**: p. 450-458.

113. Polanco-Loria, M., et al., *Constitutive model for thermoplastics with structural applications.* International Journal of Impact Engineering, 2010. **37**(12): p. 1207-1219.

114. Boyce, M., S. Socrate, and P. Llana, *Constitutive model for the finite deformation stress–strain behavior of poly (ethylene terephthalate) above the glass transition.* Polymer, 2000. **41**(6): p. 2183-2201.

115. Argon, A., *A theory for the low-temperature plastic deformation of glassy polymers.* Philosophical Magazine, 1973. **28**(4): p. 839-865.

116. Raghava, R., R.M. Caddell, and G.S. Yeh, *The macroscopic yield behaviour of polymers.* Journal of Materials Science, 1973. **8**(2): p. 225-232.

117. Polanco-Loria, M., et al., *Constitutive model for thermoplastics with structural applications.* International Journal of Impact Engineering, 2010. **37**(12): p. 1207-1219.

118. Dean, G. and L. Wright, *An evaluation of the use of finite element analysis for predicting the deformation of plastics under impact loading.* Polymer testing, 2003. **22**(6): p. 625-631.

119. Walley, S. and J. Field, *Strain rate sensitivity of polymers in compression from low to high rates.* DYMAT j, 1994. **1**(3): p. 211-227.

120. Clausen, A.H., et al. *A constitutive model for thermoplastics with some applications*. in *In 8th European LS-DYNA users conference*. 2011.

ABSTRACT

STRAIN RATE DEPENDENCE AND IMPACT BEHAVIOR OF ABS (ACRYLONITRILE-BUTADIENE-STYRENE) AMORPHOUS THERMOPLASTIC

by

MEHMET AKIF DUNDAR

December 2017

Advisor: Dr. Emmanuel. O Ayorinde

Major: Mechanical Engineering

Degree: Doctor of Philosophy

ABS (acrylonitrile-butadiene-styrene) is an extensively utilized amorphous thermoplastic in numerous engineering applications, such as marine, aerospace, automotive, electronic enclosures and housings because it offers many distinctive material properties, including good impact resistance, high toughness, high stiffness and high compressive strength. The most considerable material quality of ABS is its excellent impact resistance compared to other amorphous thermoplastics and this distinguished material ability makes the ABS very appealing for such unique engineering applications where a good impact resistance is highly needed. Nevertheless, the material behavior of ABS under impact loads is highly complex due to chaotically arranged chain macromolecules and randomly dispersed rubber particles in its structure. Therefore, understanding its impact behavior is currently under a considerable investigation. Particularly, a numerical analysis to accurately predict the impact behavior of ABS has been of very desired industrial interest.

Thus, the primary aim of this study was to successfully predict the impact response of ABS subjected to various impact velocities utilizing the semi-empirical material model (SAMP-1) in the explicit solver of LS-DYNA. The material parameters of ABS used as an input in SAMP-1

were obtained through the conducted uniaxial tension tests over a wide range of strain rates varying from low to high, as well as, uniaxial compression and shear tests at different strain rates. Numerical predictions were favorably compared to experimental results and there was a very good agreement found between them. Hence, the impact response of ABS under different impact velocities was numerically predicted with a very high accuracy.

Additionally, after the ABS material was subjected to impacts, two powerful non-destructive evaluation methods, such as ultrasonic C-Scan and laser scanning microscopy, were utilized to detect damaged areas and surface imperfections, respectively. The detected damaged areas by ultrasonic C-Scan were also compared to the numerically predicted damaged areas.

AUTOBIOGRAPHICAL STATEMENT

MEHMET AKIF DUNDAR

Mehmet Akif DUNDAR earned his Bachelor's degree in Mechanical Engineering from the Kirikkale University of Turkey in 2005. Shortly after earning his Bachelor's degree, he started working as a project engineer in one big natural gas distributor company of Turkey. He resigned from his job in January 2009 because he was awarded a scholarship by the Turkish Ministry of Education and the scholarships which covered his English classes, Master of Science and PhD studies. He attended the Ohio University to learn English in April 2009 and spent about 14 months at the Ohio University. After that, he joined the Wayne State University to start his Master of Science in August 2010. During his master studies, he generally focused on a combined experimental work and numerical implementation of free vibration analysis of rectangular plates. He earned his Master of Science degree in August 2012. Following his master's, he immediately started his PhD at the Wayne State University. For his PhD studies, he specifically studied on strain rate dependence and impact behavior of amorphous polymers. He is currently a PhD candidate at the Wayne State University and expects to graduate in August 2017.